Nanoparticle Magnetic Characterization and Comparison of Rock Anisotropy Methods

By

Brendan Snow

A thesis submitted in partial fulfillment of the requirements for the degree of

Master of Science

in

Geophysics

Department of Physics

University of Alberta

ABSTRACT

The mass susceptibility and associated Curie temperatures were determined for a series of ternary manganese and zinc ferrite nanoparticles (Mn–Zn ferrite NPs) with ratios of Mn:Zn ranging from 0.67-2.33. Variations in the Mn:Zn ratio of these Mn–Zn ferrite nanoparticles largely unaffected the particle size with the average grain diameter for the samples studied being 7nm. At room temperature (20°C) and low applied field strength the mass susceptibility remains relatively consistent as the Mn:Zn ratio increases from 0.67 to 2.33 with the further increase in the amount of manganese resulting in a slight decrease of the mass susceptibility. A similar trend is also observed in the saturation magnetization for each particle, where the saturation magnetization decreases slightly with increased Mn content. At elevated temperatures (125°C) both the saturation magnetization and magnetic susceptibility increase with the relative Mn content, both at a relatively similar ratio of 5x stronger magnetization saturation and susceptibility for a ratio of 2.33 than 0.67. Mn rich compositions have a significantly lower temperature dependence which makes them more suitable for downhole conditions of over 100°C with a response greater than 6.5 times that of nanomagnetite (nMag).

The correlations between anisotropy of magnetic susceptibility (AMS), anisotropy of isothermal remanent magnetization (AIRM), gyroremanent magnetization (GRM) and acoustic anisotropy were investigated for a set of metasediments and metavolcanics and plutonic rocks from a ductile shear zone in the Flin Flon Belt of the Trans-Hudson Orogen. Ultrasonic laboratory measurements of shear wave velocities were carried out at various polarizations under

atmospheric pressure conditions to characterize shear wave anisotropy and verify alignment to visible textural elements within the rock sample. The fastest shear wave velocities observed systematically had a polarization within the bedding plane and parallel to any visible lineation while the slowest shear wave propagation direction was found to be perpendicular to the bedding plane. These results were then compared to various magnetic fabric measurement techniques where the anisotropy of magnetic susceptibility was compared to the anisotropy of isothermal remanent magnetization and gyroremanent magnetization. Comparisons between these different magnetic methods determined that there was a clear foliation visible in the magnetic fabric with the bulk of the fabric being sourced from the diamagnetic to paramagnetic components which aligned with the lattice preferred orientation (LPO) observed via acoustic anisotropy. Some samples included a ferrimagnetic component largely due to multidomain ferrimagnetic grains. One sample was observed to contain stable single domain grains due to the retention of a GRM. This sample was shown to have a clear foliation in the XY plane which agreed with the visible fabric. This sample was originally thought to be quasi isotropic based on p-wave measurements however this is not the case due to the magnetic and s-wave anisotropies supporting a magnetic and acoustic rock fabric. The observed AMS and AIRM principle axes displayed a high degree of correlation with the elastic coefficients previously measured for each sample by Cholach et al. (2005). The orientation of s-wave splitting was also well aligned with the declination of the AMS principle axes with the maximum magnetic susceptibility axis having a similar declination to the azimuth of the fast polarity. The minimum principle magnetic susceptibility axis was aligned with the azimuth of the slow s-wave polarity.

PREFACE

Some of the research conducted for this thesis forms part of a collaboration between Professor David K. Potter at the University of Alberta and Professor Andrew R. Barron from Rice University. The group at Rice University were responsible for the synthesis of the magnetic nanoparticles used in **Chapter 2**. I was responsible for the collection of magnetic Curie point data at the University of Alberta with a Bartington furnace and the magnetization curves were measured by Arfan Ali in the UK with a variable field translation balance. The results of Chapter 2 were published in a peer-reviewed journal as follows:

Lauren Morrow, Brendan Snow, Arfan Ali, Samuel J. Maguire-Boyle, Zeyad Almutairi, David K. Potter & Andrew R. Barron (2018) Temperature dependence on the mass susceptibility and mass magnetization of superparamagnetic Mn-Zn-ferrite nanoparticles as contrast agents for magnetic imaging of oil and gas reservoirs, Journal of Experimental Nanoscience, 13:1, 107-118, DOI: 10.1080/17458080.2018.1426894

To link this aricle: https://doi.org/10.1080/17458080.2018.1426894

This thesis also utilizes some of the samples studied by Cholach et al. (2005) and uses some of this published data in a comparative anisotropy analysis in **Chapter 3** and **Chapter 4**. The data measured by Cholach et al. (2005) on the samples studied in this thesis consisted of uniaxial p-wave velocity measurements at elevated confining pressures as well as sample density values which were both used to compute elastic coefficients. My work in this thesis expands upon the previous measurements by introducing s-wave velocity measurements at various polarities measured under atmospheric pressure as well as various magnetic anisotropy measurements (AMS, AIRM, and GRM) on a subset of rock samples studied by Cholach et al. (2005) to be compared with the previously measured rock properties.

ACKNOWLEDGEMENTS

I would like to thank my supervisor, Dr. David K. Potter for his guidance, advice and support throughout my research at the University of Alberta. His patience and support have been invaluable over the past few years at the University of Alberta. I would also like to thank Dr. Douglas R. Schmitt for his support and advice throughout my entire career at the University of Alberta. Dr. Petar Petrov was also very helpful as a source of advice and support which I greatly appreciated. I also wish to thank my committee members for their revisions and suggestions to improve the quality of my thesis.

TABLE OF CONTENTS

LIST OF TABLES

LIST OF FIGURES

LIST OF SYMBOLS

X – Magnetic susceptibility

χ_m – Mass magnetic susceptibility

μ_o – Permeability of free space

H – Magnetic field

H_c – Coercive force

M – Induced Magnetization

M_{sat} – Saturation magnetization

τ – Relaxation time

T_c – Curie temperature

SP – Superparamagnetic

SD – Single domain

SSD – Stable single domain

MD – Multidomain

np's – Nanoparticles

nMag – Nano magnetite

Mn – Manganese

Zn – Zinc

s-wave – Shear wave

p-wave – Compressional wave

C_{11}, C_{22}, and C_{33} – Main diagonal elastic coefficients related to bulk modulus

AMS – Anisotropy of magnetic susceptibility

AMR – Anisotropy of magnetic remanence

AIRM – Anisotropy of isothermal remanent magnetization

GRM – Gyroremanent magnetization

Azimuth – Rotation of s-wave polarization clockwise from 0 degrees

Inclination – plunge of principle axes below the plane

Declination – trend of principle axes clockwise from 0 degree

CHAPTER 1: INTRODUCTION

The exploration of the Earth's crust has been the subject of many scientific studies since James Hutton presented the Theory of the Earth in 1785. Over the last century, in particular, this field has seen many advancements in the methods used for exploration; these methods include but are not limited to seismic, magnetic, electrical and gravitational surveys. Of these, magnetic and seismic exploration have seen extensive use in petroleum exploration where both of these methods are used to remotely sense the elastic and magnetic properties of rocks beneath the earth's surface to determine the geologic history and potential resource. However, the magnetic and elastic properties of most geomaterials are anisotropic, which is to say that the observed properties will vary depending on the direction of observation. This variation or anisotropy is the result of many combined factors ranging from the small scale such as composition, crystal structure, individual grain orientation up to larger processes including deposition and structural deformation processes. Part of this thesis will compare magnetic and acoustic anisotropy on a suite of rock samples.

Every material is inherently magnetic to some degree, and for geomaterials, these magnetic properties are controlled by the rock fabric that is the result of the composition, crystal structure, size and shape of each grain within the sample. At this base level, other petrophysical parameters such as the electrical resistance, resistivity and acoustic wave velocity are also controlled by these inherent rock fabric characteristics albeit by different means. These physical properties of the materials also tend to vary with the direction of observation (at least by a small degree); this variance with direction is referred to as the material's anisotropy. The anisotropy of materials was traditionally viewed as unnecessary information in resource exploration, however over time we have begun to explore increasingly complicated systems, and now it is advantageous to account for this anisotropy. Some potential geologic sources of anisotropy for different types of rocks are listed by Helbig (1994):

Igneous: Preferential orientation of mineral grains due to magma flow.

Sedimentary: Settling of grains with the flat axis parallel to the horizontal bedding plane and the long axis in the direction of fluid flow.

Sedimentary: Vertical compaction during diagenesis further rotates long axis into horizontal bedding plane.

Metamorphic: Strain resulting in preferentially oriented cracks and joints.

Metamorphic: Recrystallization causing a lineation or foliation.

Metamorphic: Nonhydrostatic stress resulting in the preferential opening of cracks and pores.

Due to these various sources of rock fabrics a strong understanding of anisotropic behavior for a given material can tell us valuable information about (i) the geologic processes that have occurred to create and deform the material, and through this (ii) how best to map and exploit natural resources in the system. To do this, we must first answer some basic questions, such as "what is the cause of the anisotropy and how can we relate this back to the mineral orientations within the rock itself?"

In this thesis, the links between the observed magnetic and acoustic anisotropies will be explored for various rock samples to describe the sample's petrophysical rock fabric. Additionally, the effects of grain size will also be discussed regarding the effect on the observed magnetic response. This will be accomplished by measuring the magnetic anisotropy of various rock samples (that are metamorphic in origin). This will then lead to a comparative study between the observed magnetic fabric and the laboratory measured P and *S-wave* anisotropy and the previously determined elastic coefficients (Cholach et al., 2005). This comparison hopes to identify relationships that will allow us to more expeditiously quantify the anisotropy within our samples by using one method to predict the response of another. There are a few works that compare some of these anisotropic methods such as AMS and acoustic (Owens and Bamford, 1976; Potter, 2004; Han, 2005; Robion et al., 2014) but to our knowledge there have been few studies to directly compare the responses between the different magnetic anisotropy methods of AMS, AIRM, and GRM with elastic wave anisotropy on the same sample set.

To fill the gap of comparative studies, this thesis investigates the relationship between anisotropy of magnetic susceptibility (AMS), anisotropy of magnetic remanence (AMR) specifically gyroremanent magnetization (GRM) and isothermal remanent magnetization (IRM), and acoustic anisotropy. Towards this end, metamorphic samples taken from the Flin Flon Belt of the Trans Hudson Orogen were investigated. These rocks were selected due to their strong visible rock fabric, which allows for an easy reference to compare magnetic anisotropy measurements. The magnetic measurements will then be compared to previous and new ultrasonic measurements that have been performed specifically with interest to how they relate to the observed rock fabric in the sample. Ideally, this will allow for the use of AMS and AMR measurements to quickly estimate the degree and orientation of acoustic anisotropy within a sample. This is desirable since measuring the acoustic anisotropy of a sample is a time-consuming process which requires significantly more sample material and preparation to completely characterize than the magnetic methods. Acoustic measurements are especially time-consuming when measuring the elastic anisotropy as a function of confining pressure as different pressure runs can take a day to complete and could potentially damage the sample. By using magnetic data first, it could be possible to optimize the experimental setup for the

various acoustic measurements. There is also the added benefit that the magnetic results are largely independent of porosity.

In addition to this, the use of magnetic properties as a tool in reservoir characterization will also be explored. The use of Manganese - Zinc ferrite nanoparticles as a magnetic contrast agent will be investigated as proposed in Morrow et al. (2014). The ultimate goal of this research is to establish the viability of Mn-Zn ferrites as magnetic contrast agents to track the propagation of hydraulic fracture proppant. This will ultimately be used to assess the effectiveness of a frac job and provide some downhole measurement of fracture propagation. For this thesis, we will expand on the characterization of several different magnetic nanoparticles, each with varying Zn:Mn ratios. It is proposed that the relative Zn content will impact the magnetic susceptibility, saturation magnetization and Curie points of these different nanoparticles. Please note that we have published the results of this particular study in Morrow et al. (2018).

1.1 BACKGROUND

Magnetic anisotropy methods are highly accurate and sensitive to changes in the magnetic rock components; they have the advantage over most other anisotropic methods of being able to provide rapid 3-D data based on a small amount of sample material. The following sections will serve to describe the underlying principles of the different anisotropic methods and to explain what information can be gained from each.

The anisotropy of magnetic susceptibility (AMS) is a fast method that can be used to help describe the magnetic fabric of a material, which is often linked to the overall fabric of the material itself. The use of low field magnetic susceptibility anisotropy has been successful in the study of various rock fabrics. There are some drawbacks to the exclusive use of AMS because relatively small amounts of single-domain ferrimagnetic material can introduce a strong ambiguity in the AMS fabric. To avoid ambiguity, the anisotropy of magnetic remanence (AMR) has been used to characterize any ferrimagnetic contribution towards the magnetic susceptibility and can additionally be used to resolve multiple magnetic fabrics. Similarly, anisotropy seen in elastic waves is dependent on many factors: alignment of constituent mineral grains, any preferred crystallographic orientation within said grains, preferential alignment of pores (including microfractures) and pore structure within the sample. Many of these factors can be influenced by the history of a rock, including the depositional environment and subsequent deformation. It is reasonable to expect a correlation between the acoustic and magnetic results, which would allow us to use one type of anisotropy to predict another anisotropic property. This thesis will work to investigate any such correlation within several different sample types. This would allow for rapid sample characterization and a quick first impression of the rock fabric. Magnetic fabric information could also allow for a more efficient experimental design when measuring the other characteristics; for example, the magnetic fabric could be used to identify the best axes to measure the greatest degree of shear wave splitting or the minimum and maximum axes of compressional wave anisotropy. To test this

interaction, the magnetic fabric of rocks altered by metamorphic processes were measured and compared to their previously determined elastic coefficients (Cholach et al., 2005). The degree of shear wave anisotropy was also be more closely investigated by measuring the orientation and degree of shear wave anisotropy. This was also compared to the magnetic fabric.

The approach taken to define the anisotropic rock properties will include the use of four complementary methods applied to the same samples. Each of the methods introduced here will be explained in greater detail later on.

1) IRM – Will provide the strongest signal of the magnetic remanence methods and indicate the presence of ferrimagnetic components within a sample.
2) GRM – Very sensitive to the anisotropy of Stable Single Domain particles. This will help to put a constraint on the size of any ferrimagnetic material seen within each sample as well as to identify any preferential orientation of these grains.
3) AMS – Fast method to help determine size shape and orientation of magnetic particles and the bulk magnetic fabric of a sample. This method will contain contributions from all the components of the sample rather than just the remanence carrying particles.
4) Elastic Wave Velocities - measurements previously taken for the samples investigated, as well as new measurements, to identify preferred crystallographic as well as grain orientation within a sample related to the rock fabric.

In addition to the anisotropy characterization, petrophysical magnetic measurements can also be used to help quantify different reservoir properties. The use of Mn-Zn ferrite nanoparticles as magnetic contrast agents will be investigated. The magnetic susceptibility of these Mn-Zn particles was measured to determine their suitability as magnetic tracer agents. One application for these would be to assess the effectiveness of a hydraulic fracturing operation by using them as tracers to measure the distribution of the proppant used. However, their usefulness will be dependent on the contrast of their magnetic properties (magnetic susceptibility, saturation magnetization, and Curie point) and the reservoir rock both at room temperature and more importantly under reservoir temperature conditions. These properties were measured for a variety of particle compositions where the Mn:Zn ratio was varied between samples. From this, we expected to see that a higher relative Zn content would result in a lower Curie point, which would in turn result in reduced effectiveness under reservoir conditions as the lower susceptibility and saturation magnetization at a higher temperature will have a smaller contrast with the surrounding rock formation.

The characterization of the Manganese-Zinc ferrite nanoparticles allowed us to understand some of their basic magnetic properties. The goal of this work was to determine how these nanoparticles would react under reservoir temperature conditions and to identify factors that influence their detection such as their magnetic susceptibility values. These particles and their characteristics are detailed in **Chapter 2**. Although beyond the scope of this work the ultimate goal is to develop a method of detecting in situ permeability anisotropy.

1.2 MAGNETIC PARAMETERS & ANISOTROPY

To give some context, it is useful to review some basic principles of magnetism and the magnetic properties of minerals. This is a broad field of study, the basics of magnetism are well outlined in Griffiths (1999) whereas a more specific look at magnetic fields within rocks can be found in Tarling and Hrouda (1993), Lowrie (2007), and Spaldin (2010). At the most basic level, any moving charge will generate a magnetic field; this can be easily visualized by electrons moving through a wire. This movement will create a magnetic field which curls around the wire in the plane perpendicular to the current flow. If we scale this principle down to the atomic level, it can be shown that one electron will create a current as it orbits around the nucleus and spins about its axis, which will result in a magnetic moment. All materials must exhibit some magnetic properties if they are above absolute zero, and when exposed to a magnetic field they will display a net magnetization, which is the result of the superposition of all the individual magnetic moments within the material. There are detailed derivations which describe different magnetic responses to an applied field shown in multiple works (Griffiths, 1999; Lowrie, 2007; Spaldin, 2010). However, the main classes of magnetic materials are summarised here:

1) **Paramagnetism**. Paramagnetism occurs in materials that can maintain net magnetic moments for the individual atoms; these magnetic moments are randomly oriented due to thermal agitation resulting in a net zero magnetization in the absence of an external magnetic field. However, these materials will begin to align their magnetic moments with an applied magnetic field (see ***Figure 1***)**.** This results in a net magnetization along the direction of the applied field. This effect is due to the outermost electron levels being unfilled which results in unpaired electrons. These unpaired electrons will orient their spins such that the magnetic moments produced will align with the applied magnetic field. Paramagnetic materials are characterized by a weak positive magnetic susceptibility, which is because the moments only partially align with the applied magnetic field.
2) **Diamagnetism.** Diamagnetism is the result of the change in the electron orbital motions when exposed to a magnetic field. This effect acts in opposition to the applied magnetic field which results in a magnetic moment aligned antiparallel to the applied field (***Figure 1***)**.** All matter will display this response, however it is important to note that the diamagnetic effect is weaker than the paramagnetic effect so the net moment in paramagnetic materials will still align parallel to the field. Diamagnetism can only be seen in atoms that have no net magnetic moment. This requires the outermost electron shells to be filled so as not to be eclipsed by paramagnetic or ferromagnetic effects. This results in diamagnetic materials being characterized by a very weak negative magnetic susceptibility. Similarly to paramagnetic materials, diamagnetic materials are unable to maintain a magnetization in the absence of a magnetic field due to thermal agitations Diamagnetic minerals will only impact the magnetic anisotropy that is observed if there are virtually no other magnetic components within the rock. For example when the ferromagnetic component is less than 0.0001% of the rock mass, and the paramagnetic

fraction is less than 1% (Tarling and Hrouda, 1993). Under these conditions, the AMS can provide a good indicator of shape and crystalline anisotropy of the diamagnetic component which would otherwise be overshadowed.

3) **Ferromagnetism.** Ferromagnetism is characterized by the existence of ferromagnetic domains, in which all magnetic moments are parallel to each other. This effect is specifically the result of unpaired electrons in the 3d shells of the atoms. These electrons share linked spins and their magnetic moments combine with the weak paramagnetic state already in the material. Ferromagnetic materials can orient their electron spins without an external magnetic field and will strongly reinforce an applied magnetic field. This linkage is dependent on the temperature of the material. If the thermal agitation becomes too great the material will revert to paramagnetic behavior due to the Curie law. When a ferromagnetic material is demagnetized, below the Curie temperature, different domains will have different orientations resulting in a net zero magnetization for the material. Under an applied magnetic field, however, these domains will reorient to align with the field direction, and the domain boundaries will migrate to accommodate this reorientation. For low fields this process is reversible, and the domains will revert to the demagnetized state once the applied field is removed. For fields of sufficient strength the magnetization process becomes hysteretic as the domain boundaries will not fully return to their original configurations resulting in a remanent magnetization.

Paramagnetic and Diamagnetic materials can exhibit magnetic susceptibility anisotropy or AMS. The AMS of these materials is largely dependent on the preferred crystal lattice axes (Tarling and Hrouda, 1993). The structure of the lattice will largely control the magnetic easy axis or axis of highest magnetic susceptibility. Additionally, the lattice structure will generally result in preferential grain shapes due to planes of weakness along the crystal structure. Thus the magnetic anisotropy seen in these materials is largely representative of the degree of alignment of the individual grains.

There are several classes related to ferromagnetism which are summarized below. A more detailed description can be found in Spaldin (2010). These classes are related in that they contain magnetic domains which have a non-random orientation when there is no applied field.

1) **Ferrimagnetism** - Ferrimagnetic materials contain domains with two primary sublattices that are in antiparallel to each other within the crystal lattice ***Figure 1*****.** For a material to be classified as ferrimagnetic the magnetic moment of one sublattice must be stronger than the other such that a net spontaneous magnetization remains. Ferrimagnetic materials will act to reinforce an applied magnetic field and will, therefore, have a positive susceptibility. This effect, although similar to ferromagnetism, is lower in magnitude.
2) **Antiferromagnetism** – Antiferromagnetic materials have a similar lattice configuration as ferrimagnetic materials wherein adjacent moments align antiparallel to each other

(see ***Figure 1***) the main difference being that each opposing lattice is identical in its magnitude of magnetization. These equal and opposite orientations result in a zero net spontaneous magnetization. These materials will act to reinforce an applied magnetic field and do display a small positive magnetic susceptibility, however they are unable to maintain a remanent magnetization.

3) **Canted Antiferromagnetism** – this is a special case of antiferromagnetism. These materials are antiferromagnetic, but the domain lattices are canted at a small angle to each other. This small angle results in a small net spontaneous magnetization (***Figure 1***)**.** In reality, canted antiferromagnetism is much more common than pure antiferromagnetism as any crystal defects can add a small angle of offset into the lattice structure. Like antiferromagnetic materials, these materials will act to reinforce the applied magnetic field and have a positive magnetic susceptibility.

It is also important to remember that when heated above their Curie temperature ferromagnetic materials will behave in the same manner as paramagnetic materials and obey the Curie-Weiss law (Tarling and Hrouda, 1993; Lowrie, 2007; Spaldin, 2010). This behavior is the result of thermal agitations within the material overpowering the effects of shape and crystalline anisotropy that are discussed in greater detail below. Heating a ferromagnetic material above its Curie temperature results in randomized magnetic moments within the ferromagnetic grain in the absence of a magnetic field. Therefore an applied field will align these moments in the same fashion as a conventional paramagnetic material.

The different classes of magnetization responses have been summarized schematically in **Figure 1**.

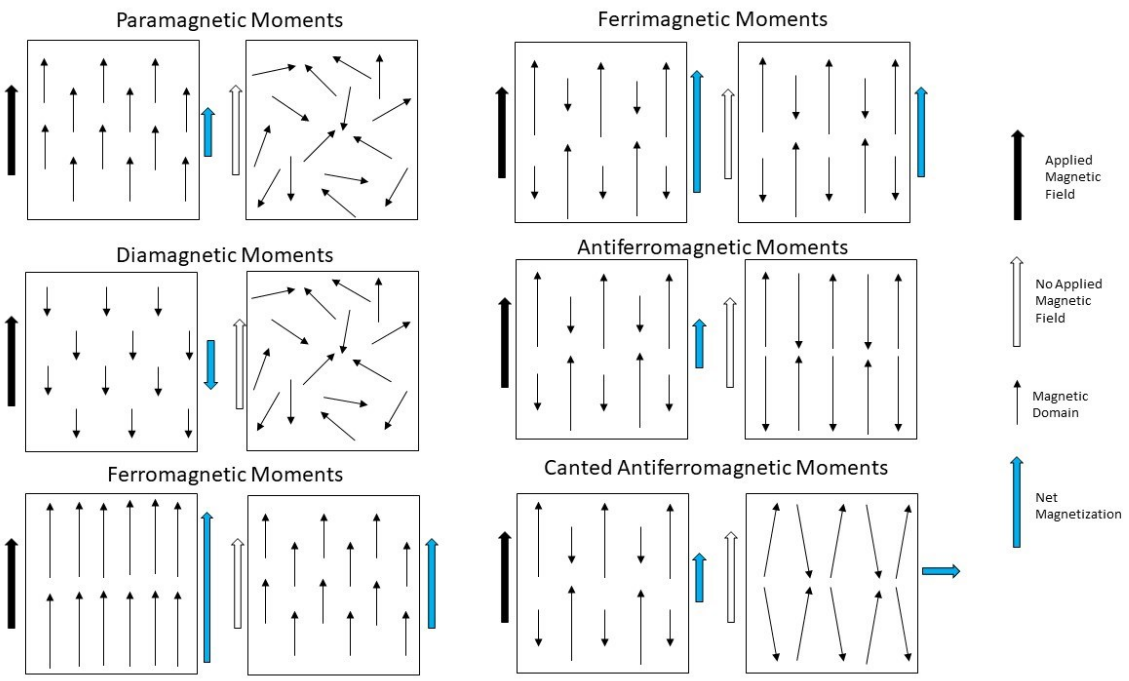

Figure 1: Types of magnetization with and without an applied magnetic field to show various magnetic material behaviors. Solid arrow: applied magnetic field; Blue arrow: Net Magnetization; Hollow Arrow: No applied magnetic field; Thin Arrow: Individual magnetic moment.

When exposed to a strong enough magnetic field ferromagnetic, antiferromagnetic or ferrimagnetic materials will have all of the magnetic domains align with the applied field. At this field strength the magnetization of the material becomes saturated (M_{sat}). However for ferromagnetic and ferrimagnetic materials, once the applied magnetic field is removed a remanent magnetization (M_R) will remain in the sample for sufficiently large grains. The effects of grain size will be discussed in more detail later on in this chapter, but for now, we will assume a sample grain that is sufficiently large enough to contain a stable single magnetic domain and one that is an idealized ferromagnetic material as this response is similar to its ferrimagnetic counterpart. If a residual magnetization is acquired in the manner described above it is more specifically known as an isothermal remanent magnetization or IRM (Potter, 2004; Lowrie, 2007). If the sample has been magnetized to saturation, then the IRM produced when the field is removed will represent the remanent magnetization of saturation (M_{rsat}). If the field direction is reversed, then the material will become magnetized in the direction opposite the original magnetization. As the negative magnetic field is increased eventually the newly induced magnetization will exactly cancel out the previous one resulting in a net zero magnetization. The field required to produce a net zero magnetization is known as the coercive force (H_c).

The magnetic susceptibility for a material is the ease at which it acquires a magnetization which can be represented by the slope of the magnetic hysteresis curve that results from plotting the applied field H vs. the magnetization M. Generally speaking the magnetic field (B) within a material can be expressed as:

$$B = \mu_o(1 + \chi)H \quad (1)$$

where χ represents the magnetic susceptibility for the material, H is the applied external magnetic field and μ_o is the permeability of free space. Generally speaking diamagnetic materials have a weak negative susceptibility value ranging from the order of about $-1x10^{-5}$ to zero (SI), paramagnetic materials have a positive and slightly stronger susceptibility magnitude ranging between zero and about $1x10^{-4}$ (SI), whereas the ferromagnetic materials are much stronger ranging anywhere between 0.5 to 20 (SI) and higher (Tarling and Hrouda, 1993).

1.3 REVIEW OF SMALL SCALE MAGNETISM

The magnetic properties of small ferromagnetic or ferrimagnetic grains are greatly dependant on the size and number of magnetic domains which can be contained within the grain. These domains can be either stable in the case of stable single domain (SSD) grains or unstable superparamagnetic (SP) particles. Grains which support more than one magnetic domain or multidomain (MD) grains are considered to be too large to be classified as a nanoparticle. Diameters associated with transitions from SP to SSD or SSD to MD grains are given for some common minerals in **Table 1**. From this table we can see that the upper limit for these domain transitions is often larger than the nanometer scale and can often be measured in microns (μm). In **Chapter 2** the use of Mn-Zn ferrite nanoparticles will be discussed for applications towards reservoir characterization and hydraulic fracture monitoring. These particles are on average 6nm in diameter and are well below the diameter necessary to support a stable single domain. Additionally they were shown through magnetic hysteresis measurements to be superparamagnetic in nature which is advantageous for magnetic contrast agents due to their very high magnetic susceptibility. Later on in **Chapter 4** the magnetic fabric associated with several rock samples will be discussed and it is shown that these samples are influenced by the presence of primarily MD grains however one sample with a SSD component is observed. The rest of **section 1.3** and **1.4** detail the implications of various magnetic domain configurations which will be useful in understanding the results presented in **Chapters 2 and 4**.

Table 1: Grain diameter for common remanence carrying elements and minerals associated with domain transitions. Each column represents the diameter where a magnetic grain of that mineral transitions from one magnetic state to the next with the first column giving the maximum diameter for a superparamagnetic response above which the particle is considered to be stable single domain. The second column describes the upper limit for a stable single domain diameter, above which only multidomain responses are expected. Modified from (Dunlop and Ozdemir, 1997).

	SP/SSD	**SSD/MD**
Mineral	Superparamagnetic maximum diameter (μm)	Single domain maximum diameter (μm)
Iron	0.008	0.023
Magnetite	0.025-0.030	0.05-0.06
Maghemite		0.06
Hematite	0.025-0.030	15

1.3.1 Ferrimagnetic Materials & Magnetic Remanence Anisotropy

The magnitude of the observed magnetic anisotropy is determined by both the anisotropy of the individual grains (shape, crystalline and elastic) and the degree of particle alignment within the sample. In the case of ferrimagnetic materials, the shape anisotropy is strongly controlled by the number of magnetic domains contained within the particle. A good summary of the causes and effects of magnetic anisotropy can be found in Tarling and Hrouda (1993), Spaldin (2010), however for a more in-depth description see Dunlop and Ozdemir (1997). Three separate effects contribute to the overall magnetic anisotropy seen within a single ferrimagnetic grain; these effects are due to the superposition of magnetocrystalline, magnetoelastic and shape anisotropy.

Certain directions within a crystal lattice are preferred for magnetization, especially at low applied magnetic field strength. The directions which take on a magnetization easily are referred to as the easy axes of the crystal. The source of this anisotropy is a weak coupling between ionic bonding that makes up the crystal lattice and the individual electron spins of each electron. For an in-depth description of this phenomenon see Dunlop and Ozdemir (1997) however, the effects of magnetocrystalline anisotropy are assumed to be weak in comparison to the effects of shape anisotropy unless otherwise stated for ferrimagnetic materials. However, for the cases of diamagnetic and paramagnetic materials, magnetocrystalline anisotropy is the primary control on the observed magnetic fabric. The effects of magnetoelastic anisotropy, which is due to the increased ionic distance along the axis of magnetization (Dunlop and Ozdemir, 1997), are also considered to be small in comparison to the shape anisotropy of the grain.

For ferrimagnetic materials, the shape of the grain will introduce a large degree of anisotropy which generally overshadows the effects of magnetocrystalline and magnetoelastic anisotropy in single domain grains. Every ferrimagnetic grain will acquire a magnetization parallel to the direction of the applied magnetic field, however, this magnetization will be preferentially acquired along the long axis of the grain. This can be applied to various grain shapes. Oblate spheroids, for example, will carry a maximum magnetization along the plane containing the major and intermediate axes with the minor axis containing the lowest magnetization. In the case of spherical grains, there will be no shape anisotropy, and the magnetic anisotropic effects will be due to magnetocrystalline anisotropy. A further description of different shape anisotropies can be found in Dunlop and Ozdemir (1997) however we will focus on the use of oblate and prolate spheroid grains.

1.3.2 Single Domain Particles

A ferrimagnet is said to be single domain when the magnetization does not vary across the magnet for any applied magnetic field. This means that the ferrimagnetic grain will only contain a single magnetic domain. The existence of particles small enough to contain only one magnetic domain was first predicted by Frenkel and Dorfman (1930) who calculated an upper size limit for these particles of 10^{-5}cm. This upper size limit was a large overestimate and was improved upon by Néel (1947) who estimated this critical size to occur when the diameter of a grain was about the same as the thickness of a domain wall. Another estimate for this critical transition diameter was proposed by Kittel (1949) who determined a critical diameter by setting the magnetostatic energy of a single domain structure equal to that of a two domain structure.

Without an applied magnetic field, ferrimagnetic grains will eventually revert to a demagnetized state due to random thermal fluctuations in much the same way as paramagnetic and diamagnetic materials. However, the time it takes for a single domain particle to relax back from an acquired magnetization will vary considerably depending on the grain size and configuration. This time is given by Neel's equation below (Néel, 1955):

$$\tau = \frac{1}{C} e^{\frac{vH_c M_{sat}}{2kT}} \qquad (2)$$

where: v is the volume of the single domain particle, H_c is the coercive force, M_{sat} is the saturation magnetization, and kT is the thermal energy of the system (the Boltzmann constant k multiplied by the temperature T in Kelvin). For simplicity, the frequency factor C is usually set to 10^8Hz.

The effect of particle volume on relaxation time has been seen in small room temperature spherical iron particles. Work done by Néel (1955) illustrated a stark change in relaxation time with changing volume that is shown by a magnetization being held 'indefinitely' for spheres with a diameter of 160 angstrom (Å or 10^{-10} m), whereas slightly smaller iron spheres of 120 Å

were demagnetized almost instantly (less than 0.1s). This rapid change in relaxation time highlighted the effect of a critical diameter and the subsequent division of single domain particles into larger stable single domain (SSD) and smaller superparamagnetic (SP) particles (Bean and Jacobs, 1956).

Superparamagnetic particles can be thought of as the lower limit for which a stable single domain to be maintained without an applied magnetic field. In an SSD state, the magnetic moment is locked into a stable local state by a high activation energy (which is due to a low demagnetizing field along this axis (Dunlop and Ozdemir, 1997)) and thermal fluctuations will cause little deviation from this (Néel, 1949, 1955). In SP particles this activation energy becomes sufficiently small that random thermal agitations can cause frequent random fluctuations in the magnetic state. If the time taken for a measurement of magnetization (τ_m) is much larger than the time taken for a domain to flip (τ) from Néel's equation, then the sample will appear to have a net zero magnetization (Spaldin, 2010). As we can see in Néel's equation the volume of a particle will exponentially influence the relaxation time. A smaller volume is analogous to lowering the activation energy and results in a net zero magnetization for the characteristically small SP particles since $\tau_m >> \tau$. When exposed to a magnetic field, however, SP particles will rapidly acquire a magnetization that is dependent on the applied magnetic field H_o and the temperature T in Kelvin (Dunlop and Ozdemir, 1997).

Superparamagnetic particles do not carry a remanence for any significant amount of time, so the magnetization (as a function of the applied field H) will follow a closed hysteresis curve shown below in **Figure 2**. The curve rises steeply and saturates at relatively low H_o compared to SSD and MD saturation fields due to the low amount of energy (i.e., low applied field strength) required for domain rotation (Dunlop and Ozdemir, 1997). This means that the magnetic susceptibility for SP particles is very high and can be significantly larger than SSD and MD magnetic susceptibilities due to them rapidly acquiring large changes in magnetization at low applied fields.

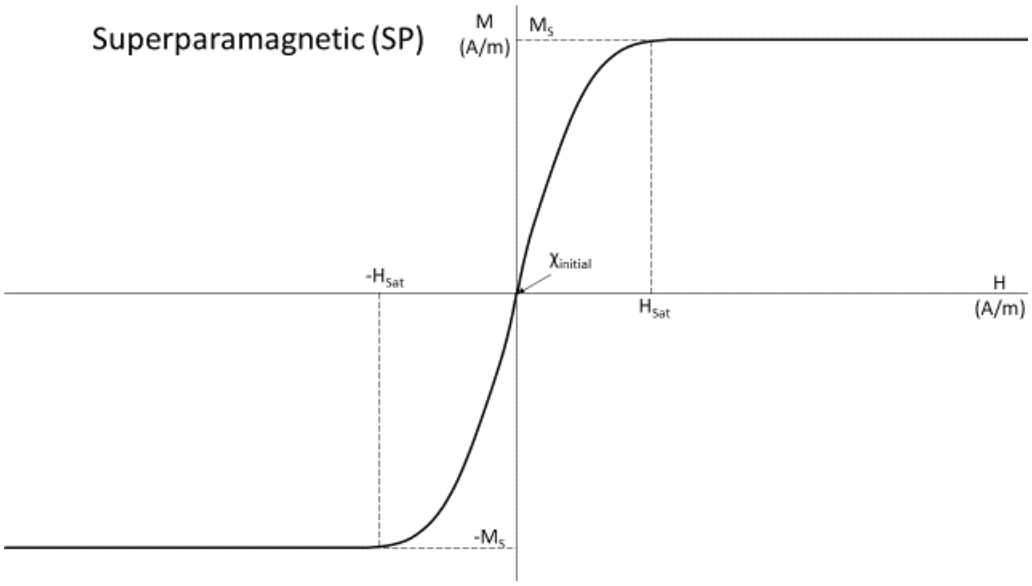

Figure 2: Closed magnetic hysteresis loop as idealized magnetization of a random assemblage of superparamagnetic nanoparticles modified from Dunlop and Ozdemir (1997).

Figure 2 above shows an idealized superparamagnetic magnetization curve (Dunlop and Ozdemir, 1997). It should be noted that the magnetization curve is closed which confirms that there is no magnetization retained in the absence of a magnetic field H due to the fast relaxation time. We can also see that the change in magnetization is rapid especially at low fields and reaches saturation quickly.

Generally speaking, SSD grains have the lowest magnetic susceptibility out of SP, SSD and MD particles as they carry the strongest remanent magnetization. This is especially true for low magnetic fields as the activation energy required to flip a magnetic domain is quite large. This can be seen by the shallow slope in the initial magnetization curve of an assemblage of SSD particles in **Figure** 3 below.

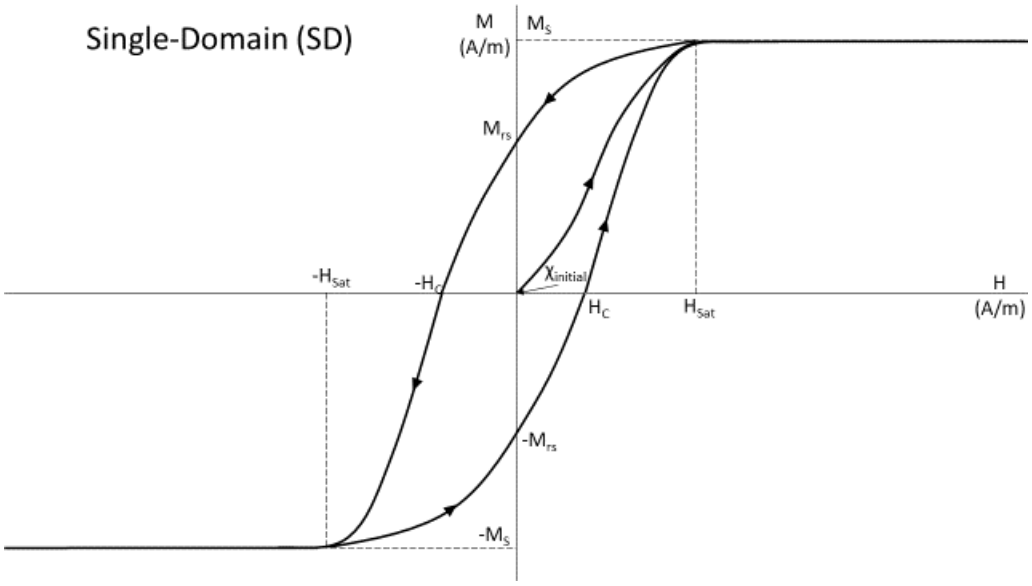

Figure 3: Open hysteresis loop with low initial magnetic susceptibility as an idealized magnetization of a random assemblage of stable single domain nanoparticles modified from Dunlop and Ozdemir (1997).

1.3.3 Multidomain Particles

As theorized by Frenkel and Dorfman (1930) and later refined by Néel (1947) and Kittel (1949) there is an upper size limit for stable single domain particles above which a single domain is no longer the lowest energy configuration. Ferrimagnetic grains that are sufficiently large will spontaneously subdivide themselves into two or more magnetic domains where each has an internally uniform magnetization that can vary in direction and magnitude between the different magnetic domains. These multidomain (MD) grains were first theorized by Landau and Lifshitz (1935) who noted that the long-range effect of dipole-dipole interactions would result in magnetostatic energy that could eventually outweigh the exchange forces and magnetocrystalline anisotropy. This led them to predict basic body and closure domain patterns. **Figure 4** shows an idealized magnetic hysteresis loop for an MD particle assemblage. At low field strengths, MD particles will have a stronger magnetic susceptibility than a comparable SSD grain. This is because there are lower energy mechanisms available to change the magnetization of an MD grain than the domain rotation required for an SSD grain. In order of increasing energy, MD particles can undergo domain wall displacement and domain nucleation before domain rotation. This allows them to have a higher magnetic susceptibility at low fields compared to SSD particles due to the relatively low energy cost of domain wall displacement.

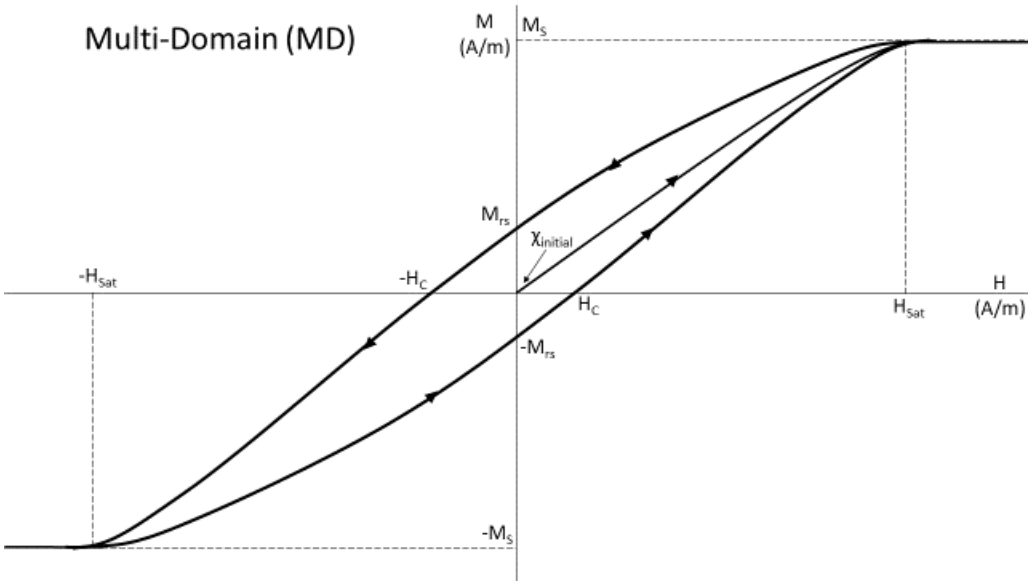

Figure 4: Open magnetic hysteresis loop as an idealized magnetization loop for a random assemblage of multidomain grains of magnetite modified from Dunlop and Ozdemir (1997).

1.3.4 Summary & Applications

In summary of the above sections, we can classify ferrimagnetic particles based on the number of magnetic domains contained within the individual grain. Generally, they are divided between multidomain and single domain particles. Multidomain particles as the name suggests contain at least two magnetic domains, this configuration results in the lowest possible magnetostatic energy for particles above a certain volume. As the grain size is reduced, it will approach a volume that cannot support a domain wall as the lowest energy state and then the system will prefer to contain only one magnetic domain. More specifically the energy required to create a domain wall is larger than the decrease in magnetostatic energy caused by dividing the particle into two domains. A detailed description of this can be found in Dunlop and Ozdemir (1997). In this case, these single domain particles are best thought of as having surface 'magnetic charges' where the magnetostatic energy is then stored in a surface pole distribution. Over time the magnetization carried by a single domain particle will decay according to Néel's equation, and when this relaxation period is below a critical time (less than 100s for most practical purposes), the particle will then be classified as superparamagnetic. Superparamagnetic particles differ from stable single domain particles in that they do not retain any magnetic remanence and they have a much higher magnetic susceptibility than larger particles. Due to their higher magnetic susceptibility, SP particles will be of interest as a magnetic contrast agent, and this application is investigated in **Chapter 2**.

In addition to differences in the magnitude of susceptibility and remanence MD, SSD and SP particles also differ in the direction of their minimum and maximum axes. As is summarized in **Figure 5** below we can see that the major magnetic remanence axis always lies parallel to the long axis of the grain (except for SP particles as they do not carry any remanent magnetization).

Additionally, the magnetic susceptibility axis is perpendicular to the long axis of the grain for SSD particles whereas it is parallel to the grain for MD and SP particles. These relationships described by **Figure** 5 are useful in defining any magnetic fabric that is the result of an assemblage of ferromagnetic particles within a rock sample.

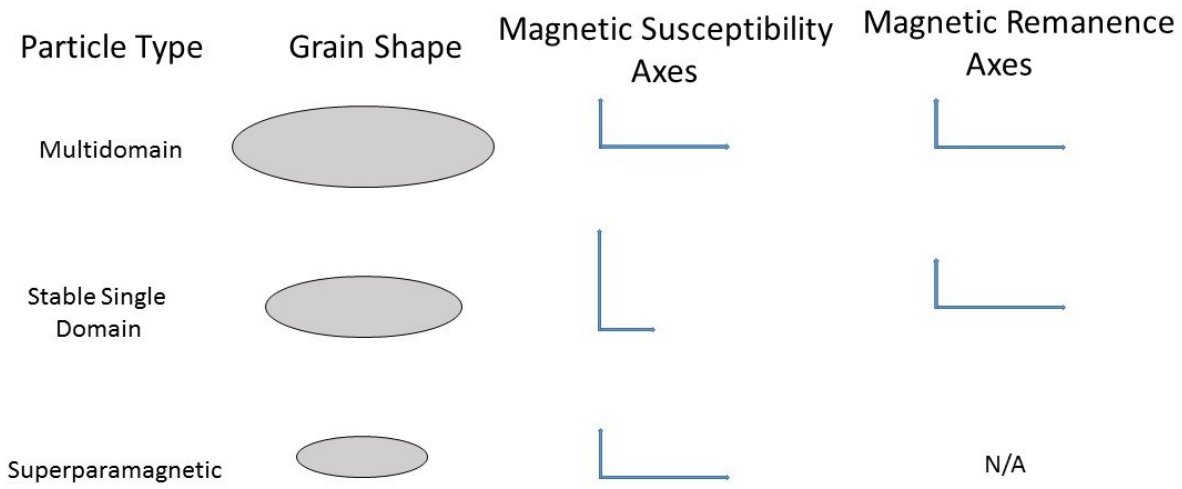

Figure 5: Magnetic remanence always has a major axis along the long axis of the grain except for SP particles which carry no remanence. Maximum magnetic susceptibility for MD and SP particles is along the long axis of the grain; whereas it is perpendicular for SSD particles.

1.4 Magnetic Anisotropy

If we expand on the differences in magnetization and susceptibility for individual SP, SSD and MD particles, we could use them as a way to measure the magnetic character for an assemblage of grains since the magnetic susceptibility and magnetization are the sum of all the individual components resulting in net magnetic susceptibility and magnetization. For many materials, it turns out that the value of magnetization can vary with the direction of measurement as it would with a singular grain. This directional variance in magnetization and subsequently magnetic susceptibility is responsible for the magnetic anisotropy of an object. Magnetic anisotropy in rocks was first observed by Ising (1942) who observed the low field magnetic susceptibility was higher when measured parallel to the bedding of varved clays than when it was measured in the perpendicular direction. Magnetic susceptibility anisotropy has since evolved into a useful tool in quantifying different rock textures and has many applications in paleomagnetic, depositional and structural studies as shown by many workers (Collinson, 1965; Hrouda, 1982; Potter and Stephenson, 1988; Tarling and Hrouda, 1993; Potter, 2004; Borradaile and Jackson, 2010).

There are two main types of magnetic anisotropy that can be looked at, anisotropy of magnetic susceptibility (AMS) and anisotropy of magnetic remanence (AMR). These forms of anisotropy

are controlled by two basic contributing factors (Spaldin, 2010), the first and often lesser magnitude of the two is due to any magnetic preferred orientation from the structure of the crystal lattice itself, the second and usually stronger contributing factor is due to the shape and size of the magnetic grain.

This section will discuss the basic causes and implications for both as well as basic principles of AMS and AMR fabrics. To measure these fabrics at least six independent measurements are needed to fully constrain the orientation and magnitude of the magnetic susceptibility anisotropy ellipsoid. Three of these measurements are required to determine the direction of the principal susceptibility axes relative to the sample axes, and then three more are needed to identify the magnitude of each axis. **Figure 6** below shows a schematic diagram of the anisotropy ellipsoid with the principle axes marked to indicate the maximum, intermediate and minimum axes of anisotropy respectively.

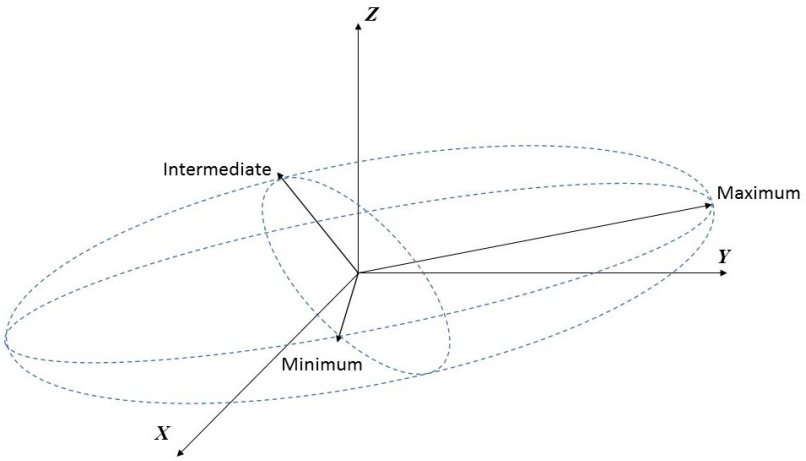

Figure 6: Arbitrary 3D ellipsoid used to describe a magnetic fabric through the orientation and magnitude of the maximum, minimum and intermediate AMS and AMR principle axes.

The advantage of magnetic susceptibility measurements over other techniques of anisotropy such as acoustic velocity measurements or X-Ray fluorescence is that they are relatively quick to acquire, inexpensive, non-destructive and can be accomplished with less sample material. The shape of this anisotropy ellipsoid can be used to help quantify various magnetic fabric characteristics such as lineation, foliation, and degree of anisotropy. However, there is some ambiguity due to the presence of ferrimagnetic particles where even a small amount can overshadow the paramagnetic and diamagnetic components in the AMS ellipsoid (Potter, 2004). It is also possible for a net magnetic susceptibility to be near zero if there exists the correct ratio and orientation between the ferromagnetic, paramagnetic, and diamagnetic components within the material. This ambiguity is one of the drawbacks for the AMS ellipsoid method. However, when combined with the use of magnetic remanence anisotropy it is possible to better constrain the system by isolating various subfabrics.

AMR studies are useful in that they are only influenced by remanence-carrying particles (i.e., ferromagnetic, ferrimagnetic and canted antiferromagnetic minerals) whereas AMS measurements are the sum of all contributions from all minerals in a rock sample (remanence carrying as well as diamagnetic and paramagnetic). AMS is also limited in the fact that it is strongly dependent on the size of the sample's ferromagnetic or ferrimagnetic particle components. The relationship between AMS and the size and shape of these particles is complex (as shown in **Figure 5**) in that the direction of the maximum susceptibility axes can change from along the long axis of a particle (Potter and Stephenson, 1988; Potter, 2004; Borradaile and Jackson, 2010) as is the case for superparamagnetic (SP) and multidomain (MD) particles to lying perpendicular to the long axis as is the case of stable single domain (SSD) particles. This variation is not seen with AMR techniques as the maximum remanence is always along the long axis of the grain. These changes in the magnetic fabric can be used to identify the type of remanence carrying particles present in a sample, their size and their orientations (Stephenson, S. Sadikun, et al., 1986; Potter and Stephenson, 1988; Potter, 2004; Borradaile and Jackson, 2010). When coupled with AMS we can use this to help define a magnetic rock fabric for the sample that can be used to identify the size, shape and any preferred orientation of the magnetic grains within the rock.

1.4.1 Magnetic Anisotropy & Implications

The directions and magnitudes of the principle AMS or AMR axes are generally related to the rock sample texture. AMS is the result of contributions from any lattice preferred orientation (LPO) of minerals that compose the sample as well as the effects of shape anisotropy due to the grains themselves. AMS has been widely used in the field of structural geology to determine a strain history for the rock as it is a sensitive indicator of rock texture. Additionally, AMS can provide valuable information about the origin of the rock as well as its structural evolution (Hrouda, 1982; Housen and van der Pluijm, 1991; Mattei et al., 1997; Hrouda and Ježek, 1999; Borradaile and Jackson, 2010; Arbaret et al., 2013; Dubey, 2014; Ferré et al., 2014). Generally speaking for deformed rocks the magnetic susceptibility lineation is parallel to the direction of extension and the maximum magnetic susceptibility axis. Conversely, the orientation of the minimum susceptibility axis is generally parallel to the direction of maximum shortening. This technique shares many similarities with elastic anisotropy as both are dependent on the preferred orientation of anisotropic crystals as well as the orientation of the mineral grains themselves (Han, 2005; Martínez and Schmitt, 2016). AMS and elastic anisotropy are also similar in that they represent contributions from all the constituent components of a sample.

There are several sources of natural remanent magnetization (NRM), and it is not uncommon to have a superposition of various magnetization sources. A good overview of the different kinds of NRM can be found in Dunlop and Ozdemir (1997), but in general the different sources can be broken up into three categories. The first cause of NRM is thermoremanent magnetization (TRM); this is acquired by the sample cooling to a temperature below the Curie point for the magnetic remanence carrying components. This method will often give the strongest indication

of the Earth's magnetic field at the time of cooling as the magnetic domains are locked along the paleomagnetic field direction. A strong TRM signal is commonly found in metamorphic and igneous rock samples. The second classification of NRM is chemical remanent magnetization (CRM), due to chemical changes or new crystal growth within the rock sample sometime after deposition and is most common in sedimentary and metamorphic rocks. The third source of NRM is depositional remanent magnetization (DRM). This is acquired during the deposition of sediments as the magnetic components will align along the direction of the Earth's magnetic field while in suspension and retain the azimuthal component of this field. Note for higher energy deposition environments it is possible for the preferential alignment of these grains to be controlled by current flow direction (Tarling and Hrouda, 1993).

These sources of NRM are the primary interest for paleomagnetic studies, and as such the remanence must be measured with respect to their original orientation at the time of collection allowing us to determine the Earth's magnetic field at the time of formation. However to make observations about the shape and distribution of the remanence carrying grains themselves this natural magnetization must be removed by first demagnetizing the sample and then inducing a controlled laboratory remanence (Potter, 2004). The distribution of the magnetic grains and their relative sizes can be used to help infer rock fabric information such as paleocurrent directions in sedimentary rocks, flow direction for igneous rocks and determination of stress orientation in metamorphic rocks. The orientation of the magnetic susceptibility ellipsoid to can be used in conjunction with the remanence ellipsoid to remove ambiguity in these characteristics of the rock fabric (Dubey, 2014).

1.5 SEISMIC ANISOTROPY

1.5.1 Basics of Elastic Materials

Seismic methods can be used to identify many rock properties, and is one of the most commonly used data types in oil and gas exploration. In the petroleum industry, there is extensive use of sonic velocity logs to help with formation characterization. This log data can give information on density, porosity, fractures and even fluid content. In general, seismic waves will travel through the body as either a compressional *p-wave* or as a transverse shear or *s-wave* and respond to all of the previous factors (Lowrie, 2007). The velocities for the *p-wave* (v_p) and the *s-wave* (v_s) are dependent on the material properties particularly the bulk modulus K, the shear modulus μ and the bulk density ρ such that:

$$v_p = \sqrt{\frac{K + \frac{4}{3}\mu}{\rho}} \tag{3}$$

$$v_s = \sqrt{\frac{\mu}{\rho}} \tag{4}$$

Where the bulk modulus is the resistance to uniform compression, and the shear modulus is the resistance to shearing. These parameters are defined as follows:

$$K = -V\frac{dp}{dV}$$

$$\mu = \frac{\sigma_{shear}}{\varepsilon_{shear}}$$

where p is the applied pressure, V is the volume, and dp/dV is the infinitesimal change in pressure with respect to volume. For the shear modulus, σ_{shear} is the shear stress, and ε_{shear} is the shear strain. From these equations, we can see that for the same material, the *P-wave* will always have a higher velocity and is, therefore, the first arrival (Lowrie, 2007). The main distinction between a P and an *S-wave* is that for *P-wave*s the direction of particle movement is parallel to the direction of wave propagation, whereas *S-wave*s have particle motion in a direction perpendicular to the propagation direction. The above equations describe the velocity of these waves when they pass through an isotropic medium. However Earth materials are rarely isotropic, and the seismic wave velocity will often change based on the direction of observation. This anisotropy can be controlled by a variety of factors and understanding it can give us useful geological information such as rock texture, porosity information and preferred crystallographic orientation.

1.5.2 Seismic Anisotropy

It is important to understand the effect that rock texture has on seismic wave velocity anisotropy since seismic surveys or sonic log data is much more readily available for in-situ observations of a rock formation than the rock fabric itself. Therefore any relationship between the rock fabric and seismic anisotropy can be used to help define a rock fabric based on observed anisotropy patterns. Seismic wave velocities and their subsequent anisotropy are controlled by a variety of factors which include: preferred crystallographic orientation, porosity, temperature, pore fluid content, tectonic stresses and mineral grain distribution to name a few (Cholach et al., 2005; Martinez, 2014). Knowledge of these processes and how they influence the seismic velocity structure is useful in defining geologic structures and processes in a region.

Many studies have been done to link seismic wave anisotropy with observed rock fabrics. Birch (1960, 1961) for example, measured a non-linear increase in *p-wave* velocities with confining pressure. This was attributed to the closure of pores within the rock, particularly cracks and microfractures. There have since been many other works done in the field of seismic anisotropy (Gangi and Carlson, 1996; Dewhurst and Siggins, 2006; Martinez, 2014; Martínez and Schmitt, 2016). Seismic characteristics often vary based on lithology, and because of this there has been

much work done to empirically characterize the seismic properties of various rock types. There have been extensive laboratory studies done to characterize P and *S-wave* anisotropies within various rock types (Birch, 1960, 1961; Johnston, 1987; Johnston and Christensen, 1995; Vernik and Liu, 1997; Han, 2005; Sayers, 2005; Dewhurst and Siggins, 2006; Miller et al., 2013; Martinez, 2014).

Mathematically speaking, the description of the elastic anisotropy of a rock requires a 4^{th} rank tensor that consists of up to 21 independent constants (Nye, 1957). This, of course, differs from the 2^{nd} order tensor in the case of magnetic anisotropy with only six independent coefficients. This tensor can have fewer independent coefficients depending on any symmetries within the present anisotropy. The mathematical details for the stiffness tensor and the different classes of symmetry are left to **Chapter 4**.

It was noted earlier that seismic wave velocities are often dependant on the direction of propagation through the anisotropic material. This general statement holds for both compressional *p-wave*s as well as the transverse *s-wave*s however each wave type is affected differently. For example, *p-wave*s will generally travel with a faster velocity if they are propagating in the plane of foliation vs. normal to it and will generally display a continuous velocity change for any intermediate angles of incidence (Nye, 1957; Martinez, 2014). *S-wave*s, however, are also very strongly controlled by the polarity of the wave vs. the foliation plane. An S-wave traveling through an anisotropic medium will split into two perpendicular components or polarizations (Nye, 1957). This is commonly referred to as shear wave splitting and is illustrated in **Figure 7** and has been the subject of many studies (Crampin, 1985; Vinnik et al., 1989; Sayers, 1994; Cholach, 2005; Crampin and Peacock, 2005; Martinez, 2014). Generally, the wave with polarity parallel to the plane of foliation will travel with a faster velocity than the one with polarity perpendicular to the foliation, causing two separate *S-wave* arrivals which contain valuable information in determining the elastic coefficients.

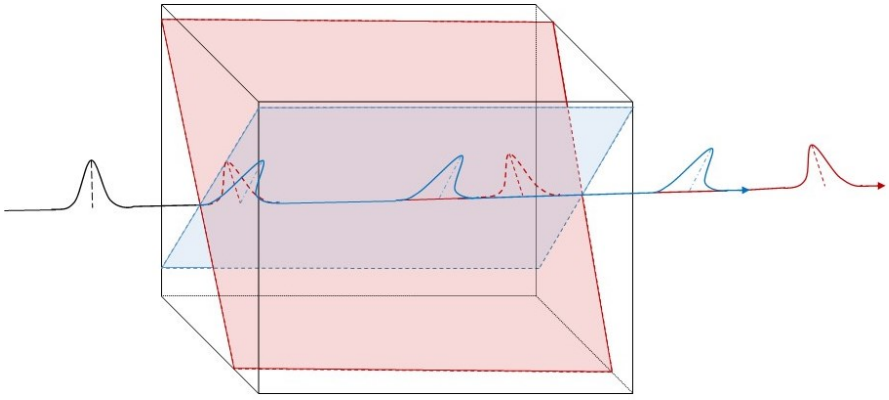

Figure 7: Schematic diagram of shear wave splitting, faster propagation along the red plane than along the blue plane.

It is also important to note the influence of small cracks or microfractures present in the samples studied. The effect of these cracks is to introduce a non-negligible contribution of anisotropy which decreases with increasing pressure as these cracks are closed. If these microfractures share a preferred orientation, then they can contribute to an observed symmetry in the anisotropy. For shallow crustal studies, these oriented fractures could be used as an indicator for the stress regime where they will form parallel to the maximum and intermediate stresses (Cholach et al., 2005; Martinez, 2014). The effect of these microfractures on a seismic signal with a wavelength much larger than the crack spacing has been shown to act as a transversely isotropic medium with the axis of symmetry perpendicular to the fracture plane. For the samples studied in this work, it is important to note that these fractures do impact the previously observed seismic velocities and are also responsible for some degree of shear wave splitting (Martinez, 2014). In order to potentially remove the contribution of these fractures to the anisotropy, it is necessary to conduct the ultrasonic measurements at a high confining pressure so as to close as many cracks as possible. This will allow the isolation of the intrinsic properties of the rock minerals with minimal contributions from porosity. One benefit of magnetic measurements is that they may be conducted at standard atmospheric pressure as they can be independent of porosity if the mass magnetic susceptibility is used.

1.6 Comparative study motivation

The Trans Hudson Orogen and the Flin Flon Belt, in particular, have been the subject of many studies due to the existence of large economic mineral deposits. It was for this reason that these samples were investigated for their acoustic anisotropy by (Cholach et al., 2005) who go into greater detail about how the elastic parameters for various metamorphic samples vary due to confining pressures.

The Trans Hudson Orogen ranges from northern Quebec, west into Saskatchewan and south through to South Dakota (Cholach et al., 2005). The samples were sourced from eastern Saskatchewan directly west of the provincial border and town of Flin Flon Manitoba. The rock from this area can be separated into plutonic and non-plutonic rocks (Ashton et al., 1988; Cholach et al., 2005). See Lucas et al. (1994, 1996) for a more in-depth description of the geologic processes in the area. The samples studied in this thesis are primarily metamorphosed igneous rocks ranging in composition from felsic to mafic. They were sourced from the Granite lake metavolcanics, Granite Lake and Nesootao Lake plutons and Nesootao Lake metavolcanics.

For this thesis, we investigated a subset of these same samples to determine if the magnetic fabric does indeed match the previously determined elastic constants. In particular, the relationship between the magnetic signatures (AMS and ARM) and the fast, intermediate and slow directions of the rock samples will be investigated. The goal of this is to determine a potentially faster more material-efficient method to identify the principle component directions necessary for measuring a sample's acoustic anisotropy which can be a time-consuming process.

1.7 Summary of Chapters

This thesis is organized into 5 different chapters that are as follows:

Chapter 1 discusses the magnetic properties of small ferrimagnetic grains to determine the behaviors of superparamagnetic, stable single domain and multidomain grains, diamagnetism, Paramagnetism and ferro/ferrimagnetism. This is then expanded upon to include some of the background theory detailing basic causes of rock anisotropy for the AMS, AMR and acoustic results.

Chapter 2 is meant to quantify the magnetic characteristics of the Zn-Mn ferrite nanoparticles that were studied for use as a reservoir contrast agent. There will first be a short review of their synthesis, size, composition, and measured characteristics. The methods used to characterize these particles will be discussed in detail particularly the sample preparation, Curie point analysis, risk of oxidation, magnetic susceptibility and saturation magnetization. These results will then be summarised and recommendations for future work will be given.

Chapter 3 gives some background theory for elastic anisotropy and various anisotropic symmetries are explored. The previous and external to this thesis measurement of p-wave anisotropy with confining pressure is presented. This past work was supplemented by additional s-wave measurements taken for this thesis and all are discussed in terms of observable rock fabric within a sample set.

Chapter 4 begins with a short review of the background theory for magnetic anisotropy. The methodology of various magnetic anisotropic methods are examined, specifically: AMS, AIRM, and GRM. The magnetic fabric for the anisotropic rock samples discussed in **Chapter 3** is characterized with these methods and is then compared to the previous elastic anisotropic

measurements. Select core plugs are presented and correlations between the different anisotropic measurements are discussed.

Chapter 5 summarizes the conclusions for this thesis and details recommendations for future work.

1.8 Objectives

This thesis has two main objectives:

Objective 1: Investigate the magnetic properties for various compositions of Mn-Zn ferrite nanoparticles. This is to determine their usefulness as magnetic contrast agents in comparison to nanomagnetite. Particular care will be given to the mass magnetic susceptibility and saturation magnetization for each composition at both room temperature (20^{o}C) and at elevated reservoir temperature (125^{o}C). The relation of these properties for the various particle compositions will be compared with the Curie temperatures of each as they are most likely linked.

Objective 2: Determine any correlations between various magnetic anisotropic methods and acoustic anisotropic methods. This is done to determine if the magnetic results could be used to rapidly predict the orientation and magnitude of acoustic anisotropy within each sample. Compressional (p-wave) and transverse (s-wave) velocity anisotropies for various metamorphosed rock samples were determined. It is expected that there will exist a relationship between the anisotropy of magnetic susceptibility and the acoustic anisotropies as both of these methods measure contributions from all of the constituent minerals within a rock sample. In low porosity samples the acoustic measurements are primarily controlled by the lattice preferred orientation of constituent minerals and this is the primary control over the AMS fabric as well. However, a very small volume of ferrimagnetic material will be able to dominate the magnetic susceptibility signal so care must be taken when interpreting the anisotropy of magnetic susceptibility results. The anisotropy of isothermal remanent magnetization and gyroremanent magnetization will be measured in order to further delineate any ferrimagnetic contribution towards the magnetic fabric within a sample. This ferrimagnetic fabric does not necessarily need to align with the paramagnetic and diamagnetic magnetic fabric. However, in the case of metamorphic rocks it is possible that the ferrimagnetic minerals experienced the same deformation as the other mineral components and their orientations should be related.

CHAPTER 2: MAGNETIC PROPERTIES OF MANGANESE-ZINC FERRITE NANOPARTICLES

Some of the work presented in this chapter has been published as:

Lauren Morrow, Brendan Snow, Arfan Ali, Samuel J. Maguire-Boyle, Zeyad Almutairi, David K. Potter & Andrew R. Barron (2018) Temperature dependence on the mass susceptibility and mass magnetization of superparamagnetic Mn-Zn-ferrite nanoparticles as contrast agents for magnetic imaging of oil and gas reservoirs, Journal of Experimental Nanoscience, 13:1, 107-118, DOI: 10.1080/17458080.2018.1426894

This is an Accepted Manuscript of an article published by Taylor & Francis in the Journal of Experimental Nanoscience in January 2018, available online:*http://wwww.tandfonline.com/DOI*

2.1 INTRODUCTION

There is a large demand for hydrocarbons used in commercial products and fuels (OPEC, 2014). However, the prolonged use of hydrocarbons over the past century has unfortunately caused a depletion of many large conventional reservoirs. This has forced exploration efforts to change focus and look for more unconventional reservoirs, that while more difficult to produce from are far more numerous and relatively untapped. Of these, tight shale reservoirs have undergone major development in the last two decades (Dammel et al., 2011; Nicot and Scanlon, 2012). These shale reservoirs are often the source rocks for more traditional conventional plays which have not yet released all of their contained hydrocarbons due in part to the low permeability of shales (nD – μD). However, enhanced recovery techniques are needed to develop the resources in the shale reservoir intervals in order to overcome the challenges that are due to these low permeabilities. Of the various enhanced recovery methods, hydraulic fracturing has seen the most use for tight shale intervals. This practice involves the injection of high-pressure fluids into the formation which will stimulate a fracture near the wellbore. When combined with horizontal drilling techniques large volumes of shale reservoir can be fractured to allow for economic hydrocarbon recovery. While effective, this technique does have some drawbacks, including uncontrolled damage to the reservoir rock, uncertainty in proppant distribution and environmental concerns. To answer these questions, and obtain the maximum production from a well, more information is needed about the fracturing process (Sahimi, 2012).

There are methods in place to monitor the success of a frac job such as the use of microseismic monitoring, which can detect the distance and direction of fracture propagation as well as various well logging tools such as nuclear magnetic resonance (NMR) or formation micro imaging (FMI) logs, which can be used to identify fractures in the borehole wall. In addition to these, other methods of characterization are being developed such as the use of conductive polymers or proppant tracking materials (Nguyen and Fulton, 2006; McDaniel et al., 2012). This

chapter will serve to highlight the magnetic properties of manganese-zinc ferrite nanoparticles under various reservoir conditions. The primary use of these ferrites will be their use as magnetic contrast agents, which will allow for a measurement of proppant distribution. The unique nature of these particles also lends to their use as a way to effectively monitor pollution and enforce environmental concerns. They can act as a unique fingerprint for a company's fracture fluid, allowing for identification of pollutant sources. In addition to this, they have the added benefit of being non-toxic, which makes them a favorable alternative to radioactive or chemical tracer agents.

Various species of nanoparticles have been investigated for their use as possible contrast agents for proppant distribution and characterization. Previously the use of nanoscale magnetite (nMag) was investigated for this purpose due to its nontoxic nature and high magnetic susceptibility, which has also allowed it to see some analogous use in the medical field (Sun et al., 2008; Roca et al., 2009) as it provides a strong contrast with nearby tissue. Specifically, nMag was previously studied to evaluate its magnetic signal to noise ratio and therefore usefulness against two different types of proppants (sand or ceramic) under both surface and reservoir conditions (Morrow et al., 2014). From this, it was determined that 0.269g/L and 1.01 g/L of nMag are necessary to differentiate a magnetic signal against the sand and ceramic proppants respectively. This equated into roughly 15,000kg of nMag being necessary to characterize a well using sand proppant and 56,000 kg for ceramic. These amounts only account for the effects of the proppant, however a typical shale reservoir rock will typically be paramagnetic and have a higher magnetic susceptibility. In order to overcome this added effect it was shown that at least 86,400 kg of nMag would be necessary to properly contrast with the reservoir at ambient room temperature (Morrow et al., 2014). Fortunately, a typical shale is largely comprised of paramagnetic clays such as illite, which will decrease in magnetic susceptibility with higher reservoir temperatures according to the Curie law (Ali and Potter, 2012). Typical reservoir temperatures range between 120^{o}C and 150^{o}C. According to a model given by Ali and Potter (2012) these temperatures will result in a decrease of magnetic susceptibility of up to 30% from the susceptibility measured at room temperature for simple compositions of 80% illite and 20% quartz. This would require less nMag to properly contrast an average shale reservoir at 120^{o}C - 150^{o}C vs. 20^{o}C, however, it was shown for a simple case that this would only reduce the required nMag to 63,000 kg (Ali and Potter, 2012). However, it was also noted that shales could be highly variable and for one such case a shale with a higher magnetic susceptibility required significantly more nMag, with 242,000kg needed for an ambient temperature of 20^{o}C and about 169,000kg for a temperature of 150^{o}C. In either case, the higher reservoir temperature would reduce the amount of magnetite needed, however it will still be a significant volume making the use of nMag cost prohibitive. One way to address this problem is to investigate different types of magnetic nanoparticles with higher magnetic susceptibilities, which could produce a higher signal to noise than nMag.

The Mn-Zn particles studied in this thesis are classified under the spinel ferrite category. Of particular interest will be the Curie temperature for each particle type studied (where the

magnetic susceptibility drops close to zero following the Curie law) due to the elevated reservoir temperatures which typically range between 120^{o}C and 150^{o}C. The superparamagnetic Mn-Zn ferrites studied have shown high magnetic susceptibility, which makes them of particular interest for use as magnetic contrast agents (Rath et al., 2002). Furthermore, these Mn-Zn ferrite nanoparticles are a useful monitoring tool due to their small diameter which allows them to be easily transported through the shale reservoir despite its low porosity and permeability. This has favorable implications towards their use as a fluid tracer as they will be able to flow through tighter rock formations. A magnetic susceptibility and Curie temperature measurement of fluids taken from monitoring wells should be sufficient to determine the source of contamination and allow it to be traced back to the operator responsible. They are also advantageous in that their surface properties can be changed to influence their mobility (Maguire-Boyle et al., 2014) while the core of the particle can be engineered to give various properties that can be measured (Byerlee and Johnston, 1976; Barron et al., 2010; Cocuzza et al., 2012). More specifically, the dependence of mass susceptibility and mass magnetization on the temperature and composition of various ternary Mn and Zn ferrites will be investigated and used to determine the amount of ferrite necessary per well to provide a good magnetic contrast with the reservoir. The nontoxic nature of these particles means that they could be applied to both hydrocarbon and water bearing reservoirs.

2.2 NANOPARTICLE COMPOSITION & KNOWN CHARACTERISTICS

2.2.1 Composition and Synthesis

Superparamagnetic Mn-Zn ferrite ($Mn_xZn_{1-x}Fe_2O_3$) nanoparticles are known to have a high magnetic susceptibility (Morrow, 2015). The particles used in this study are classified as an Mn-Zn ferrite spinel (Lima et al., 2006); the synthesis for which is a thermal decomposition reaction of various metal acetylacetonate complexes (Morrow, 2015; Orbaek et al., 2015). For these compositions, it was shown that their magnetic ordering is due to a super-exchange interaction between the metal ions in the A tetrahedral and B octahedral sites (Lima et al., 2006; Morrow, 2015). By including the weakly magnetic Zn a reduction in the magnetic exchange between sites A and B is achieved. Therefore altering the Zn content should cause a change in the magnetic properties of the nanoparticles. It was shown that the composition of these particles is controlled by the relative ratio of the reagents present, and this was used to produce a range of known compositions (Morrow, 2015; Orbaek et al., 2015). The samples studied in this chapter are the same as those studied in Morrow et al. (2014) and the results of **Chapter 2** in my thesis have been published in Morrow et al. (2018). The particles themselves and their compositions based off of stoichiometry are given in **Table 2.**

The synthesis, at Rice University (Morrow et al. 2018), was carried out in an oxygen-free environment where the ratio of metal (2mmol) to surfactant was kept constant (Morrow et al., 2014, 2018; Orbaek et al., 2015) and is as follows:

In the general synthesis, 1,2-hexadecanediol (0.3876 g, 1.5 mmol), oleic acid (951.1 mL, 3 mmol), and oleylamine (987.1 mL, 3 mmol) in benzyl ether (37.5 mL, 197.28 mmol) were used for each run. The variation in the Mn:Zn ratio for the resulting nanoparticles was controlled by varying the relative amounts of the Mn precursor $Mn(acac)_2$ and the Zn precursor $Zn(acac)_2$ during synthesis. After all the chemicals were added argon was then flushed through the system to remove any oxygen. The system was then heated to 200 ^oC at a rate of 10 ^oC/min. The temperature was then held constantly at 200 ^oC for two hours after which the heating was increased to reflux at the same rate of 10 ^oC/min. Once refluxing, heating was held constant for one hour. After one hour, the heating was turned off, and the entire system was cooled to room temperature. Ethanol (40 mL) was added to the solution to precipitate out the nanoparticles. The solution was then split into 50 mL centrifuge tubes and centrifuged. The supernatant was discarded, and ethanol (15 mL) was added to each tube to wash the nanoparticles. The samples were centrifuged and washed twice more, discarding the supernatant each time. After washing, the nanoparticles were then air dried overnight (Morrow et al., 2018). The previous work (Orbaek et al., 2015) indicated that this washing procedure was sufficient to remove contaminants.

Table 2: Relative stoichiometric Zn and Mn content for the ferrite nanoparticles studied.

Sample	*Mn*	*Zn*	*Mn:Zn*
LEHI 54b	*0.4*	*0.6*	*0.67*
LEHI 62d	*0.7*	*0.3*	*2.33*
LEHI 14a	*1*	*0.9*	*1.11*
LEHI 17b	*0.2*	*0.8*	*0.25*
LEHI 50b	*0.5*	*0.5*	*1.00*

2.2.2 Size & Mobility

Since zinc is slightly smaller than manganese it is expected to see a slight decrease in lattice size as the relative Zn content is increased (Rath et al., 2002; Arulmurugan et al., 2005). This decrease in size will cause some spin canting and an increased magnetization with higher Zn content. The average size of the various nanoparticles studied was determined by the use of small angle X-ray scattering. The particle size was shown to not be significantly influenced by changes in composition with the average particle diameter being 7 nm with a narrow size distribution as shown in **Figure 8** (Morrow, 2015; Orbaek et al., 2015; Morrow et al., 2018). This uniformity is important to maintain for useful comparisons between the various compositions as magnetic properties are influenced by particle size. The particles are also near spherical, so any effects due to shape anisotropy will be negligible.

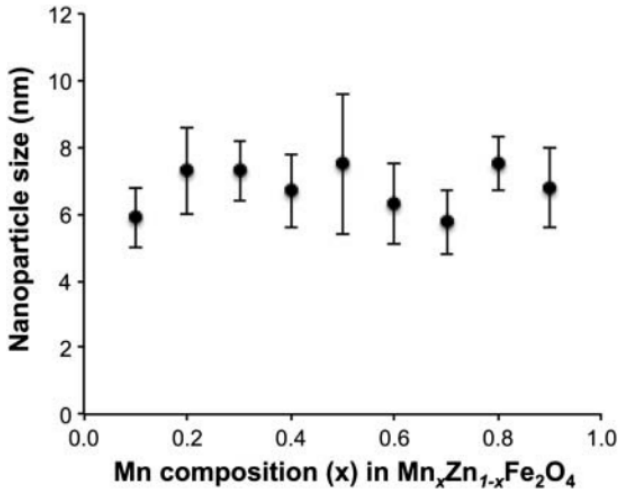

Figure 8: Dependence of Mn:Zn ferrite nanoparticle size as a function of Mn concentration used in synthesis. The diameters of these nanoparticles were determined through x-ray diffraction measurements and the error bars represent the measured size distribution for each composition. (Orbaek et al., 2015; Morrow et al., 2018).

2.2.3 Temperature Dependence

The characterization of mass susceptibility for these nanoparticles was initially done through the use of a Quantum Design MPMS SQUID System at Rice University that was equipped with a high-temperature furnace. The mass susceptibility as a function of the Mn:Zn ratio was tested in a low field of 17.5 mT and is shown in ***Figure 9***.

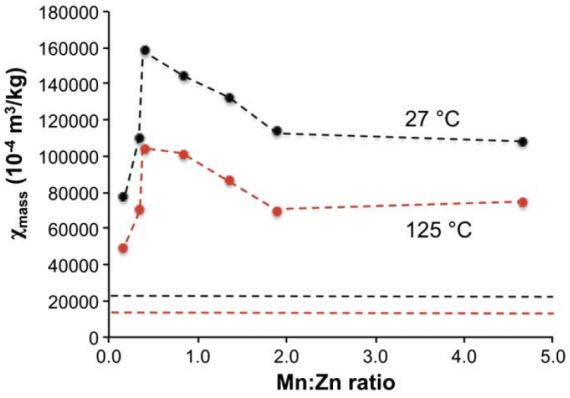

Figure 9: Mass susceptibility (X_{mass}) as a function of the Mn:Zn ratio of Mn-Zn ferrite nanoparticles measured at 27°C (black) and 125°C (red). The dashed line represents nMag values.

It was shown that the Mn-Zn ferrite particles have higher positive magnetic susceptibility values than the previously studied nMag (dashed line) at both temperatures that were studied. The mass susceptibility shows a dramatic increase with the initial increase of the Mn:Zn ratio (an increase of x in $Mn_xZn_{1-x}Fe_2O_3$) up until a ratio of 0.4 where the susceptibility peaks at about

6.5x that of magnetite when considered at reservoir temperatures (127 ^{o}C) or 7.5x at 27^{o}C. Ratios of Mn:Zn higher than 0.4 resulted in a decrease of mass susceptibility until a ratio of 2 after which the susceptibility maintained a constant value with relative increasing Mn content (Morrow, 2015). This trend is shared for both temperatures studied. From this trend the use of nanoparticles with an Mn:Zn ratio of 0.4 (i.e. $Mn_{0.28}Zn_{0.72}Fe_2O_3$) could result in a significant decrease in nanoparticles needed to contrast a well, from 35 mg/L for a sandstone reservoir and 0.205–1.73 g/L for a shale reservoir. A variable field translation balance (VFTB) was then used to more accurately determine magnetic saturation and susceptibility values with help from Arfan Ali in the UK. These measurements are given in **Figure 10** through **Figure 14 .** These results clearly show that the slope or mass susceptibility drops with an increase in temperature due to the Curie Law as does the magnetic saturation value. The degree of this drop is thought to be related to the Curie temperature for each sample. Additionally, we can see that the hysteresis loops are closed which indicates that these particles are superparamagnetic and that they give the highest saturation magnetization and magnetic susceptibility at room temperature (20^{o}C) when compared to their values at higher reservoir temperatures up to (125^{o}C).

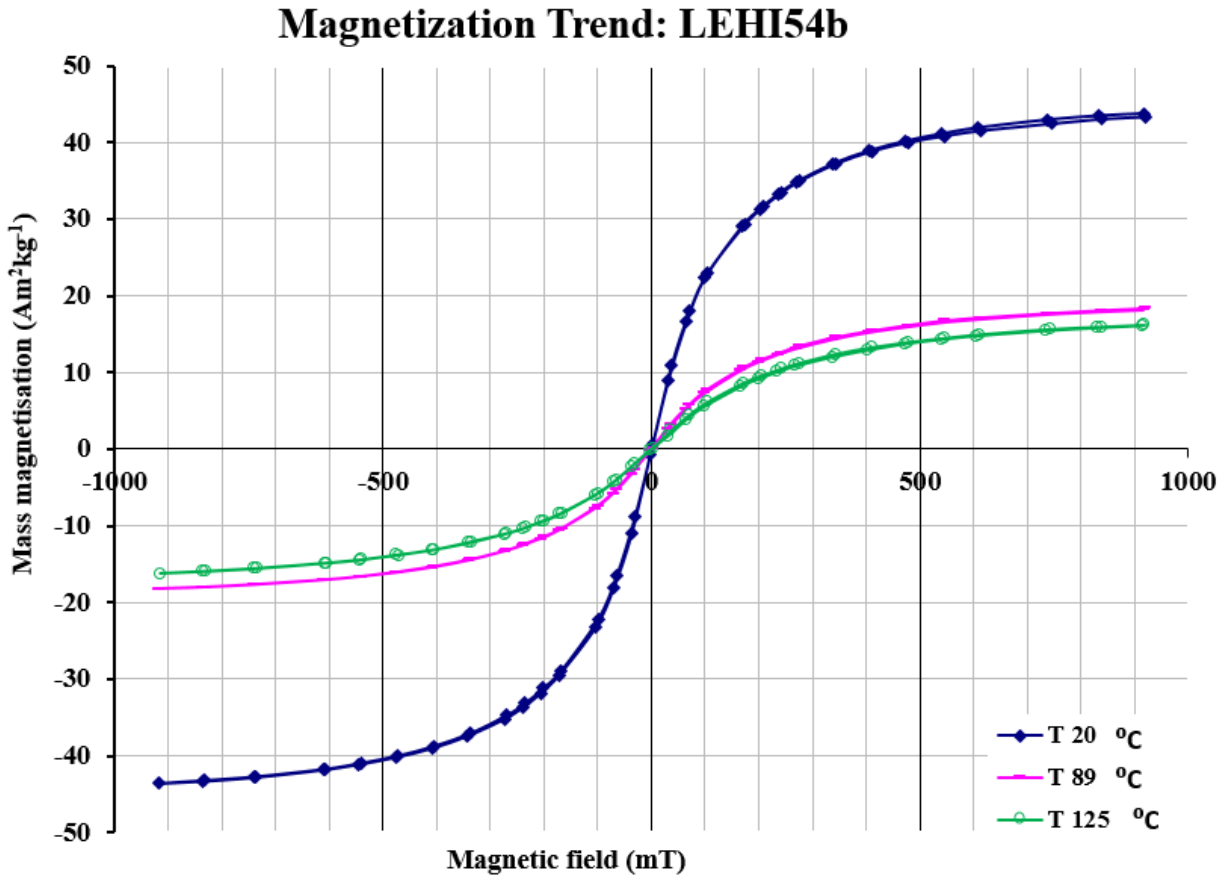

Figure 10: A variable field translation balance (VFTB) was used to measure the magnetic hysteresis loops at different temperatures (20°C, 89°C, and 125°C) blue, pink and green respectively for the LEHI 54b sample which had a Mn:Zn ratio of 0.67. Closed hysteresis loops confirm that these particles are superparamagnetic. All samples display a decrease in M_{sat} and X_{mass} at elevated temperatures.

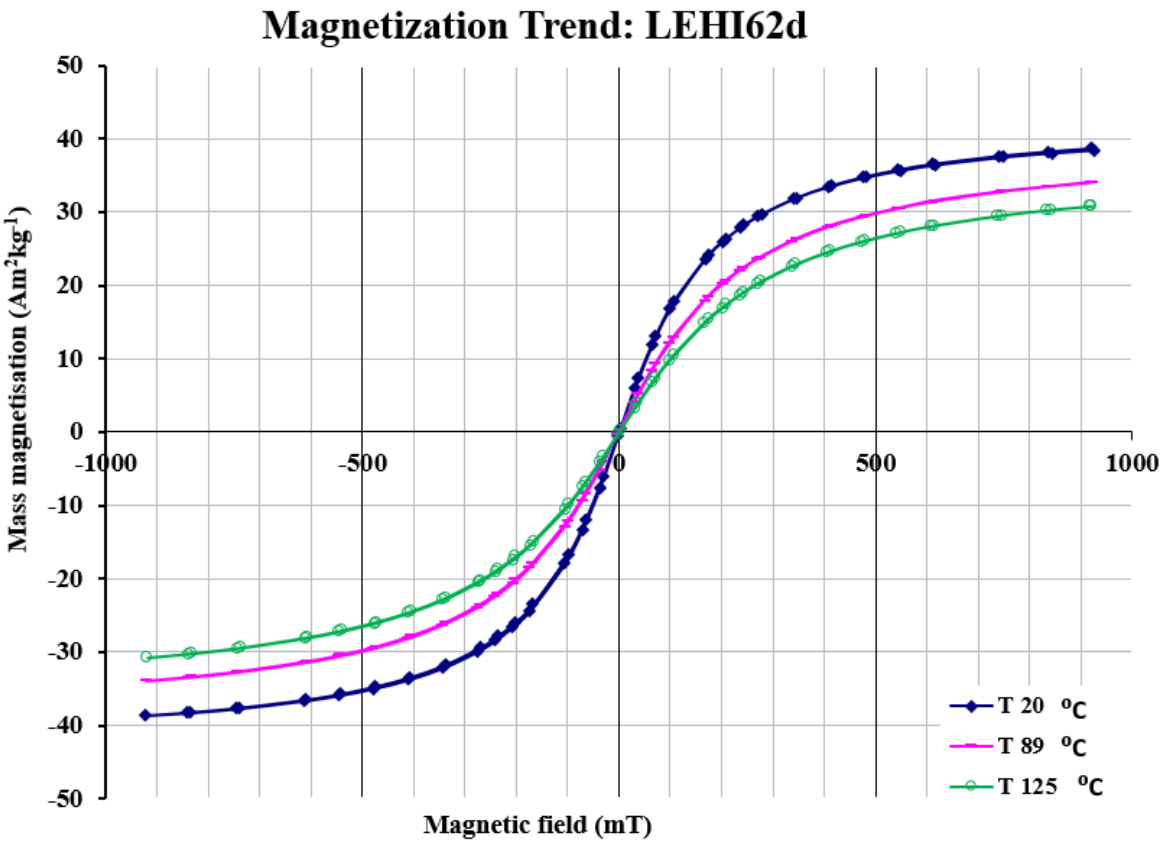

Figure 11: A variable field translation balance (VFTB) was used to measure the magnetic hysteresis loops at different temperatures (20°C, 89°C, and 125°C) blue, pink and green respectively for the LEHI 62d sample which had a Mn:Zn ratio of 2.33. Closed hysteresis loops confirm that these particles are superparamagnetic. All samples display a decrease in M_{sat} and X_{mass} at elevated temperatures.

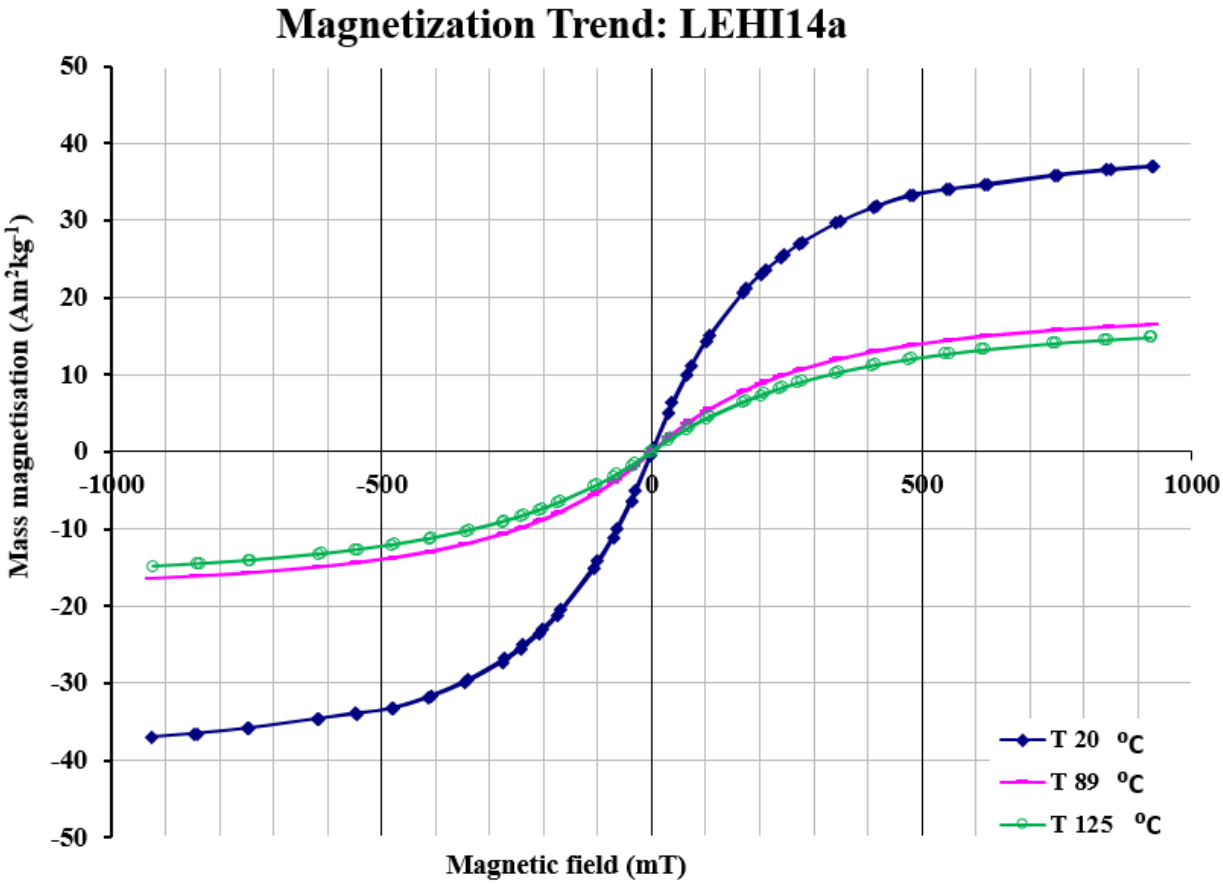

Figure 12: A variable field translation balance (VFTB) was used to measure the magnetic hysteresis loops at different temperatures (20°C, 89°C, and 125°C) blue, pink and green respectively for the LEHI 14a sample which had a Mn:Zn ratio of 1.11. Closed hysteresis loops confirm that these particles are superparamagnetic. All samples display a decrease in M_{sat} and X_{mass} at elevated temperatures.

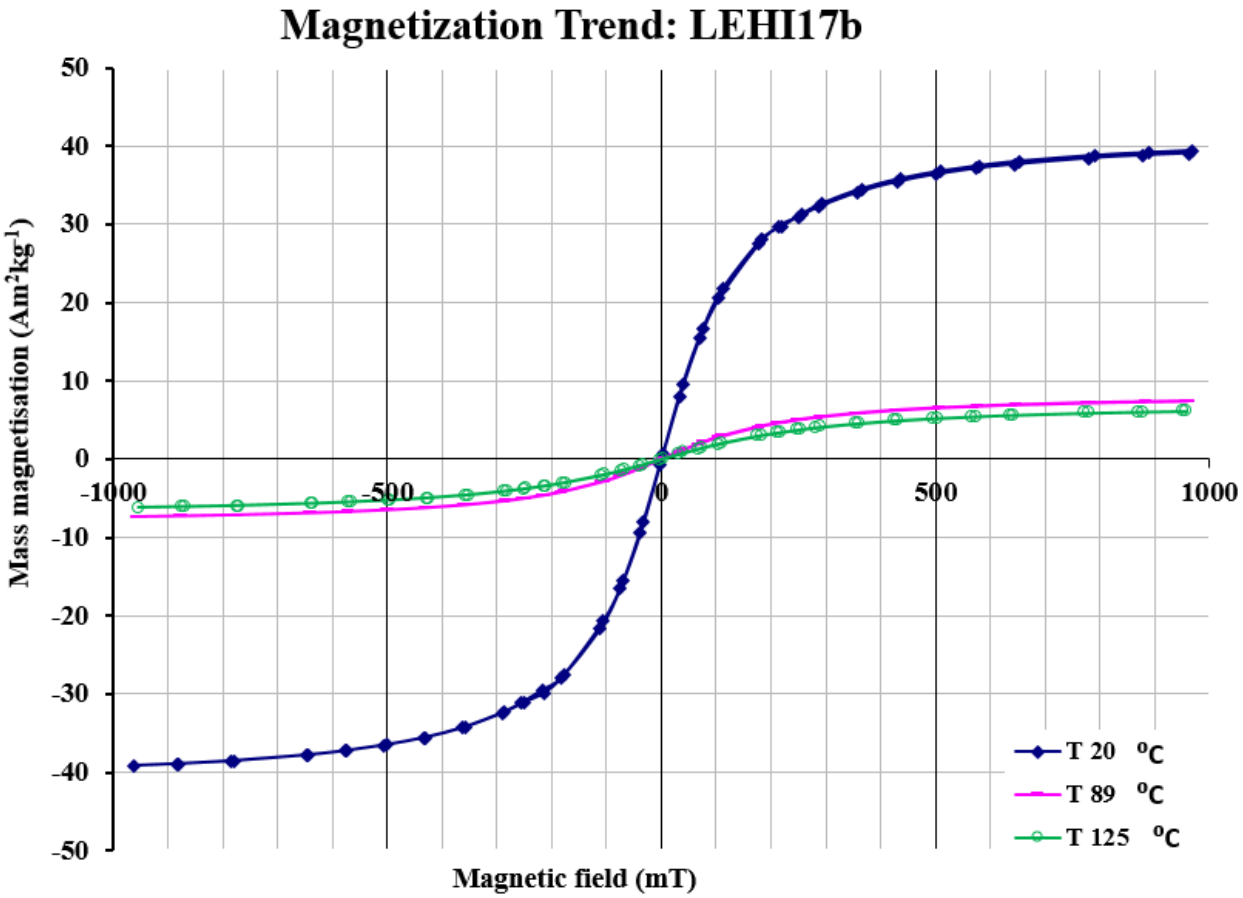

Figure 13: A variable field translation balance (VFTB) was used to measure the magnetic hysteresis loops at different temperatures (20°C, 89°C, and 125°C) blue, pink and green respectively for the LEHI 17b sample which had a Mn:Zn ratio of 0.25. Closed hysteresis loops confirm that these particles are superparamagnetic. All samples display a decrease in M_{sat} and X_{mass} at elevated temperatures.

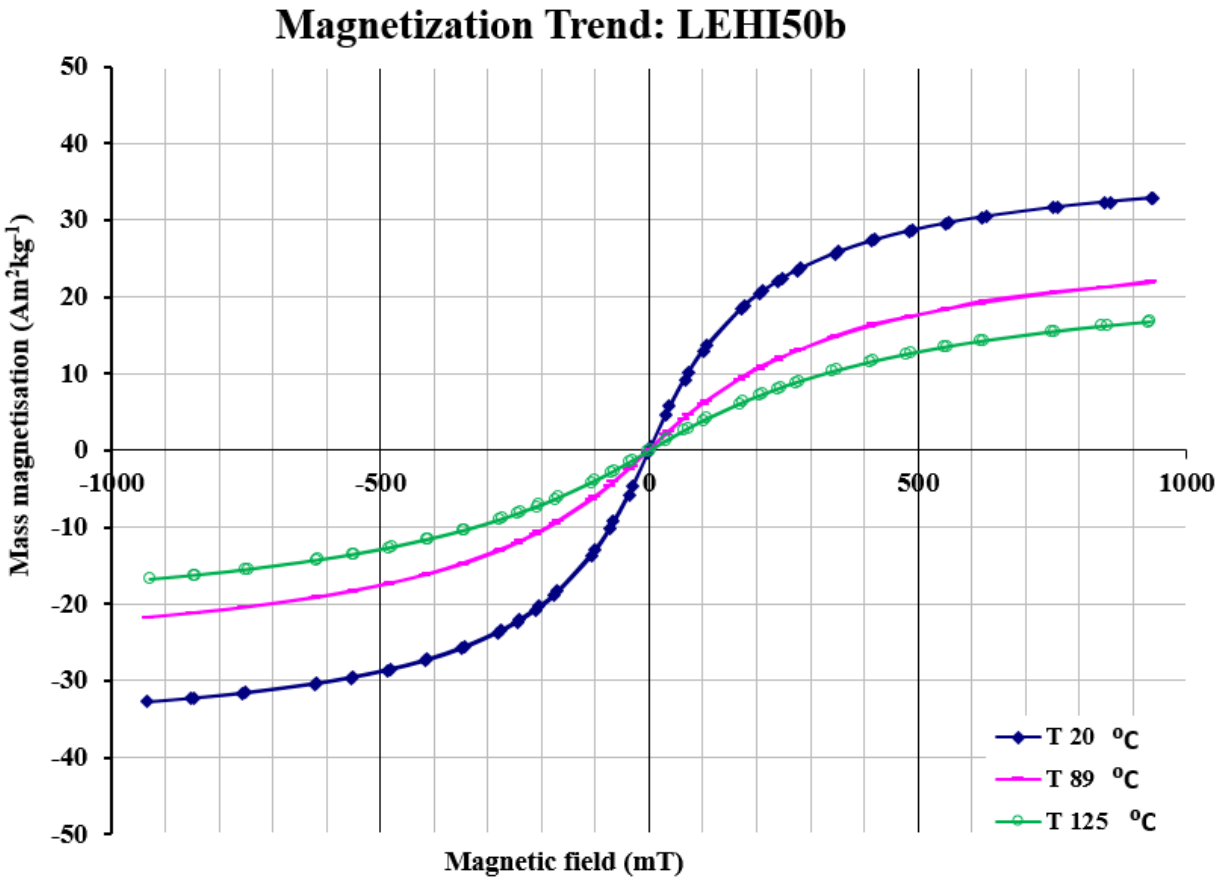

Figure 14: A variable field translation balance (VFTB) was used to measure the magnetic hysteresis loops at different temperatures (20°C, 89°C, and 125°C) blue, pink and green respectively for the LEHI 50b sample which had a Mn:Zn ratio of 1.00. Closed hysteresis loops confirm that these particles are superparamagnetic. All samples display a decrease in M_{sat} and X_{mass} at elevated temperatures.

Figure 10 through **Figure 14** illustrate the temperature dependence of the magnetic hysteresis measured in the mass magnetization of each sample. From these curves we can see that the room temperature mass saturation magnetization is relatively independent of the Mn:Zn ratio. However, it varies considerably with elevated temperature. **Figure 15** and **Figure 16** show how the mass susceptibility and saturation magnetization respectively**,** as measured on the much more accurate VFTB system, vary with the Mn:Zn ratio at elevated temperatures compared to room temperature.

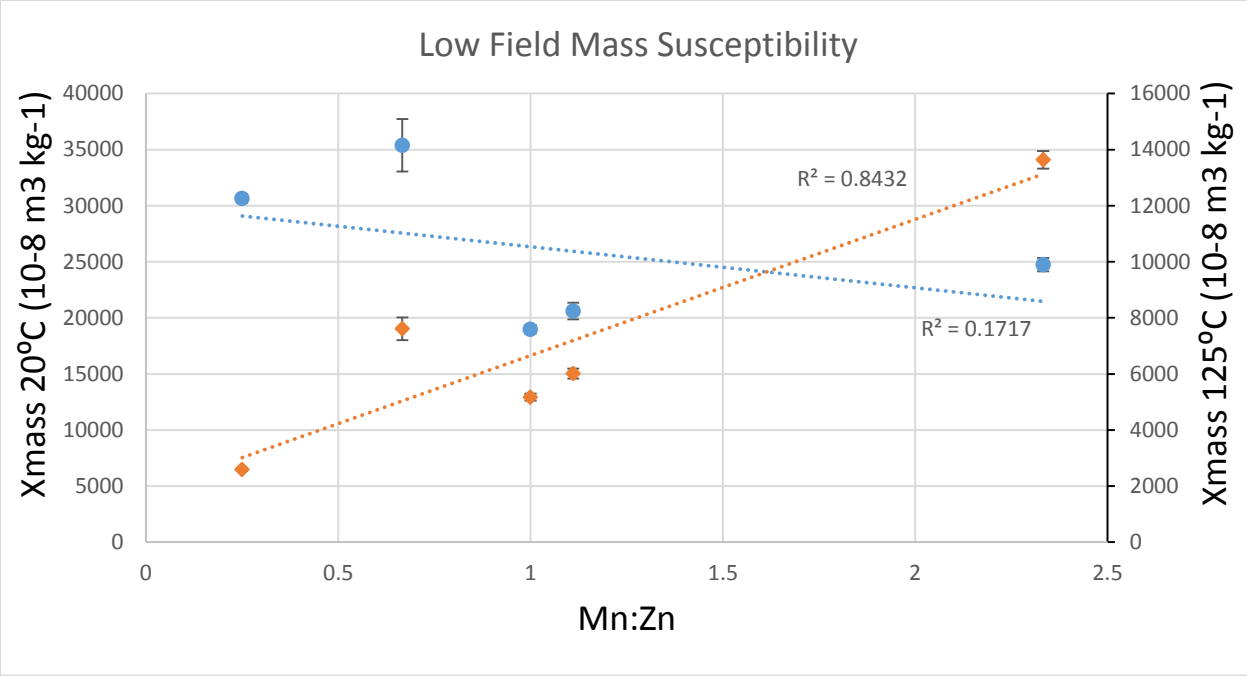

Figure 15: Mass susceptibility with Mn:Zn ratio. The room temperature measurements (left axis) were taken at 20°C (blue circles) while the elevated 'reservoir temperature' measurements (right axis) were taken at 125°C (orange diamonds). Error bars were computed as the standard deviation for multiple low field susceptibility measurements.

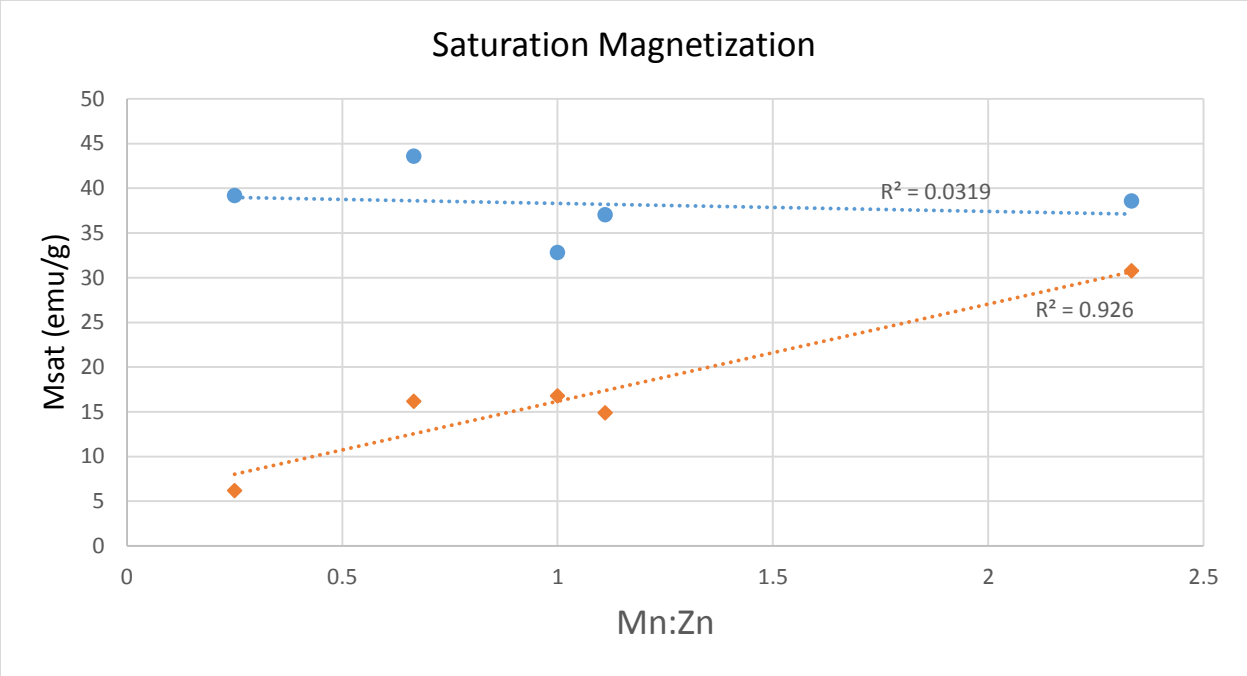

Figure 16: Saturation magnetization against Mn:Zn ratio as measured by a VFTB at both low (20°C) and high (125°C) temperatures. The Msat for elevated temperatures is noted as orange diamonds and blue circles for low temperature values. Error bars were computed as the standard deviation for multiple magnetization measurements and are smaller than data point symbols.

From **Figure 15** and **Figure 16** we can see that the low temperature (20°C) mass susceptibility or saturation magnetization is largely unrelated to the Mn:Zn content.However we can observe that sample LEHI 54b shows the highest saturation magnetization and mass susceptibility of the nanoparticles studied, this agrees with the results shown by **Figure *9***. This is not the case for elevated temperatures (125°C). At higher temperature there does appear to be a relationship between the Mn:Zn ratio and both the M_{sat} and mass susceptibility. For both susceptibility and saturation, there is a larger drop in magnitude with a higher temperature for particles with a low Mn:Zn ratio vs. those with a higher Mn:Zn ratio. This is likely related to the Curie temperature as shown later in **Figure 23**.

2.3 Curie Point Measurement

In order to characterize these particles and measure their Curie points, each sample was subjected to a range of temperatures, and their magnetic susceptibility was measured. These measurements were conducted by me at the University of Alberta with the samples exposed to the air however, oxidation was not a major concern due to their composition and the relatively low temperatures investigated. A known mass of nanoparticles was mechanically dispersed within a known mass of powdered calcium fluoride (CaF_2) inside a ceramic sample holder. The magnetic susceptibility value was first zeroed, and a background measurement with an empty ceramic holder was acquired to later account for instrumental drift. The sample holder was

then placed inside a Bartington MS2WF furnace shown in **Figure 17**. The furnace temperature was increased at a rate of 5^{o}C per minute starting from a room temperature of 21^{o}C.

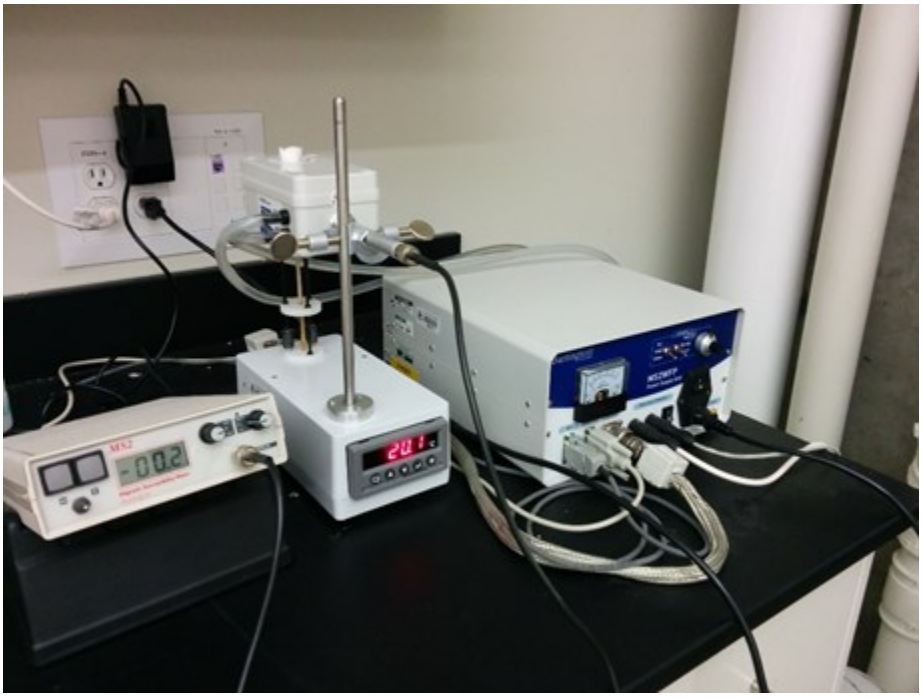

Figure 17: Bartington furnace used for temperature dependent susceptibility measurements. The sample is placed within a crucible and heated at a constant rate. The volume susceptibility is then measured at regular intervals.

Measurements of magnetic susceptibility were taken at an interval of every 5^{o}C. Due to the high resolution of the magnetic susceptibility measurements that were taken there was a short lag time between the start and finish of the measurement of 10s. This lag time was not insignificant as it was common for the temperature to increase by 1^{o}C-2^{o}C over this period. To account for this, the temperature at the beginning and end of each measurement period was recorded and the susceptibility was taken as the average over that time interval. The temperature was increased from room temperature to a maximum value where there was no further change in magnetic susceptibility at a low slightly positive value. The point after which there was no more change in magnetic susceptibility was taken as the Curie temperature. For the samples tested the maximum temperature measured was no greater than 250^{o}C and often much lower. A measurement was then recorded after cooling to room temperature and removing the sample to account for instrumental drift during the experiment.

Although these nanoparticles have a very high mass susceptibility the low concentrations used due to sample size constraints resulted in a low measured volume susceptibility. To account for this, the contribution to the magnetic susceptibility from the ceramic container and calcium fluoride could not be ignored. A sample consisting of just calcium fluoride and the ceramic container was measured at room temperature and subtracted from the measured nanoparticle

data. It is not necessary to measure the calcium fluoride sample and container at higher temperatures since these components are both diamagnetic and therefore their combined susceptibility is independent of temperature.

This corrected volume susceptibility value is noted as χ_{cor} and is measured in units of m^3/kg. The final conversion to units of mass susceptibility (χ_m) for the nanoparticles of mass m_n is:

$$\chi_m = 10\frac{\chi_{cor}}{m_n} \tag{5}$$

Figure 18 to **Figure 22** show the measured susceptibility with temperature for each of the particle compositions studied, and their respective Curie temperatures are noted in **Table 3**.

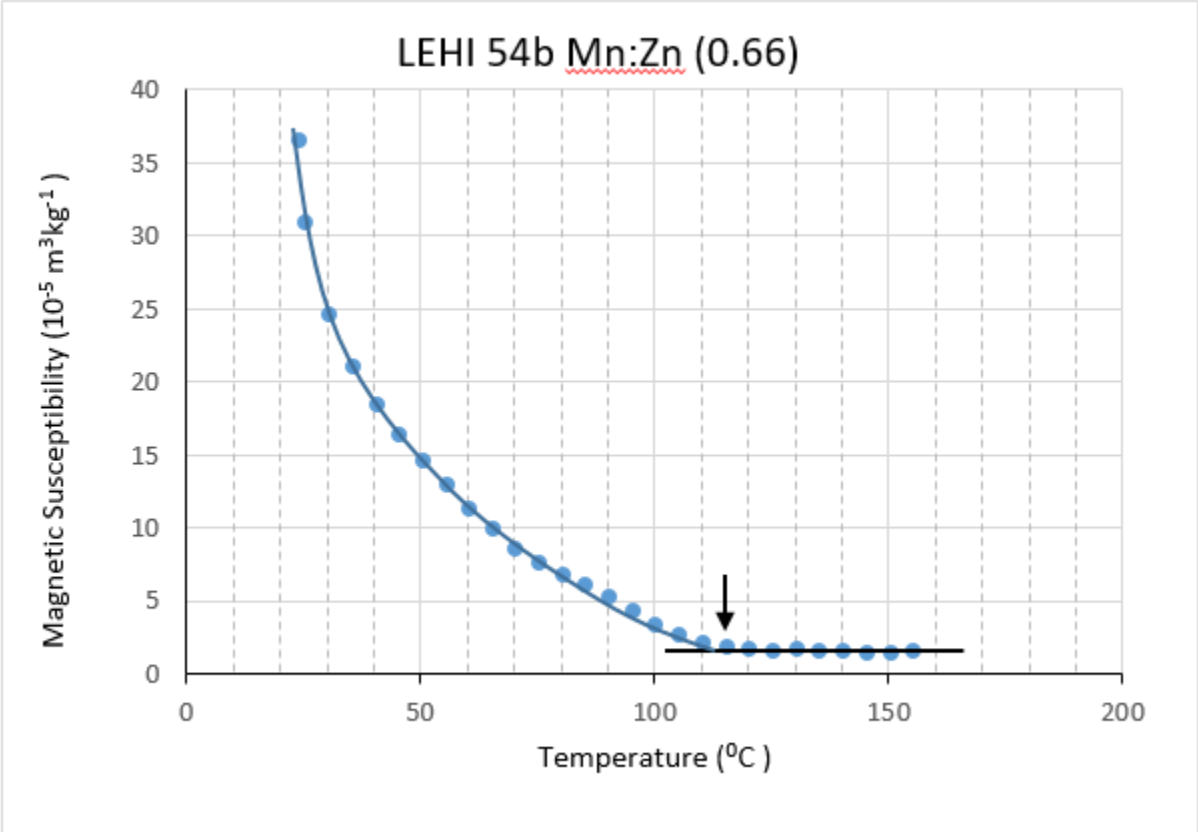

Figure 18: Curie point measurements for LEHI 54b. The sample was heated and magnetic susceptibility was measured in a Bartington furnace. Two curves were fit to the data, one nonlinear decay curve and another horizontal linear trend can be seen. The temperature where there was no further significant change in magnetic susceptibility was taken as the Curie temperature and is marked with a black arrow.

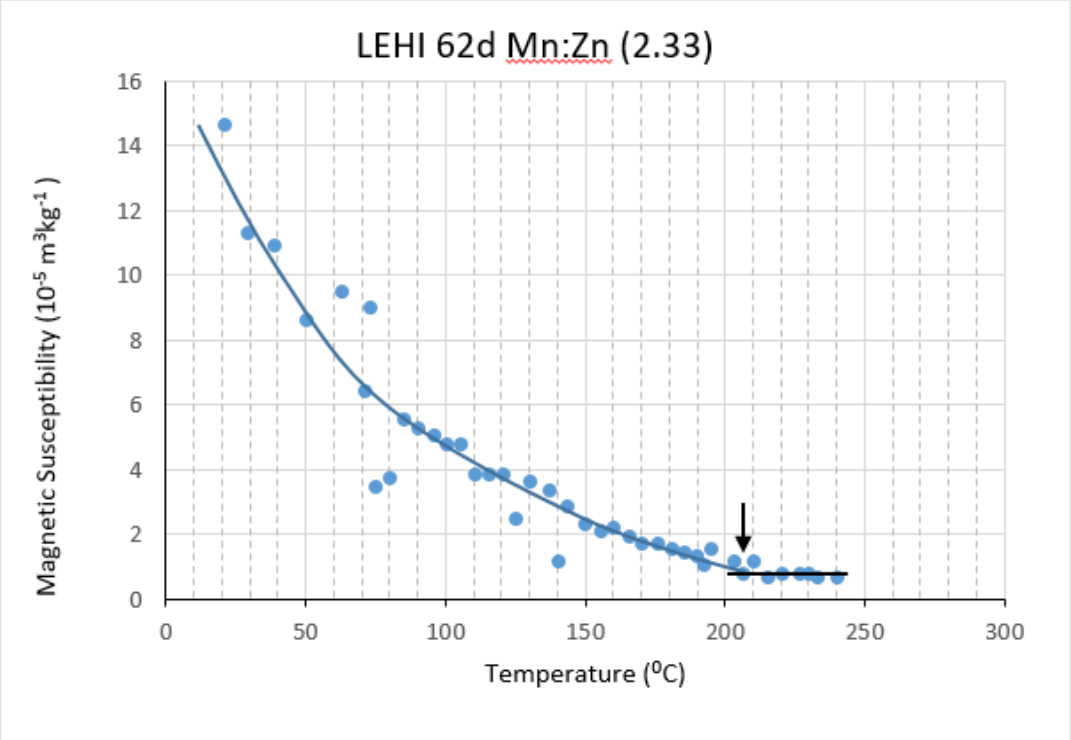

Figure 19: Curie point measurements for LEHI 62d. The sample was heated and magnetic susceptibility was measured in a Bartington furnace. Two curves were fit to the data, one nonlinear decay curve and another horizontal linear trend can be seen. The temperature where there was no further significant change in magnetic susceptibility was taken as the Curie temperature and is marked with a black arrow.

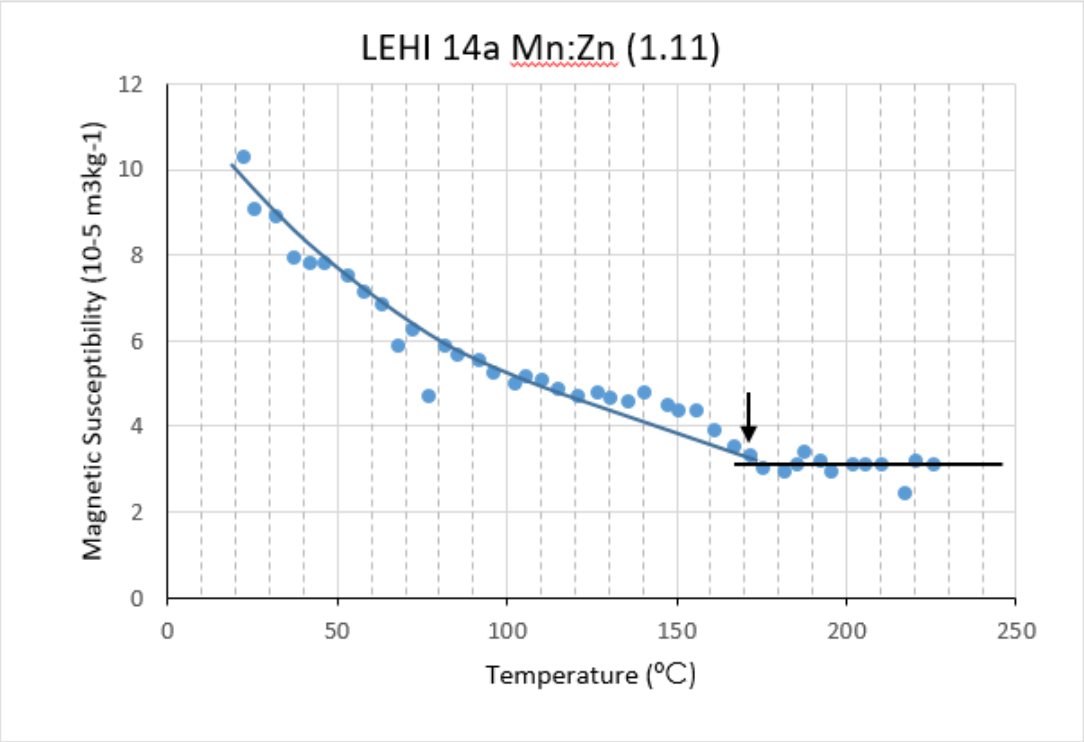

Figure 20: Curie point measurements for LEHI 14a. The sample was heated and magnetic susceptibility was measured in a Bartington furnace. Two curves were fit to the data, one nonlinear decay curve and another horizontal linear trend can be seen. The temperature where there was no further significant change in magnetic susceptibility was taken as the Curie temperature and is marked with a black arrow.

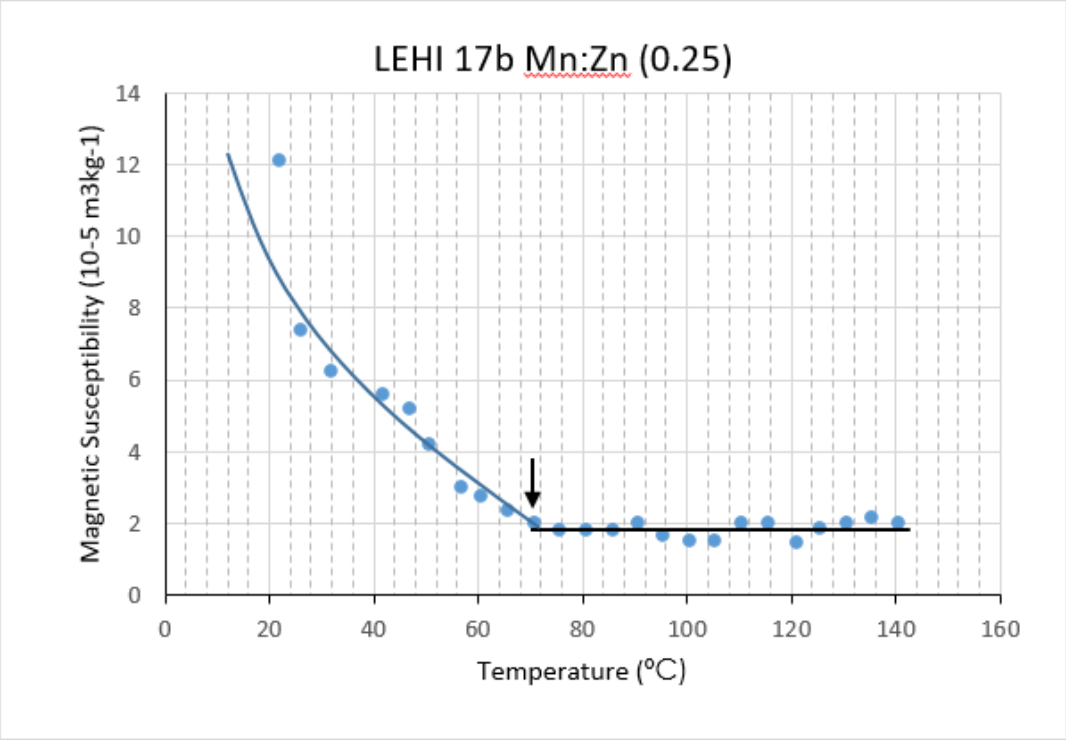

Figure 21: Curie point measurements for LEHI 17b. The sample was heated and magnetic susceptibility was measured in a Bartington furnace. Two curves were fit to the data, one nonlinear decay curve and another horizontal linear trend can be seen. The temperature where there was no further significant change in magnetic susceptibility was taken as the Curie temperature and is marked with a black arrow.

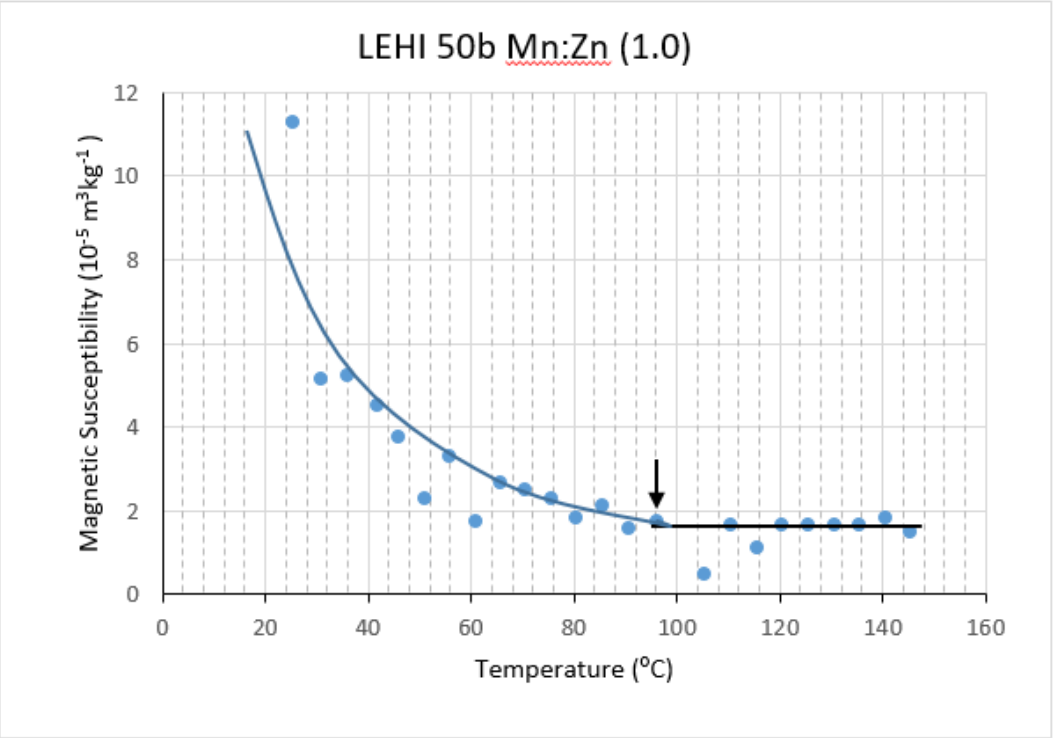

Figure 22: Curie point measurements for LEHI 50b. The sample was heated and magnetic susceptibility was measured in a Bartington furnace. Two curves were fit to the data, one nonlinear decay curve and another horizontal linear trend can be seen. The temperature where there was no further significant change in magnetic susceptibility was taken as the Curie temperature and is marked with a black arrow.

Table 3: Summary of Curie temperature results picked from the magnetic susceptibility with temperature plots. This temperature was picked at the point where there was no significant change in magnetic susceptibility with increasing temperature. The error in this measurement (δT_c) represents the range of temperatures over the 10s interval of time required to take the measurement.

Sample	*Mn*	*Zn*	*Mn:Zn*	*Curie Temperature (°C)*	*δTc (°C)*
LEHI 54b	*0.4*	*0.6*	*0.67*	*115*	*0.5*
LEHI 62a	*0.7*	*0.3*	*2.33*	*207.1*	*0.6*
LEHI 14a	*1*	*0.9*	*1.11*	*171.8*	*1.8*
LEHI 17b	*0.2*	*0.8*	*0.25*	*70.8*	*0.8*
LEHI 50b	*0.5*	*0.5*	*1.00*	*96.05*	*0.6*

The measured Curie temperatures are dependent on the amount of Zn present in the samples. **Figure 23** shows that the Curie point increases with a higher Mn:Zn ratio.

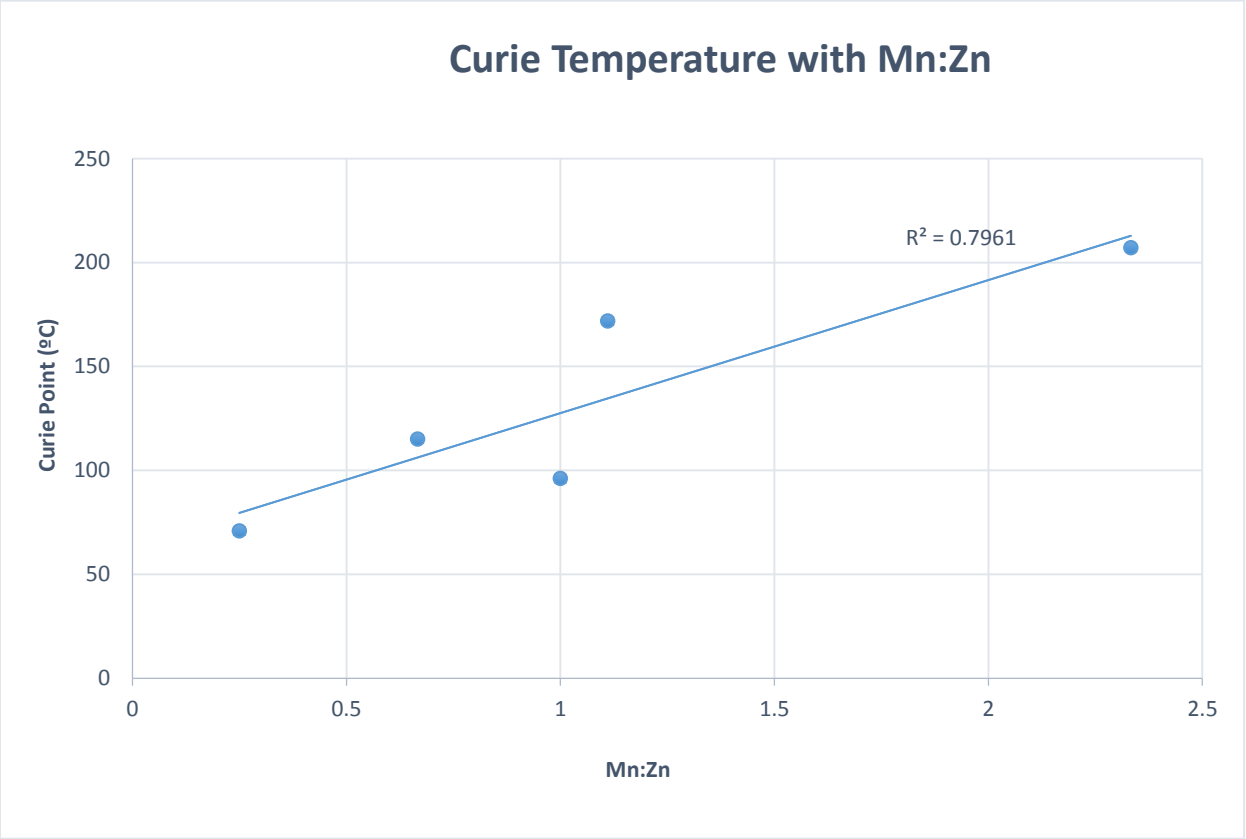

Figure 23: Curie points as a function of increasing Zn content. There is a clear linear trend where the Curie point temperature decreases as the Zn content with respect to Mn increases. Uncertainties (δT_c) are smaller than the symbols.

2.4 Relationship between Curie Temperature & Saturation Magnetization

Earlier **Figure 16** had shown the relationship between saturation magnetization (M_{sat}) and relative Mn:Zn content measured for each species of nanoparticle at both room (25^{o}C) and reservoir (125^{o}C) temperatures. From this, we can see that the Zn content does not have a significant effect on the room temperature saturation magnetization. However at higher temperatures, the Zn content does play a role in the saturation magnetization. At high temperature a low Mn:Zn ratio results in a low value of M_{sat}. It has also been shown in that the relative Zn content will influence the observed Curie temperature for a particular species of particle, shown in **Figure 23**. **Figure 24** compares the Curie points to the observed saturation magnetization. The magnetization saturation at room temperature is independent of the Curie point while at high temperature (125^{o}C) a higher Curie temperature is linearly associated with a higher saturation magnetization.

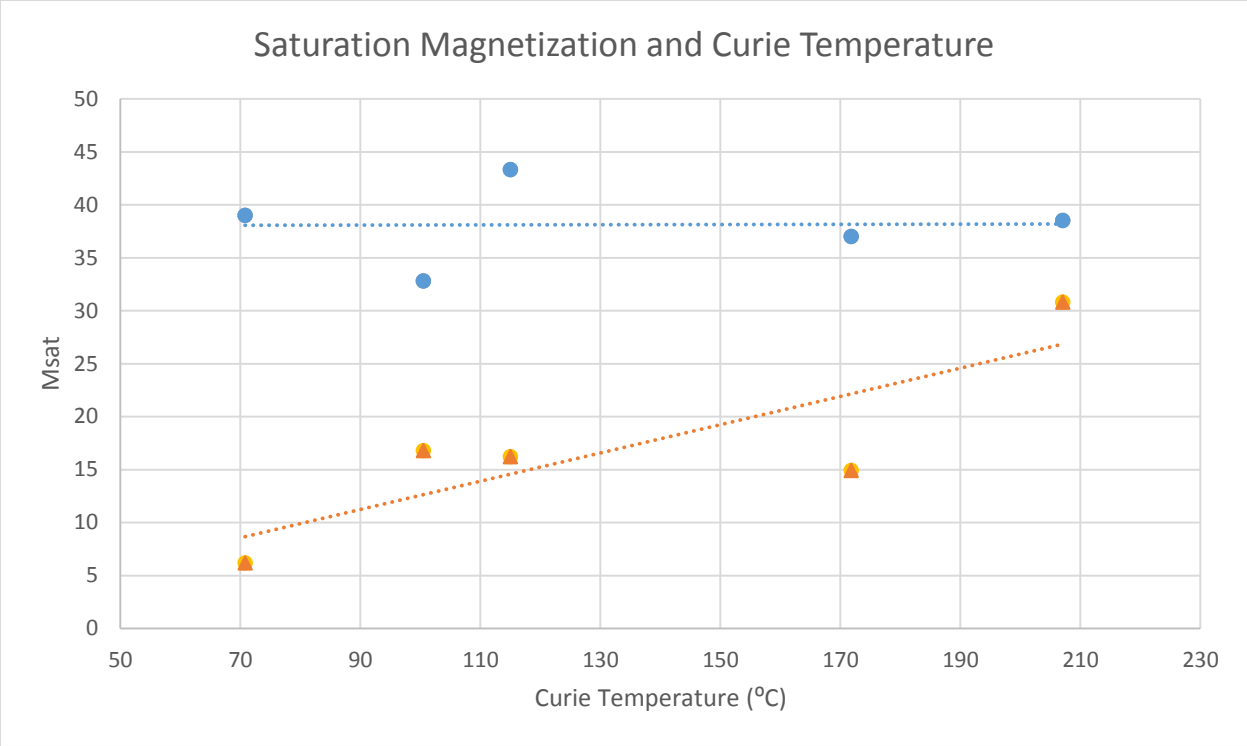

Figure 24: Saturation magnetization measured on Mn-Zn ferrite nanoparticles is compared to the Curie temperatures. At room temperature (blue circle) the M_{sat} value is independent of the Curie temperature, however, at higher temperatures (orange triangle), M_{sat} is tied to the Curie point. Error bars are smaller than symbols.

When scaling these results up to the volumes needed to properly characterize a full well fracking operation, we can see that the use of Mn:Zn ferrites provides a significant reduction in the volume of particles needed when using the same reservoir conditions as Morrow et al. (2015) as they are about 6.5x more effective than nMag as a contrast agent.

2.5 CONCLUSIONS & FUTURE WORK

In conclusion, we can see that the ratio of Mn:Zn for the Mn-Zn ferrite particles studied does, in fact, play a role in the magnetic properties of each sample. The properties measured at reservoir temperatures are greatly influenced by the relative Zn content. It was shown that the saturation magnetization at higher temperature would increase for higher ratio values of Mn:Zn or a lower fractional Zn component. This is also true for the measured Curie temperature for each sample with a higher Curie point being observed for higher values of Mn:Zn. The particles with a higher Mn:Zn ratio will have a smaller decrease in saturation magnetization observed at higher temperatures. This effect is most likely linked to the higher associated Curie temperatures of these particles. It should also be said that the species with the highest

observed magnetic susceptibility at both reservoir and room temperatures has an Mn:Zn ratio of 0.4 and is still 6.5x that of nMag when compared at reservoir temperature.

For future work, it will be necessary for more of the samples to be produced for use in the VFTB system in order to measure the magnetic hysteresis curves in more detail. Additionally, more samples comprised of different proportions of Zn and Mn should be made to further constrain the observed trend and verify that this relationship is in fact linear. Although these particles are thought to be completely oxidized in production, it is recommended as a further precaution to measure the Curie points in a vacuum or inert gas as this will reduce the potential error associated with potential high-temperature chemical changes.

Regarding the applicability towards the use as magnetic contrast agents the Mn:Zn ferrites have been shown to produce a significantly stronger magnetic susceptibility signal than the nMag previously studied by Morrow et al. (2014). This increase in magnetic susceptibility was observed for both room temperatures and downhole reservoir conditions. The room temperature response for the highest susceptibility composition was about 7.6 times that of nMag and a slightly reduced downhole response (at 125°C) of about 6.5 times that of nMag. Although this is a significant improvement over the results from nMag, large volumes of the Mn:Zn particles are still required to properly contrast against shale reservoirs. However, these results are encouraging in that Mn:Zn ferrites could act as a replacement for nMag tracers in non-shale reservoirs and provide a significant increase in the signal to noise ratio.

CHAPTER 3: ACOUSTIC ANISOTROPY

Over the past several decades our capability to make seismological observations of the earth's crust have improved dramatically due to various technological advances, which allow us to acquire, store, and process increasingly large and more detailed seismic surveys. The increased resolution of these surveys has also required us to learn more about the material properties that we are observing as the effects of anisotropy within the acoustic signal cannot be ignored when developing an appropriate geologic model. The elastic anisotropy that is inherent in most rocks will result in velocity variations which depend on the direction and polarity of seismic wave propagation. As a result of this, the intrinsic elastic properties observed within various rock types is a crucial piece of information in seismic wave modeling and interpretation. Understanding these properties and their symmetries can give valuable insights into the rock texture. This rock texture can also create an acoustic anisotropy of a significant degree with variations in travel time often exceeding 10%. Since the elastic properties themselves govern the velocity of compressional and transverse waves, any elastic anisotropy will be followed by a corresponding compressional (*p-wave*) and shear (*s-wave*) velocity anisotropy. This elastic anisotropy can be the result of many factors, all of which could influence the velocity of an elastic wave passing through the material. These can include effects from preferential mineral orientations or porosity resulting from depositional, diagenetic or metamorphic processes. For metamorphic rocks, the most commonly observed fabrics are: isotropic, transversely isotropic, and orthorhombic. These are generally the result of any lineation or foliation within a sample (or lack thereof). This then allows seismic anisotropy to be used as a tool to characterize rock fabric and texture. The causes for this anisotropic behavior can also influence other various physical properties of the rocks themselves such as electrical resistance, magnetic susceptibility, and magnetic remanence. This chapter will focus on understanding this relationship by comparing the *p* and *s-wave* velocity anisotropies previously measured within various metamorphic samples by Cholach et al. (2005), as well as new measurements on the same samples, to understand the proper context for the magnetic measurements discussed in the next chapter.

3.1 ELASTIC WAVE ANISOTROPY

Markham (1957) was one of the first to determine elastic constants through the pulse transmission method by measuring the transmission time of a simple acoustic pulse through known thicknesses of material. This was obtained to determine the velocity anisotropy of various metals of cubic and hexagonal crystalline structure. In these earlier anisotropic studies simple mineral structures were investigated due to easier experimental design and elastic parameter calculation. These earliest geometries were usually cubic or hexagonal in nature due to the many degrees of symmetry.

Later the pulse transmission technique was applied to shale samples at various angles to the axis of symmetry by Johnston and Christensen (1995), which showed both shear wave splitting

and allowed for the phase velocity of the waves to be measured. These phase velocities were then used to determine the elastic properties of the shale sample and further quantify the anisotropic behavior of these rocks. Metamorphic rocks can be particularly complicated in terms of their elastic anisotropy due to the superposition of depositional, mineralogical and deformational processes that combine to create a complex rock fabric. The main purpose of this chapter is to review and supplement (with new measurements) the previous observations made by Cholach et al. (2005) wherein the elasticity of metamorphic rocks within the Annabel Lake ductile shear zone of the Flin Flon belt in the Trans-Hudson Orogen were studied. The previous and new work utilized extensive ultrasonic measurements including atmospheric and high-pressure laboratory conditions to characterize the elastic anisotropy for various samples taken from within the shear zone. Understanding the elastic behavior of these rocks is of particular interest for this thesis since this will allow us to draw comparisons between the elastic anisotropy observed for a subset of these samples and the magnetic fabric of the same rocks that will be measured in **Chapter 4**.

3.1.1 Causes of Velocity Anisotropy

There are several proposed mechanisms to explain the source of elastic anisotropy observed in rocks. Shales are a common example. The most common explanation is the preferential alignment of the plate-like clay minerals (Hornby et al., 1994; Sayers, 1994, 2005; Cholach, 2005). One other explanation relies on the preferential orientation of microscopic fractures or planar pores that are parallel to the plane of bedding as was demonstrated by He (2006) and Martinez (2014). Finally, kerogen found within shales may also form fine layering within the shale that would contribute towards vertical transversely isotropic (VTI) behavior that was described by several authors (Backus, 1962; Meissner, 1984; Vernik and Liu, 1997).

Preferential alignment seen in clay minerals is a large contributing factor to the overall anisotropy observed in shales as they are the primary mineralogical components within a shale. Clay minerals themselves are highly anisotropic and are primarily plate-like in structure (Sayers, 1994, 2005), and their observed anisotropy is due to a preferred alignment within the overall assemblage. If clay minerals are uniformly dispersed into a randomly oriented conglomerate, they will result in an isotropic material (Wang et al., 2001; Cholach, 2005). However, depositional and diagenetic processes will often result in a preferred parallel orientation of these minerals within the bedding plane or horizontal (Vernik and Liu, 1997).

Laboratory experiments performed on shale samples further support clay minerals as a source of transverse isotropy. Sondergeld and Rai (1992) have shown that the observed mineral fabric formed by the alignment of clay minerals in shale matches the observed elastic anisotropy fabric. This conclusion is further supported by Johnston and Christensen (1995) as a strong correlation between the clay mineral orientations observed with X-ray diffraction and seismic anisotropy was found. The closure of microfractures with pressure was attributed to some decrease in seismic anisotropy, however clay minerals were found to be the primary control, especially at high pressure. From this, we see that other factors besides clay content and

orientation can influence seismic anisotropy such as the presence of microfractures or oriented porosity.

Microfractures and preferentially oriented porosity within rocks are another source of seismic anisotropy. These microfractures can be the result of various processes such as pressure relief due to erosion, crustal stress fields, or drilling induced processes. Various workers have observed a decrease in seismic anisotropy with increased pressure (Johnston, 1987; Johnston and Christensen, 1995; Vernik and Liu, 1997; Martinez, 2014). This decrease in anisotropy is substantial, up to 29% (Vernik and Nur, 1992) or even 50% (Johnston and Christensen, 1995) in some cases. Particularly, this is can be seen in experimental results as a sharp velocity increase with confining pressure at low confining pressures, which then tapers off to a shallower increase at higher pressures (He, 2006). On its own, the change in seismic velocity with pressure could be attributed to the change in pore shape with pressure as well as the closure of the microfractures. However, the contribution of the microfractures is evidenced by a hysteresis in the velocity vs. pressure graphs. This hysteresis is due to the microfractures, which remain closed until a pressure which is lower than the pressure where they were initially closed (Jones and Wang, 1981). From this we can see that there are three main sources of seismic anisotropy within rocks: any layering of rock units or bedding, any network of oriented cracks or fractures within the rock and any preferred orientation of minerals within the rock samples.

3.1.2 Elastic Anisotropy Review

The study of elastic properties and their anisotropies within samples can give a large amount of information about the rock and mineral structure. The relationship between the elastic constants for a sample and the observed elastic anisotropy will be described in this chapter. An in-depth derivation for these relationships can be found in Nye (1957), whereas the following sections will only act as a brief summary. In its most general form the relationship between stress and strain can be shown by Hooke's law which is written as:

$$\sigma_{ij} = c_{ijkl}\varepsilon_{kl} \tag{6}$$

In the Einstein summation notation, σ_{ij} shows the second order stress tensor, which is defined as the unit force per unit area. Similarly, ε_{kl} shows the second order strain tensor (Nye, 1957), which represents the deformation experienced due to the stress that is applied.

$$\varepsilon_{kl} = \frac{1}{2}\left(\frac{\partial u_k}{\partial x_l} + \frac{\partial u_l}{\partial x_k}\right) \tag{7}$$

The parameter u is the displacement along an axis. The elasticity tensor c_{ijkl} is a fourth order tensor containing the elastic stiffness constants. The elasticity tensor c contains 81 elements, however symmetry can be used to reduce the number of independent elements from 81 down to 36. This then reduces down to 21 independent elements as the material may only gain energy during compression (Nye, 1957). Specifically, this symmetry is of the form:

$$c_{ijkl} = c_{jikl} = c_{ijlk} = c_{jilk} \tag{8}$$

It can be shown that due to the conservation of energy (Hudson and Harrison, 2000):

$$c_{ijkl} = c_{klij} \tag{9}$$

With this symmetry in mind, the tensor c_{ijkl} is more commonly seen in literature as the second order stiffness tensor C_{mn} which is shown as:

$$c_{ijkl} = C_{mn}(m, n = 1{:}\,6; i, j, k, l = 1{:}\,3) \tag{10}$$

This new tensor C_{mn} is a second order symmetric Voigt matrix. This new index can be extended to the rest of the equation for Hooke's law by making the substitution of (Nye, 1957; Musgrave, 1970):

$$m = \begin{cases} i, & i = j \\ 9 - (i + j) & i \neq j \end{cases} \tag{11}$$

$$n = \begin{cases} k, & k = l \\ 9 - (k + l) & k \neq l \end{cases} \tag{12}$$

This simplifies Hooke's law into the following form:

$$\sigma_m = C_{mn}\varepsilon_n \tag{13}$$

This new notation causes σ_m and ε_n to become 6 X 1 vectors containing the six independent components of the stress and strain tensors respectively. C_{mn} is now a 6 X 6-second-order tensor containing the 21 independent stiffness components from c_{ijkl} and can be seen as:

$$\begin{pmatrix} \sigma_1 \\ \sigma_2 \\ \sigma_3 \\ \sigma_4 \\ \sigma_5 \\ \sigma_6 \end{pmatrix} = \begin{pmatrix} C_{11} & C_{12} & C_{13} & C_{14} & C_{15} & C_{16} \\ C_{21} & C_{22} & C_{23} & C_{24} & C_{25} & C_{26} \\ C_{31} & C_{32} & C_{33} & C_{34} & C_{35} & C_{36} \\ C_{41} & C_{43} & C_{43} & C_{44} & C_{45} & C_{46} \\ C_{51} & C_{52} & C_{53} & C_{54} & C_{55} & C_{56} \\ C_{61} & C_{62} & C_{63} & C_{64} & C_{65} & C_{66} \end{pmatrix} \begin{pmatrix} \varepsilon_1 \\ \varepsilon_2 \\ \varepsilon_3 \\ \varepsilon_4 \\ \varepsilon_5 \\ \varepsilon_6 \end{pmatrix} \tag{14}$$

In this expanded form 21 elements of the stiffness matrix are independent, so, therefore, there is no symmetry also known as triclinic. There are other forms of this stiffness matrix C_{mn} that can reflect different forms of symmetry.

3.1.3 Classes of Symmetry

There are various classifications for the types of mineral elastic symmetries (Nye, 1957). All materials studied will exhibit a trivial symmetry of 180^{o} about the origin such that every element C_{mn} will be equal to its counterpart C_{nm}. It should be noted that in this work the letters chosen to represent matrix elements (a, b, c, …, v) are not necessarily equal between anisotropy classes. They only serve to identify patterns in the individual stiffness matrix element values.

Isotropic. An isotropic material is one where the observed symmetry is spherical. That is to say that the properties observed are the same in all directions. In the case of elasticity, there are only two independent elastic parameters. Given below is the form of the stiffness matrix of an isotropic material:

$$C = \begin{pmatrix} a & b & b & 0 & 0 & 0 \\ b & a & b & 0 & 0 & 0 \\ b & b & a & 0 & 0 & 0 \\ 0 & 0 & 0 & c & 0 & 0 \\ 0 & 0 & 0 & 0 & c & 0 \\ 0 & 0 & 0 & 0 & 0 & c \end{pmatrix} \tag{15}$$

The parameters a, b and c are all dependant on two independent components: Young's modulus μ and the Poisson ratio λ with this relationship being shown as:

$$\begin{gathered} a = \lambda + 2\mu \\ b = \lambda \\ c = \mu \end{gathered} \tag{16}$$

The Poisson ratio λ can be rewritten in terms of the bulk modulus K and shear modulus μ:

$$\lambda = K - \frac{2}{3}\mu \tag{17}$$

Cubic. Materials with a cubic symmetry are elastically anisotropic (Helbig, 1994), while some such as halite may remain optically isotropic with three independent stiffness coefficients a, b

and c shown below. A cubic system is characterized as having all three basis vectors being orthogonal and sharing a common magnitude.

$$C = \begin{pmatrix} a & b & b & 0 & 0 & 0 \\ b & a & b & 0 & 0 & 0 \\ b & b & a & 0 & 0 & 0 \\ 0 & 0 & 0 & c & 0 & 0 \\ 0 & 0 & 0 & 0 & c & 0 \\ 0 & 0 & 0 & 0 & 0 & c \end{pmatrix} \tag{18}$$

$$c = \frac{a-b}{2} \tag{19}$$

Hexagonal. For a material to be hexagonally symmetric, it is required that there are five independent stiffness coefficients a, b, c, d, and e.

$$C = \begin{pmatrix} a & b & c & 0 & 0 & 0 \\ b & a & c & 0 & 0 & 0 \\ c & c & d & 0 & 0 & 0 \\ 0 & 0 & 0 & e & 0 & 0 \\ 0 & 0 & 0 & 0 & e & 0 \\ 0 & 0 & 0 & 0 & 0 & f \end{pmatrix} \tag{20}$$

The last coefficient f is a combination of the elements a and b such that:

$$f = \frac{a-b}{2} \tag{21}$$

Orthorhombic symmetry is characterized by nine independent elastic constants, which results in three orthogonal planes of symmetry. Orthorhombic lattices take the form of a rectangular prism with each orthogonal basis vector having a unique magnitude.

$$C = \begin{pmatrix} a & b & c & 0 & 0 & 0 \\ b & d & e & 0 & 0 & 0 \\ c & e & f & 0 & 0 & 0 \\ 0 & 0 & 0 & g & 0 & 0 \\ 0 & 0 & 0 & 0 & h & 0 \\ 0 & 0 & 0 & 0 & 0 & i \end{pmatrix} \tag{22}$$

Monoclinic symmetry has a system of 13 independent elastic coefficients with the form:

$$C = \begin{pmatrix} a & b & c & 0 & 0 & j \\ b & d & e & 0 & 0 & k \\ c & e & f & 0 & 0 & l \\ 0 & 0 & 0 & g & m & 0 \\ 0 & 0 & 0 & m & h & 0 \\ j & k & l & 0 & 0 & i \end{pmatrix} \quad (23)$$

Monoclinic crystals form when the three basis vectors are of different magnitude and only two of them are orthogonal to one another, and the third vector is not orthogonal.

Triclinic materials exhibit the least symmetric form of elastic anisotropy. They are similar to orthorhombic materials in that they have three basis vectors of unequal length. However, in addition to this inequality in magnitude, none of these basis vectors are orthogonal to each other. The elastic stiffness tensor for triclinic materials takes the form of:

$$C = \begin{pmatrix} a & b & c & j & k & l \\ b & d & e & m & n & v \\ c & e & f & p & q & r \\ j & m & p & g & s & t \\ k & n & q & s & h & u \\ l & v & r & t & u & i \end{pmatrix} \quad (24)$$

3.1.4 Properties of Transversely Isotropic Materials

In this section, we will discuss one of the special cases of elastic symmetry and address how to calculate the stiffness coefficients from the observed seismic velocities. There are several types of rock samples studied in this work ranging from metasediments to metavolcanics which were determined by Cholach et al. (2005) to be largely transversely isotropic or orthorhombic in symmetry. As mentioned earlier in section 4.2.1 these rocks are mechanically anisotropic. This anisotropy is associated with depositional and diagenetic processes which result in a preferred mineral alignment, microcrack and pore orientation resulting in the observed foliation seen within the sample. Transversely isotropic (Sayers, 1994, 2005) materials have properties which are symmetric about one axis normal to the plane of isotropy. These materials are described by a stiffness matrix that shares a similar form to hexagonal symmetry however they have a more specific relationship between the elastic constants shown as:

$$C = \begin{pmatrix} a & a-2f & c & 0 & 0 & 0 \\ a-2f & a & c & 0 & 0 & 0 \\ c & c & d & 0 & 0 & 0 \\ 0 & 0 & 0 & e & 0 & 0 \\ 0 & 0 & 0 & 0 & e & 0 \\ 0 & 0 & 0 & 0 & 0 & f \end{pmatrix} = \begin{pmatrix} C_{11} & C_{12} & C_{13} & 0 & 0 & 0 \\ C_{21} & C_{22} & C_{23} & 0 & 0 & 0 \\ C_{31} & C_{32} & C_{33} & 0 & 0 & 0 \\ 0 & 0 & 0 & C_{44} & 0 & 0 \\ 0 & 0 & 0 & 0 & C_{55} & 0 \\ 0 & 0 & 0 & 0 & 0 & C_{66} \end{pmatrix} \quad (25)$$

It is not possible to directly measure elastic moduli, as such they must be determined through static stress-strain measurements or by measuring the seismic velocities that are taken along the appropriate directions. For the case of VTI media there are 5 independent stiffness coefficients which can be calculated, and the directions of measurement are defined and illustrated in **Figure 25**.

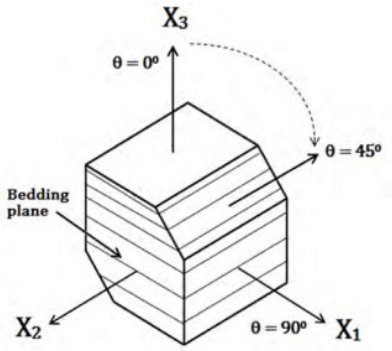

Figure 25: Schematic of ample geometry used to characterize a VTI rock with a rotational symmetry axis parallel to X_3. The angle of propagation is measured from X_3 towards the X_1-X_2 plane with the oblique measurement taken at 45° (Martínez and Schmitt, 2016).

3.1.5 Elastic Stiffness and Seismic Velocities

There are several methods to determine the elastic moduli indirectly as it is not possible to directly measure them. There are two common approaches for this measurement. The first being the use of seismic wave velocity anisotropy, and the second being the use of static stress-strain measurements. This section will serve to connect observed seismic velocities to the corresponding elastic moduli.

In the case of transverse isotropy, the phase velocity and wavefront or group velocity are the same along the principle axes of symmetry. This is not the case for intermediate angles, and further work is required to determine the phase velocity. A full derivation can be found in various publications (Daley and Hron, 1977; Thomsen, 1986), however from this we can see that for vertically transversely isotropic materials the different velocities as a function of angle θ are:

$$v_p(\theta) = \sqrt{\frac{asin^2(\theta) + dcos^2(\theta) + e + \sqrt{M}}{2\rho}} \tag{26}$$

$$v_{sv}(\theta) = \sqrt{\frac{asin^2(\theta) + dcos^2(\theta) + e - \sqrt{M}}{2\rho}} \tag{27}$$

$$v_{sh}(\theta) = \sqrt{\frac{fsin^2(\theta) + ecos^2(\theta)}{\rho}} \tag{28}$$

where the subscripts p, sh and sv indicate the compressional, horizontal shear polarity and vertical shear polarity waves respectively and:

$$M = \big((a-e)sin^2(\theta) - (d-e)cos^2(\theta)\big)^2 + (c+e)^2 sin^2(2\theta) \tag{29}$$

From the previous equations we can then find values for the elastic constants if we chose appropriate values for θ (Auld, 1974):

$$\begin{gathered} a = \rho {v_{p90}}^2 \\ d = \rho {v_{p0}}^2 \\ e = \rho {v_{s0}}^2 \\ f = \rho {v_{sh0}}^2 \\ c = \sqrt{\frac{\big(4\rho {v_{p45}}^2 - a - d - 2e\big)^2 - (a-d)^2}{4}} - e \end{gathered} \tag{30}$$

The value for the stiffness coefficient c can also be approximated by using a combination of v_{p45} and v_{sv45} (Hemsing, 2007). This has the benefit over the value of c shown above in that it will require fewer terms to calculate, and therefore has a lower propagated value of uncertainty.

$$c = \sqrt{\frac{4\rho^2\left({v_{p45}}^2 - {v_{sv45}}^2\right)^2 - (a-d)^2}{4}} - e \tag{31}$$

These equations allow us to determine, under the assumption of a transversely isotropic material with an alignment shown in **Figure** 25, the elastic constants from the recorded waveforms and their associated phase velocities.

It is important to remember that these values for the elastic constants are dependent on the material being transversely isotropic and that the vertical axis, in this case, is aligned along the axis of rotational symmetry as shown in **Figure** 25. As stated earlier it is important to use the phase velocity of the signal and not the group velocity as these two values can differ for anisotropic media as is shown in **Figure 26** below modified from Kebaili and Schmitt (1997). In this figure, the planar wave W' (traveling at a phase velocity v) is indistinguishable from the wavefront W (traveling at a group velocity of V) for an observer at point P. This makes it impossible to differentiate between the different travel path lengths of L and L' or their respective angles of propagation. This discrepancy must be accounted for to avoid measuring the group velocity in the laboratory instead of the phase velocity.

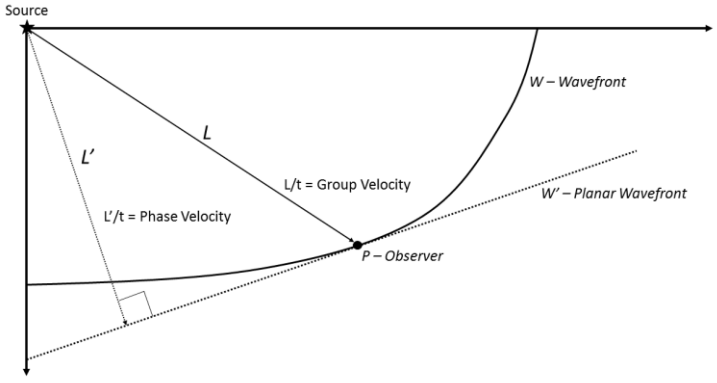

Figure 26: Schematic of a wavefront propagation through an anisotropic material.

For the different principle symmetry directions (i.e., directions parallel (θ = 90^o) or perpendicular (θ = 0^o) to the plane of symmetry) the above equations are appropriate, as the phase and group velocities are the same. This is not the case for oblique angles, and additional care must be taken to use an appropriate transducer configuration to uniquely determine the phase velocity (Cholach, 2005; Martinez, 2014).

However, the samples examined in Cholach et al. (2005) were not cut according to the geometry shown in **Figure 25** but rather as core plugs along mutually orthogonal directions which are illustrated by **Figure 27**. This limited the number of elastic constants that were derived in the previous study, and it is not possible to determine the independent off-diagonal elements. However, it is still possible to make some observations about the type and degree of

symmetry observed within each sample. The following details the methodology used in Cholach et al. (2005) to determine the elastic coefficients for the various metamorphic rock samples. For example, within an isotropic material the X, Y and Z axes are all arbitrary as the velocities are independent of the direction of propagation. In this case, the compressional wave velocities are equal such that:

$$v_{px} = v_{py} = v_{pz} \tag{32}$$

Similarly for shear waves:

$$v_{sxy} = v_{syx} = v_{sxz} = v_{szx} = v_{szy} = v_{syz}$$

which, when combined with the density ρ, allows us to calculate the elastic constants a, b and c for an isotropic material as:

$$a = \rho {v_{px}}^2 \tag{34}$$

$$b = \rho\left({v_{px}}^2 - {v_{sxy}}^2\right) \tag{35}$$

$$c = \rho {v_{sxy}}^2 \tag{36}$$

We can use a similar method to examine transversely isotropic materials where the Z direction is specified as the axis of symmetry making X and Y arbitrary resulting in the *p-wave* velocities as:

$$v_{px} = v_{py} \neq v_{pz} \tag{37}$$

The shear wave velocities are:

$$v_{syz} = v_{sxz} \neq v_{syx} = v_{sxy} = v_{szy} = v_{szx} \tag{38}$$

However only measuring along the axes of symmetry limits the number of elastic coefficients that we can determine for a hexagonal geometry to:

$$a = \rho {v_{px}}^2$$

$$b = a - 2f$$

$$d = \rho {v_{pz}}^2$$
$$e = \rho {v_{sxz}}^2 \quad (39)$$
$$f = \rho {v_{sxy}}^2$$

with the c hexagonal coefficient from not being resolvable through these measurements.

For orthorhombic materials, it is possible to determine only six of the nine elastic constants by measuring only along the axes of symmetry. For orthorhombic materials, we can expect the *p-wave* velocities to be independent of each other such that:

$$v_{px} \neq v_{py} \neq v_{pz} \quad (40)$$

with the shear wave velocities as:

$$v_{syz} = v_{szy} \neq v_{syx} = v_{sxy} \neq v_{sxz} = v_{szx} \quad (41)$$

This does not allow for the off-diagonal elements to be determined however it is possible to calculate the diagonal elastic coefficients as:

$$a = \rho {v_{px}}^2$$
$$d = \rho {v_{py}}^2$$
$$f = \rho {v_{pz}}^2 \quad (42)$$
$$g = \rho {v_{syz}}^2$$
$$h = \rho {v_{sxz}}^2$$
$$i = \rho {v_{sxy}}^2$$

3.2 ACOUSTIC ANISOTROPY MEASUREMENTS

The samples studied were first examined by Cholach et al. (2005) and were derived from near the Annabel Lake shear zone in the Flin Flon Belt of the Trans-Hudson Orogen. Additional details on the geology of the region including maps and additional references can be found in Lucas et al. (1994) and Cholach et al. (2005). The mineralogical composition for each sample set is given by **Table 4**

Table 4: Mineral compositions of metamorphic samples studied as determined in Cholach et al. (2005).

Sample Set	*Total*	*Quartz*	*Biotite*	*Altered*	*Plagioclase*	*Hornblende*	*Epidote*	*Calcite*	*Accessory*	*Staurolite*	*Opaque*	*Other*
9318	98.2	51.3	38.6	8.3								1.8
9320	92.5	31.6	34.9		12.2					11.6	2.2	7.5
N6	98.6	7.6	9.7		56.5	20.9			3.9			1.4
VOL I	96.6	13.2			16.3	67.1						3.4
VOL B	93.9	22.5	8.3		61.2						1.9	6.1

3.2.1 Sample Preparation

Each specimen was cored along three mutually orthogonal directions following as outlined by Cholach (2005) shown in **Figure 27**. The cores were originally cut with a diamond bit and have a measured diameter of 2.54cm and range in length from 2 cm to 5 cm. Ideally, a core was taken parallel (X plug), and perpendicular (Y plug) to any observed lineation direction within the plane of foliation and a third core was taken perpendicular to the foliation direction (Z plug). If there was no observed lineation, then the X and Y plugs were taken perpendicular to each other in the foliation plane. If there was no observable fabric, then the Z plug was taken vertically, and the X and Y plugs were taken horizontally as mutually orthogonal to this. The core plug samples were then prepared by grinding both faces flat and parallel to within 0.01mm. A full description of the sample preparation and experimental setup is detailed in Cholach et al. (2005)

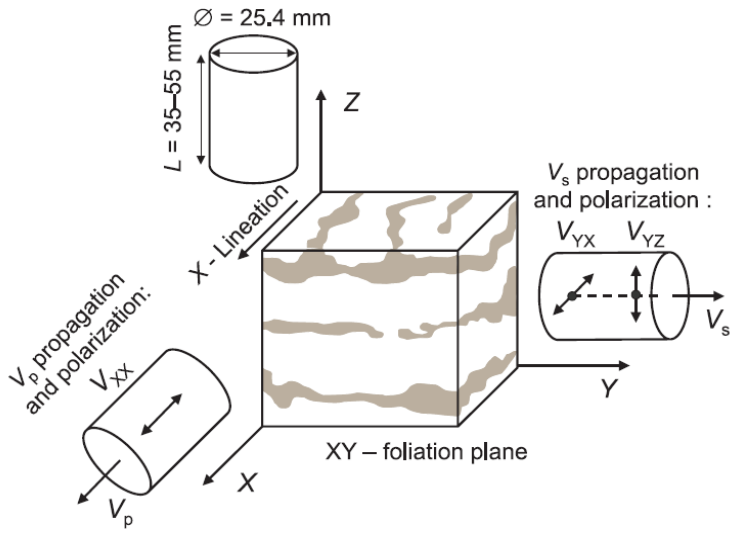

Figure 27: Schematic of the X, Y and Z core plug coordinate system orientation relative to the visual fabric. The XY plane was chosen to contain any foliation within the sample with the X-axis being along any visible lineations within the sample. Velocities are denoted by subscript propagation directions and polarizations respectively (Cholach et al., 2005).

3.2.2 Measurement Technique

An ultrasonic pulse transmission was used to measure the *p* and s-*wave* velocities through the use of piezoelectric endcaps in this thesis and by Cholach et al. (2005). Each endcap schematically shown below in **Figure 28** consisted of an aluminum cap (grey) and a transducer stack (blue). The piezoelectric ceramic p-wave (round) and s-*wave* (square) transducers produced a 1MHz signal. These transducers were bonded to copper electrodes (yellow) by a conductive silver epoxy and connected to an electrical function generator. A voltage was applied across each piezoelectric transducer to generate an ultrasonic wave, which then passed through the sample and was recorded on the corresponding opposite transducer and measured as a generated voltage. The waveforms recorded consisted of at least 300 stacked signal transmissions to further improve the signal to noise ratio.

Figure 28: Schematic of endcap design and sample configuration. Transducers (blue) are attached to aluminum endcaps (grey) or copper electrodes (yellow) by conductive silver epoxy. The transducer assembly was then sealed in a 5-minute epoxy to prevent damage.

3.2.3 Uniaxial Acoustic Measurements with Pressure

The *p-wave* velocities for several rhyolite core plug samples were previously measured at elevated pressure by Chloach et al. (2005). This was done to help characterize the change in acoustic properties due to the higher confining pressure closing microfractures between the constituent grains. This will result in any observed anisotropy being the result of a lattice preferred orientation (LPO) or another textural element. The same design of endcap shown in **Figure 28** was used, however, for these measurements only the p-waves were recorded by Cholach et al. (2005) on the subset of core plugs examined in this thesis. To prevent hydraulic oil from contaminating the samples, each of the core plugs was sealed between the endcaps inside of a rubber hosing before measurement in the pressure vessel, **Figure 29**. Various confining pressures ranging from atmospheric pressure up to 300 MPa were used to measure the change in acoustic travel time with the closing and re-opening of the microfractures/pore spaces within each sample.

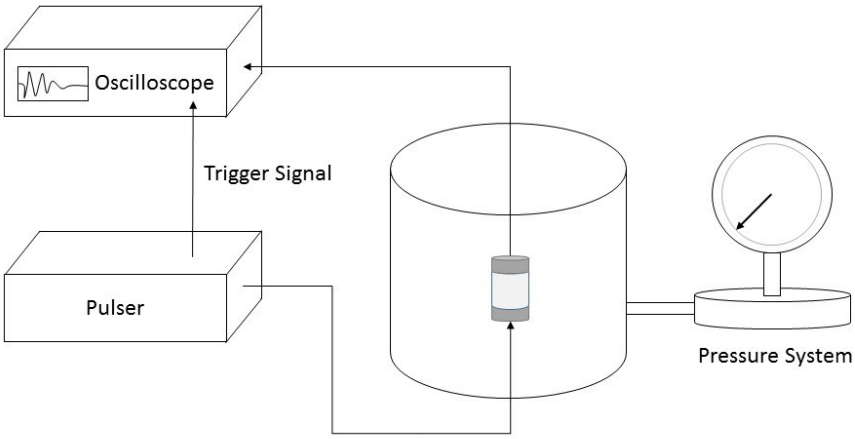

Figure 29: Schematic of pressure vessel configuration used to measure the ultrasonic velocities of various samples by Cholach et al., (2005) at a variety of confining pressures ranging from 0MPa to 300MPa.

The results of this previous study reported in Cholach et al. (2005) demonstrated the presence of some microscopic fractures within the samples as they opened and closed. This effect was observed as a change of acoustic velocity within the samples, and as a hysteresis between the up and down pressure cycles for each sample. These fractures were found to be subparallel to the foliation plane with the greatest velocity gradient with pressure being observed in waves propagating perpendicular to the plane of foliation. However, this velocity gradient was quite low and became quasilinear at low confining pressures starting around 150MPa which is much lower than the 200-300MPa onset suggested in literature (Birch, 1960, 1961; Cholach, 2005). This combined with the low velocity gradient indicated that the fractures did not play a significant role in terms of observed anisotropy which is consistent with a relatively low volume of fracture porosity which was estimated to be about 1% by Cholach et al. (2005). The results of this study for the subset of samples measured in this thesis are summarized in **Table 5** modified from Cholach et al. (2005). From the subset examined in this thesis it was previously found that the elastic symmetries were primarily orthorhombic in geometry with $C_{11} \neq C_{22} \neq C_{33}$ for the Vol-I, 93-18, and 93-20 sample sets. One sample set, N6, displayed a transversely isotropic geometry with $C_{11} = C_{22} \neq C_{33}$ and the Vol-B sample set was shown to be quasi isotropic with $C_{11} \approx C_{22} \approx C_{33}$.

Table 5: Elastic coefficients as determined by Cholach et al. (2005) for each sample set examined. The polarization is denoted as the direction of propagation and the direction of particle motion. For example the XX notation represents propagation along the X axis with

particle motion also along X denoting a *p-wave*. The C elements refer to the coefficients from the C tensor in **eq. 14**. In this case $C_{11,}$ C_{22}, and C_{33} are all elements along the main diagonal and can be calculated from the observed velocities via **eq. 42** as elements a, d, and f respectively.

Polarization	*XX*	*YY*	*ZZ*	*Elastic*
Sample Set	C_{11}	C_{22}	C_{33}	*Symmetry*
Vol I	*151*	*143*	*118*	*Orthorhombic*
Vol B	*91*	*90*	*88*	*Quasi-Isotropic*
93 18	*90*	*101*	*96*	*Orthorhombic*
93 20	*106*	*121*	*95*	*Orthorhombic*
N6	*120*	*121*	*101*	*Transversely Isotropic*

Previously shear wave anisotropy was observed by measuring the vertical and horizontal polarity transducers within the endcap during the high confining pressure tests done by Cholach et al. (2005). However, these high pressure *s-wave* measurements were not performed on the sample subset examined in this thesis. This gap will be supplemented by the work presented in **section 3.2.3**.

3.2.4 Atmospheric Pressure Shear Wave Anisotropy

In order to expand upon the work done previously by Cholach et al. (2005) shear wave anisotropy was measured for this thesis on the subset of samples examined by me at the University of Alberta. To accomplish this, the endcaps were first calibrated to account for the extra travel time that was due to the signal traveling through them and not the sample. The calibration time for *p* and *s-wave*s in the endcaps was found to be 8.23×10^{-6}s and 1.727×10^{-5}s with the total travel distance in aluminum measuring 48.8mm and 50.6mm respectively; this translated to a measured *p-wave* velocity of (5930m/s) and *s-wave* velocity of (2930m/s). There is the potential for some discrepancy between the *p-wave* measurements due to the short distance causing overlap of the initial pulse signal with the transmitted *p-wave*. To measure the acoustic velocities, the caps were bonded to the sample with a thin layer of molasses, which allowed for a stronger coupling to increase the signal to noise ratio. However, this could be further improved by performing the measurements at a higher confining pressure.

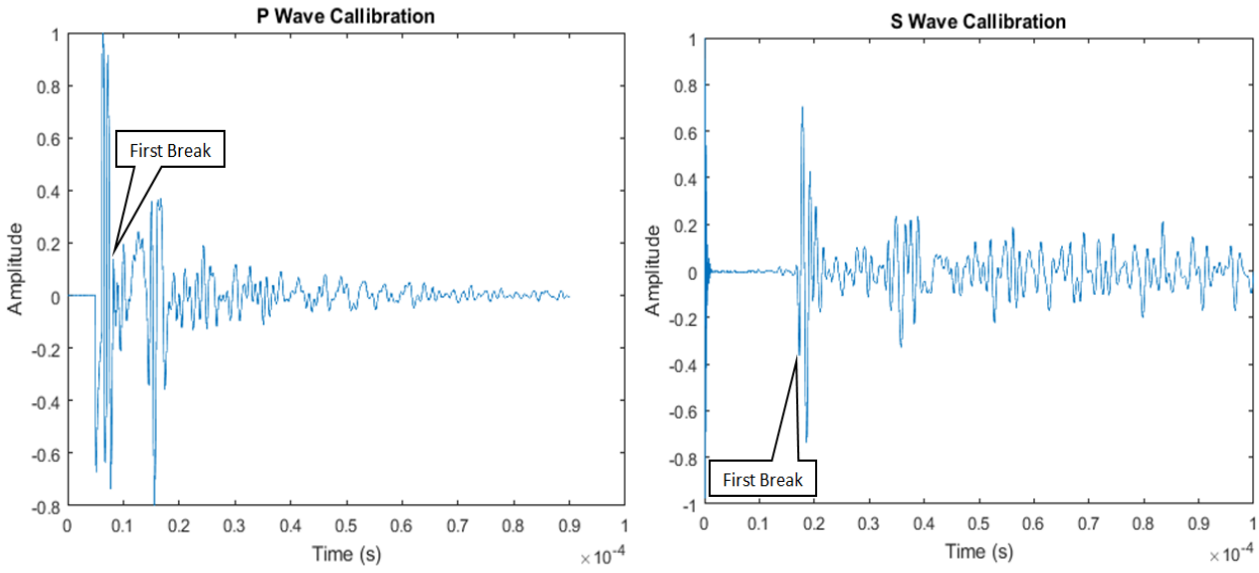

Figure 30: Ultrasonic waveforms measured for both compressional and shear wave signals at atmospheric pressure as measured during the calibration run for both the P and *S-wave* signals at atmospheric pressure. In addition to calibration times, these waveforms were also used to determine the initial wavelet for both the *p* and the *s-wave* signals, which aid in identifying the appropriate first break arrival time for the ambient pressure measurements.

Shear wave anisotropy at atmospheric pressure was measured by aligning the *s-wave* transducer polarity on both the transmitting and receiving endcaps with the x axis of the core plug, (**Figure 28**) this initial polarity was set to an azimuth of 0° as defined in **Figure 31**. Next the sample was rotated clockwise by 22.5° about it's z axis (to align with the blue plane in **Figure 31** for example) and the waveform was measured again. This was repeated in incriments of 22.5° from an azimuth of 0° to 337.5°. The resulting waveforms were then recorded (**Figure 32**) and used to determine the arrival time of the shear wave. Measuring the arrival time of the shear wave with respect to azimuth gave the s-wave velocity anisotropy for polarizations about the axis of each core plug. These arrival times demonstrate shear wave anisotropy within the sample with a fast polarization often aligned parallel to a textural element along the plug x axis (θ=0°) and a slow polarization aligned along the plug y axis (θ=90°). These measurements were carried out for a number of samples and the velocity variations are summarized in **Table 6** with reference to the coordinate system defined in **Figure 31**. This was done to (i) confirm that the fast and slow s-wave velocities did, in fact, align with the observable textural elements within the samples and (ii) further reinforce our understanding of the elastic anisotropy within each sample.

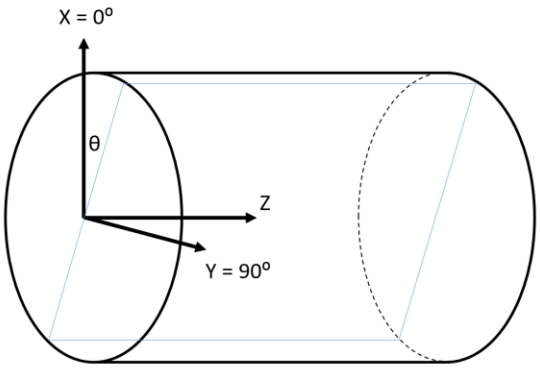

Figure 31: Schematic of core plug local coordinate system and the *s-wave* velocity along the Z axis polarized within the blue plane at an azimuth of θ clockwise from the X axis which was always aligned prefferentially along a visible texture element. This local coordinate system will be shared with the magnetic measurements in **Chapter 4**. For the the Z core plug this would be a rotation about the Z axis or measuring the *s-wave* anisotropy within the XY plane. Similarly the Y plug will measure the ZX plane anisotropy and the X plug will measure the anisotropy in the ZY plane.

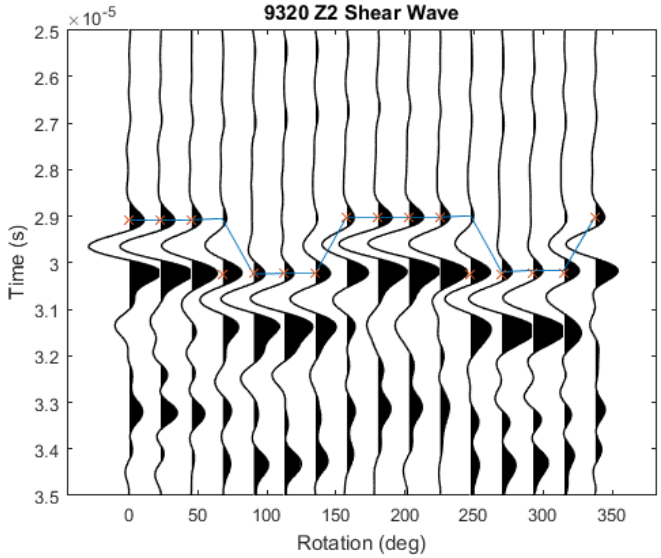

Figure 32: Shear wave arrival times measured within the 9320 Z2 core plug sample. Clear differences in velocity exist for orthogonal polarizations within the sample. The fast polarization is approximately oriented parallel to the X-axis vs. the slower Y axis.

3.3 RESULTS

For this study we are particularly interested in the degree of shear wave anisotropy observed within each sample as well as the orientations of the fast and slow *s-wave* polarities relative to the core plug axis.

Table 6 summarizes these observations for the core plugs measured in this thesis. From this we can clearly see that the azimuth of the fast *s-wave* polarity is often parallel or subparallel to the x axis of the core plug which has been defined parallel to an observable textural element.

Table 6: Measured s-wave velocities. Fast and slow s-wave polarities have been measured and their orientation with respect to the local core plug coordinate system. Note the core plug name does not necessarily represent the direction relative to textural elements. Textural orientation is given by the propagation direction column.

Sample Name		Propagation Direction	S max (m/s)	S min (m/s)	θ_{max} °	θ_{min} °	Difference (m/s)
93-20	X1	X	1831.9	1683.7	0.0	90.0	148.1
	Y1	Z	1665.2	1651.2	135.0	45.0	14.1
	Z2	Y	1804.6	1645.8	22.5	112.5	158.7
Vol B	X1	X	3120.5	3092.0	180.0	270.0	28.5
	X2	X	3034.6	2970.3	22.5	112.5	64.3
	Y1	Y	3144.1	3029.5	337.5	67.5	114.7
	Z2	Z	3284.5	3196.3	180.0	90.0	88.1
Vol I	Y1	Z	2087.5	2049.8	135.0	45.0	37.7
	Z2	Y	2088.3	2071.2	90.0	180.0	17.1
N6	X1	X	4023.6	3297.9	270.0	0.0	725.7
	Z1	Z	3795.1	3377.6	0.0	90.0	417.4
93-18	Z1	Y	3372.8	3072.8	315.0	45.0	300.0

3.4 CONCLUSIONS

It was found by Cholach et al. (2005) that most of the samples studied from both collections displayed significant *p-wave* velocity anisotropy which was due primarily to the presence of microfracture porosity and mineral alignment within the sample resulting from lattice prefferred orientation. Through the use of velocity vs. confining pressure relationships, the effects of the microfractures were isolated from the mineral components and it was found that these fractures only made a small contribution to the overall anisotropy of the sample. The primary control on acoustic anisotropy was found to be the mineral lattice preferred orientation. The sample subset studied in this thesis displayed either orthorhombic or transversely isotropic symmetries with one sample set classified as quasi isotropic. This thesis expanded on these results to help further delineate the anisotropy present within various sample sets. This was done by measuring the *s-wave* anisotropy within a subset of core plugs at atmospheric pressure. Shear wave anisotropy was found in all of the sample sets studied in this work and it preferentially aligned along textural visual elements that were observed within each sample. The maximum shear velocity was preferentially within the plane of foliation (0° on plugs with X or Y propagation directions). These qualitative results will be compared with the magnetic fabric observations in **Chapter 4** to help define the rock fabric.

CHAPTER 4: MAGNETIC ROCK FABRIC

In **Chapter 1**, the various effects of magnetic anisotropy on singular grains were discussed. In this chapter, the concepts that applied to singular grains are expanded to encompass large assemblages of magnetic grains which make up rock samples. The variations of magnetic susceptibility and magnetic remanence within a rock sample and their orientations are known as the anisotropy of magnetic susceptibility (AMS) and anisotropy of magnetic remanence (AMR) respectively (Tarling and Hrouda, 1993). These properties define the magnetic fabric within materials and for rock samples are very sensitive indicators of rock texture, which can be used to determine the origin and structural development of the rock. This is done by taking the total magnetic fabric seen within a sample as the sum of all the contributions from each magnetic component within the assemblage (Tarling and Hrouda, 1993).

The magnetic fabric within a sample will be the result of the net contributions of the shape and crystallographic orientation of every grain comprising the rock, which can be in turn interpreted and compared to other petrofabric techniques such as electrical resistance anisotropy or elastic anisotropy, the latter of which will be the focus of this study. However, the use of magnetic methods has the advantage over these other methods in that magnetic measurements are very precise, acquired quickly, and relatively inexpensive. One use of these methods is for paleomagnetic studies which require the collection of oriented rock samples, where the natural remanent magnetization present in each sample will be measured to determine the paleomagnetic history. The remanent magnetization of each sample can be influenced by anisotropy via depositional and or structural factors between the time of formation and the present day (Rochette et al., 1992; Tarling and Hrouda, 1993; Borradaile and Jackson, 2010). The present study in this thesis is not focused on the natural remanent magnetization of the samples nor their structural evolution. Instead, we are purely interested in using the AMS and AMR to define the sample rock fabric relative to the local sample coordinate system. For this reason the samples are oriented based on the observed rock fabric and not on a geographic coordinate system. Any magnetic anisotropy can be interpreted as the result of contributions from crystalline alignments and the overall grain shape, which will then be later compared to any measured acoustic anisotropy. The goal of this is to uncover any relationship that may exist between the various anisotropic methods with a particular interest to use one method as a tool in predicting the properties of another.

For this section, the magnetic anisotropy will be defined as the variation in the magnetic properties of a rock sample due to a change in the direction of observation (Tarling and Hrouda, 1993). The AMS fabric will be the result of the ferrimagnetic, paramagnetic and diamagnetic components within the sample. Ferrimagnetic material, in particular, will greatly impact the AMS value as even a small amount will be able to overshadow the other components (as discussed in **Chapter 1**). In addition to its relatively strong magnetic susceptibility, a ferrimagnetic material also has the capacity to retain a magnetization in the absence of an applied magnetic field. This means that any laboratory controlled AMR fabric measured within the rock samples can be used to help isolate the ferrimagnetic contributions. The comparison of the AMS to the AMR fabric is therefore useful as it allows us to determine the contributions of

paramagnetic (such as chlorite or illite), diamagnetic (such as quartz or calcite) and ferrimagnetic (such as magnetite) constituent components to the overall magnetic rock fabric. In order to fully describe these fabrics, the magnetic anisotropies (both AMS and AMR) are each expressed as a second-order tensor, or more conveniently as an anisotropy ellipsoid where the shape and orientation of each ellipsoid will define the total magnetic fabric seen within the rock sample (Potter, 2004).

4.1 ANISOTROPY OF MAGNETIC SUSCEPTIBILITY

For most rock samples, the magnetization that is induced by a weak magnetic field will vary depending on the direction of the applied magnetic field, to some degree making these rocks magnetically anisotropic. In reality, there are few rock samples which display a uniform magnetization independent of the applied field direction. These few samples are said to be magnetically isotropic. Whether isotropic or anisotropic, the magnetic susceptibility of a sample can be described as a symmetric second-order tensor. The magnitude of this anisotropy ellipsoid is controlled by the magnitude of anisotropy of the individual particles as well as the degree to which they are aligned. The petrofabric described by the AMS ellipsoid is the result of the intrinsic magnetic properties within the studied material. For rocks, this AMS is largely the result of preferred mineral orientation and grain shape. However, there is some contribution from the preferred crystallographic orientation (Tarling and Hrouda, 1993). The preferred crystallographic orientation will result in a magnetocrystalline anisotropy. This arises from lattice forces that act on the electron spin configuration within the crystal lattice along a specific plane or axis within the crystal structure. The other major source of anisotropy is determined by the shape of the mineral grains. As discussed in **Chapter 1** the effects of shape anisotropy are generally stronger than magnetocrystalline anisotropy. The summation of both these factors will determine both the magnitude and direction of the AMS observed within most rock samples.

An anisotropy ellipsoid can be defined for both the magnetic susceptibility and the magnetic remanence seen within a sample. As mentioned in **Chapter 1** care must be taken when interpreting the AMS ellipsoid as the effects of shape anisotropy for a ferrimagnetic grain will differ immensely depending on the number of magnetic domains that are contained. For this reason, it is useful to measure the AMR of a sample as well as the AMS. For simplicity, the mathematics and parameters will be determined in terms of the magnetic susceptibility ellipsoid, however these methods are analogous in defining the remanence ellipsoid.

4.2 MATHEMATICS OF AMS

Magnetic susceptibility can be defined in two fashions, one is the susceptibility per unit mass, and the other is per unit volume. Generally speaking, it will be more beneficial to think of it in terms of mass susceptibility as this value is independent of sample size and porosity which allows for a direct comparison of samples. This mass susceptibility is defined as (Tarling and Hrouda, 1993):

$$\chi = \frac{J}{H} \tag{43}$$

where χ is the mass magnetic susceptibility, J is the magnetization per unit mass, and H is the applied magnetic field strength.

When applied to geologic purposes the AMS is useful in describing the magnetic rock fabric. The magnetic fabric is caused by the preferred alignments of magnetic grains and minerals. In general, the preferred crystal orientation has some control over grain shape and helps to determine the AMS vector that is observed. The measured susceptibility of a rock sample represents the sum of all contributions from the material that makes up the rock (Tarling and Hrouda, 1993; Spaldin, 2010).

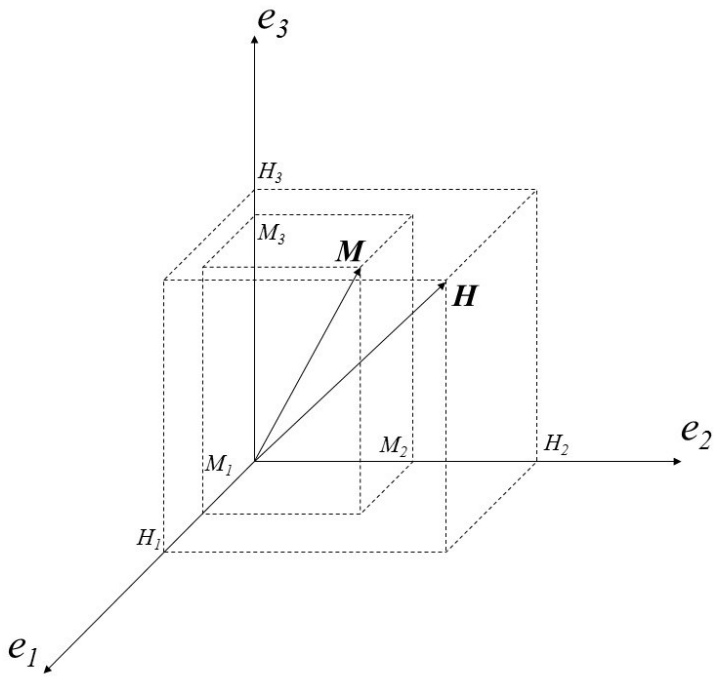

Figure 33: Schematic of magnetization vector M as a result of the applied field H. Modified from Z. Han (2005).

Figure 33 shows a schematic of the magnetization that results from an externally applied magnetic field. The magnetization **M** of a magnetically anisotropic sample (with susceptibility χ) when exposed to a low magnetic field **H** (≤1mT) can be expressed in expanded form as:

$$\boldsymbol{M} = M_1 e_1 + M_2 e_2 + M_3 e_3 \tag{44}$$

where:

$$\boldsymbol{H} = H_1 e_1 + H_2 e_2 + H_3 e_3 \tag{45}$$

The magnetic susceptibility χ can be shown as a second-order tensor, shown below in matrix notation.

$$\chi = \begin{pmatrix} \chi_{11} & \chi_{12} & \chi_{13} \\ \chi_{21} & \chi_{22} & \chi_{23} \\ \chi_{31} & \chi_{32} & \chi_{33} \end{pmatrix} or \begin{pmatrix} \chi_{xx} & \chi_{xy} & \chi_{xz} \\ \chi_{yx} & \chi_{yy} & \chi_{yz} \\ \chi_{zx} & \chi_{zy} & \chi_{zz} \end{pmatrix} \quad (46)$$

As seen in **Figure 33,** H and M are not necessarily parallel. The magnetization can be expressed in terms of the sample's magnetic susceptibility χ and applied field H such that:

$$\begin{pmatrix} M_1 \\ M_2 \\ M_3 \end{pmatrix} = \begin{pmatrix} \chi_{11}H_1 + \chi_{12}H_2 + \chi_{13}H_3 \\ \chi_{21}\mathrm{H}_1 + \chi_{22}H_2 + \chi_{23}H_3 \\ \chi_{31}H_1 + \chi_{32}H_2 + \chi_{33}H_3 \end{pmatrix} \quad (47)$$

or in more general terms:

$$M_i = \chi_{ij}H_j \ \ (i,j = 1,2,3) \quad (48)$$

It is important to note that the magnetic susceptibility tensor χ is symmetric and can be simplified to:

$$\chi = \begin{pmatrix} \chi_{11} & \chi_{12} & \chi_{13} \\ \chi_{12} & \chi_{22} & \chi_{23} \\ \chi_{13} & \chi_{23} & \chi_{33} \end{pmatrix} or \begin{pmatrix} \chi_{xx} & \chi_{xy} & \chi_{xz} \\ \chi_{xy} & \chi_{yy} & \chi_{yz} \\ \chi_{xz} & \chi_{yz} & \chi_{zz} \end{pmatrix} \quad (49)$$

This reduces the number of independent components required to define the susceptibility ellipsoid to 6. The components seen in the susceptibility tensor depend on the coordinate system in which they are defined. Therefore, it is possible to define a coordinate system for anisotropic materials such that only the diagonal elements (χ) are nonzero, as shown by (Tarling and Hrouda, 1993):

$$\chi' = \begin{pmatrix} \chi'_{11} & 0 & 0 \\ 0 & \chi'_{22} & 0 \\ 0 & 0 & \chi'_{33} \end{pmatrix} \quad (50)$$

These remaining diagonal elements are the principle axes of the magnetic susceptibility ellipsoid (χ_1, χ_2, and χ_3 in **Figure 6**. For a magnetically isotropic material, the off-diagonal elements are always equal to zero independent of the choice of coordinate system. The ideal goal for describing the magnetic anisotropy of an object is to determine the magnitude and orientation of the three principle axes with respect to the original coordinate frame. These principle axes can be found by measuring the six independent values of the susceptibility matrix. For this investigation, the coordinate system used will be in reference to the observed fabric of the rock samples as shown in **Figure 27**.

To measure the anisotropy, a sample must be placed at a variety of orientations while being exposed to a uniform magnetic field H. This will induce a magnetization M within the sample, however as was shown in **Figure 33** this magnetization is not usually aligned along the magnetic

field **H** if the sample is anisotropic. Only the projection of the magnetization vector onto the applied magnetic field unit vector is measured. In order to generate the full susceptibility tensor χ we must measure a variety of different directions and their corresponding susceptibility values and calculate back to the proper components. Care should be taken to choose an easily recognized direction to keep the calculations simple. We then take these multiple directional values of susceptibility and then back-calculate to obtain the tensor χ' through least squares methods. Even though the mirrored off-diagonal elements of χ are theoretically equal ($\chi_{yx} = \chi_{xy}$ etc.) they are taken as an average $(\chi_{xy}+\chi_{yx})/2$ for example, to reduce experimental errors.

The six independent coefficients χ are then used in a Molspin anisotropy delineator program that has been modified to compute a complete anisotropy ellipsoid (Stephenson et al., 1986). This gives the magnitudes and orientations of the principle axes for the samples as the eigenvalues and eigenvectors of the tensor respectively and can be applied to produce both the magnetic susceptibility ellipsoid as well as the IRM ellipsoid.

4.3 ANISOTROPY OF MAGNETIC REMANENCE

In this section, we will discuss the various methods that measure an induced magnetization. For many of the methods described below (gyroremanent magnetization, GRM, excluded), the magnetic remanence can be characterized as an anisotropy ellipsoid in the same manner as the magnetic susceptibility. This similarity allows us to apply the same mathematical methods used to calculate AMS in calculating the AMR (specifically IRM for this study) by replacing the susceptibility matrix (**χ**) with the magnetization matrix ($\mathbf{M}_{IRM}$).

$$M_{IRM} = \begin{pmatrix} \mathrm{M}_{11} & \mathrm{M}_{12} & \mathrm{M}_{13} \\ \mathrm{M}_{21} & \mathrm{M}_{22} & \mathrm{M}_{23} \\ \mathrm{M}_{31} & \mathrm{M}_{32} & \mathrm{M}_{33} \end{pmatrix} \tag{51}$$

where:

$$M_{ij} = M_{ji} \tag{52}$$

There are many methods used in determining the magnetic remanence within a rock sample. The different AMR methods discussed can be used to generate an anisotropy ellipsoid by measuring the components of magnetization produced by a magnetic field that is applied successively along the x, y and z-axis of the sample (unless otherwise stated). In order to generate an AMR ellipsoid the nine components of magnetization (6 of which are independent) need to be resolved. Although the method of measurement is different for each technique after acquisition, the AMR ellipsoid is calculated from **M** in the same way as the AMS ellipsoid is calculated from **χ**. The following will act as a summary to discuss the advantages and disadvantages of each method. This will include the basic underlying principles for each as well as what each method is meant to detect. For the following methods, the idealized sample and orientations referenced will be done in relation to the core plug schematic shown in **Figure 27**. A more in-depth description for each of the magnetic remanence methods can be found in Potter (2004).

4.3.1 Thermal Remanent Magnetization (TRM) and Anisotropy

This method is meant to simulate the conditions which produce a natural thermoremanent magnetization (TRM) within an anisotropic sample exposed to the Earth's magnetic field (Tarling and Hrouda, 1993; Potter, 2004). This process is accomplished by heating a rock above its Curie point (to remove any remanent magnetization) and then cooling it in a weak magnetic field (about the same magnitude of the Earth's magnetic field) aligned parallel to one of the sample axes. The x, y and z components of magnetic remanence are then measured for the applied field direction. The sample is then reoriented along a different orthogonal axis, and the measurement is repeated for each successive magnetization direction. These nine magnetization components are then used to determine an anisotropy ellipsoid through least squares methods (Stephenson et al., 1986). This method requires that no chemical or physical changes such as oxidization or welding of adjacent particles occur in the sample over the three heating and cooling cycles. Therefore special care should be taken such as heating the samples in a vacuum or a non-reactive gas. In addition to this, it is also important to use an identical magnetic field as well as the same heating, and cooling rates between each cycle as all of these factors will influence the acquired magnetization.

4.3.2 Isothermal Remanent Magnetization (IRM) and Anisotropy

Isothermal remanent magnetization (IRM) gives a rapid non-destructive alternative to TRM. The main disadvantage of TRM measurements is their potential to introduce chemical changes within a sample due to oxidization during heating. IRM and the following methods remove this potential source of error by maintaining a constant temperature (usually room temperature) (Potter, 2004). Another benefit to the use of the IRM method is that it gives the strongest response of the different remanence anisotropy methods, and is particularly useful at identifying low concentrations of remanence carrying particles within samples. It is also possible to distinguish between different size distributions of remanence carrying particles based on the observed response to different applied magnetic field intensities. Additionally, IRM measurements show a correspondence with TRM results (Stephenson et al., 1986).

IRM measurements consist of first demagnetizing the sample ideally through the use of a tumbling demagnetizer (which avoids the introduction of unwanted gyroremanent magnetization, GRM, components). However, if static or rotational demagnetization techniques are used, it is possible to correct for the unwanted GRM components (Stephenson, 1993; Potter, 2004). The demagnetized sample is then exposed to a short pulse direct field (DF) along the x axis. After the field is applied and removed, the resultant magnetization is measured in the x, y and z directions. The sample is then demagnetized, and the procedure is repeated with the DF aligned along the y and z axes resulting in nine components of magnetization being recorded, which can then be used to calculate the IRM anisotropy ellipsoid for the sample.

4.3.3 Viscous Remanent Magnetization (VRM) and Anisotropy

This method is primarily employed to detect small single domain particles near the superparamagnetic boundary. Functionally it works on the same principles as the IRM measurements except that it utilizes a lower field applied over a longer period. The magnetic grains that are most affected by this method are limited to those that have relatively short

relaxation times. However, these are potentially aligned in the same direction as the larger stable single domain (SSD) and multidomain (MD) grains that are of more interest in for paleomagnetic studies. The long exposure time required for these viscous particles to acquire a remanence makes this method significantly slower than the other magnetization measurement methods.

4.3.4 Anhysteretic Remanent Magnetization (ARM) and Anisotropy

Anhysteretic remanent magnetization (ARM) was developed as an analog for TRM methods under exposure to the Earth's magnetic field. This method requires the sample to be exposed to a small direct magnetic field (DF) which represents the Earth's Field and simultaneously to an alternating field (AF) which is meant to simulate the thermal agitation used in TRM. This method has the advantage over TRM methods in that it does not require heating of the sample and can be performed in a laboratory at room temperature. However, the ratio between TRM and ARM can change with grain size and concentration (Potter, 2004). There are three main approaches to measuring ARM anisotropy: holding the sample stationary for a static ARM, rotating the sample about each axis to produce a rotational ARM, and by tumbling the sample to measure the tumbling ARM. Each of these methods has different advantages and disadvantages that are discussed in Potter (2004), however these methods will not be used in this thesis.

4.3.5 Gyroremanent Magnetization (GRM) and Anisotropy

Measuring the gyroremanent magnetization (GRM) of a sample is an extremely sensitive method to determine magnetic anisotropy within a sample. Specifically, this method is most sensitive to the distribution of stable single domain (SSD) particles as they will preferentially acquire a GRM even with a low anisotropic distribution (Stephenson, et al., 1986; Potter and Stephenson, 1988; Potter, 2004). GRM is the remanent magnetization acquired by a sample when it is exposed to an alternating magnetic field and is only acquired if the sample contains an anisotropic distribution of SSD particles (Stephenson, et al., 1986). GRM is the precession of magnetic moments about the long axis of a ferrimagnetic particle. An anisotropic distribution of SSD particles will produce a GRM due to an alignment of the precession axes. This results in the magnitude of the GRM acquired to be proportionally dependant on the anisotropy of the sample within the plane that is perpendicular to the applied alternating magnetic field. More specifically the GRM vector will be produced perpendicular to both the easy axis of the SSD grain and the direction of H_{app}.

This method will not similarly determine an ellipsoid as no bulk measurement can be taken. It can, however, create normalized coefficients C_1, C_2, and C_3 that are related to the magnitude of anisotropy in the YZ, ZX and XY planes of the sample (Potter and Stephenson, 1988).

The GRM anisotropy requires the measured GRM components from at least six applications of the alternating field (AF) along two sets of orthogonal sample axes x, y and z as well as x' y' and z.'. If the sample has a weakly anisotropic SSD distribution, it is best to take more measurements by applying the AF along multiple planes rotated about three perpendicular axes, i.e., rotating the sample about the x, y, and z-axes. To remove a bias in observations, the sample should be tumble demagnetized between each application of the alternating field. To

further improve results and to remove any possible ARM components that may have been inadvertently introduced by a small remaining DF it is best to measure the GRM along antiparallel directions to create an average magnetization value. The large number of measurements required make this process time consuming for a sample and can take up to two days to complete depending on the number of planes investigated.

4.3.6 Demagnetization Method

To ensure a proper reading for the degree of remanence anisotropy within each of the samples, it is important to first remove any residual magnetization. This is necessary due to the unknown nature of this residual which could overprint onto the controlled remanence adding unnecessary uncertainty. In order to remove any remaining magnetization tumbling demagnetization was employed before each measurement as this will not induce any remanent magnetization in the sample itself nor does it run the risk of chemically altering the sample that is inherent in thermal demagnetization processes. To demagnetize the sample, it was placed into a tumbler and demagnetized by tumbling while being exposed to an alternating magnetic field AF of 80.0 mT for 10s. After which the magnetization of the sample after the initial demagnetization was measured to ensure that the demagnetization was successful. If a significant magnetization remained after the initial demagnetization, then the sample was demagnetized a second time to remove any remaining effects. The AF field strength of 80 mT was chosen because it was sufficiently large compared to the direct magnetic field strength of 40 mT used to impart the IRM on the sample. Generally speaking, this demagnetization technique was adequate to remove any remaining remanence.

Table 7: Summary of magnetic anisotropy techniques, equipment, and the advantages and disadvantages of each. Modified from Potter (2004).

Summary of Magnetic Anisotropy Techniques

Anisotropy Method		Equipment	Time	Advantages	Disadvantages
Thermal Remanent Magnetization (TRM)		Furnace and Helmholtz Coil	Several Hours	Direct simulation of natural TRM	Time Consuming Can cause Chemical Changes
Viscous Remanent Magnetization (VRM)		Helmholtz Cage or shielded DF Coil	Between one hour and several Days	Can isolate small SSD particles	Time Consuming Only measures small particles
Isothermal Remanent Magnetization (IRM)		Pulse Magnetizer	Less than half an hour	Fast and has strongest response	Non linear in a low Direct Field
Anhysteretic Remanent Magnetization (ARM)	Static ARM	AF coil and a DF Coil or Helmholtz Cage	Less than one hour	Less than one hour	Can cause a GRM
	Rotational ARM	Rotational Magnetizer or Turbine in a shielded AF Coil	Half an hour	No static GRM produced	Will produce RRM
	Tumbling ARM	Tumbler and Shielded AF demagnetizer	Half an hour	No RRM or GRM produced	Requires a tumbler
Gyroremanence Anisotropy	Rotational Remanent Magnetization (RRM)	Rotational Magnetizer or Turbine in a shielded AF Coil Shielded AF demagnetizer	Half an hour	Preferentially acquired by SSD particles	Specialist equipment needed
	Gyroremanent Magnetization (GRM)	Shielded AF demagnetizer	Between one and two days	Sensitive to SSD anisotropy	Very time consuming
Anisotropy of Magnetic Susceptibility (AMS)		Bulk Susceptibility Bridge AMS Delineator	Fast: Several minutes	Fast: Several minutes	Sum of all minerals, difficult to isolate specific contributions

4.5 SAMPLE DESCRIPTION

4.5.1 Sample Preparation

The general sample preparation of the core plugs was given in section 3.2.1 of **Chapter 3**. For the magnetic measurements, the samples used were cut to a length of 1-inch. **Table 4** details the mineralogical composition of each sample set. Generally speaking, the samples were cut along the plan outlined in **Figure 27,** which describes the orientation of the plugs relative to each other as well as to the direction of foliation. It is also important to remember that all measurements described below were conducted at room temperature of 21°C.

4.5.2 Bulk Magnetic Susceptibility

Perhaps the simplest magnetic property to measure is the total or bulk magnetic susceptibility of the rock. To measure the bulk magnetic susceptibility for each sample, a Molspin susceptibility bridge was used. The sample was placed within the bridge, and the magnetic susceptibility along its cylindrical axis was measured. Initially, the volume magnetic susceptibility was measured. However, this was then converted to the mass susceptibility to remove the effects of porosity and size variation between the samples, thus allowing them to be more directly compared. This conversion to the mass magnetic susceptibility χ_m is given by:

$$\chi_m = \frac{\chi_{raw}(9.702 \times 10^{-8})}{m} \tag{53}$$

where χ_{raw} is the raw measured magnetic susceptibility value, m is the mass of the individual sample in grams and 9.702×10^{-8} is a conversion factor related to the volume of the cylindrical sample. **Table 8** gives the corrected mass susceptibilities for each sample.

Table 8: Recorded mass susceptibility for the core plugs studied in detail.

Rock Sample	*Mass*	*Mass Susceptibility*
Plug	**(g)**	**(m^3/kg)**
9320 Z2	30	-2.141×10^{-5}
Vol I Z	32	1.019×10^{-4}
Vol B Z	29	7.853×10^{-3}
N6 X1	28	1.093×10^{-2}

From this data, we can see some significant variability between the mass susceptibility of each sample with several groupings emerging. The Vol B Z and N6 X1 have the strongest mass susceptibility by at least an order of magnitude when compared to the others. The 9318 and Vol I samples show an intermediate-mass susceptibility. 9320 is giving a diamagnetic response.

4.5.3 One Dimensional Anisotropy Comparisons

The mass magnetic susceptibility for each sample was compared with it's associated axial p-wave velocity for each core plug in this study. These values were normalized to allow for an easier comparison and are presented in **Figure 34** to **Figure 38**. **Equation 54** details the normalization of χ_m for plug i where n is the number of core plugs measured in a sample set, p wave velocities were normalized in a similar fashion.

$$\chi_{norm} = \frac{\chi_m}{\sum_{i=1}^{n} \chi_{mi}} \tag{54}$$

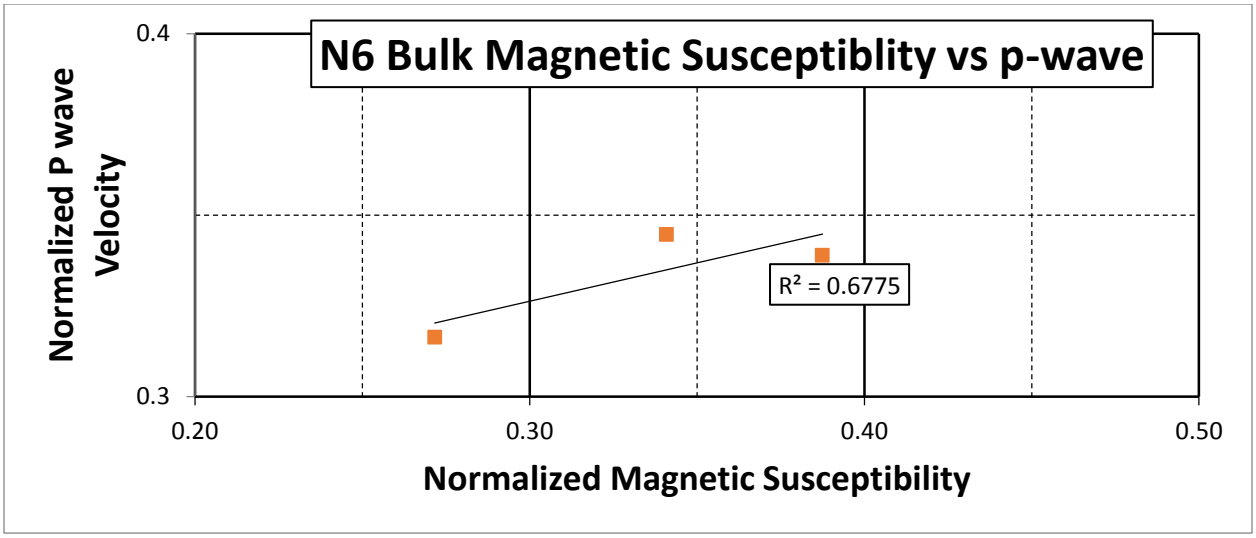

Figure 34: Normalized bulk magnetic susceptibility vs normalized p-wave velocity for the N6 sample set. The bulk susceptibility for each sample was measured as well as the uniaxial p-wave velocity for each core plug. These values were normalized to allow for an easier comparison between sample sets. These measurements were performed at atmospheric pressure.

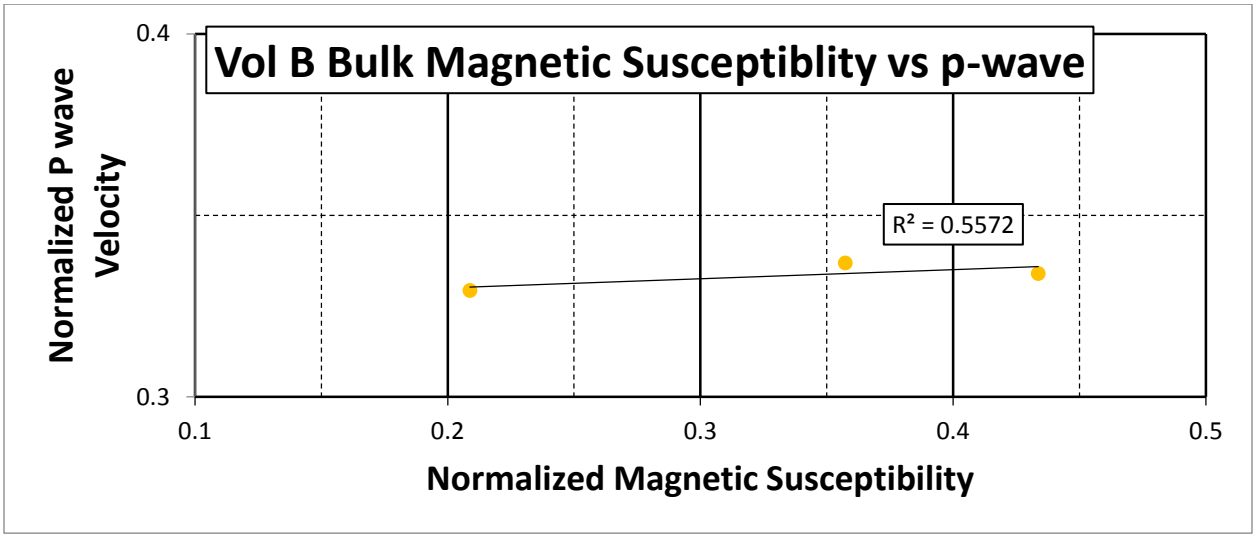

Figure 35: Normalized bulk magnetic susceptibility vs normalized p-wave velocity for the Vol B sample set. The bulk susceptibility for each sample was measured as well as the uniaxial p-wave velocity for each core plug. These values were normalized to allow for an easier comparison between sample sets. These measurements were performed at atmospheric pressure.

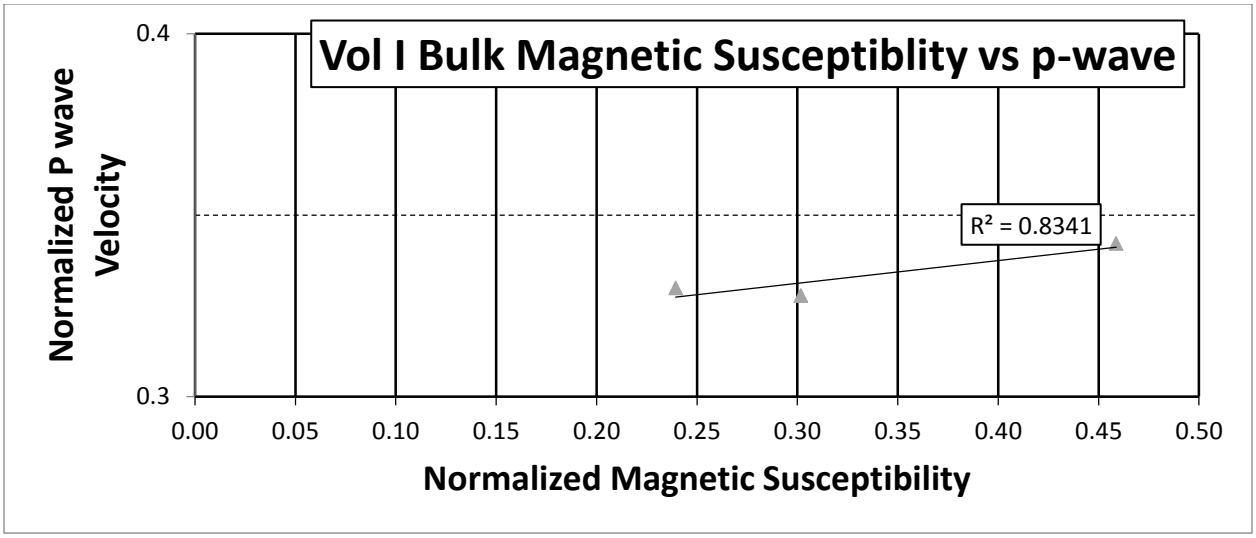

Figure 36: Normalized bulk magnetic susceptibility vs normalized p-wave velocity for the Vol I sample set. The bulk susceptibility for each sample was measured as well as the uniaxial p-wave velocity for each core plug. These values were normalized to allow for an easier comparison between sample sets. These measurements were performed at atmospheric pressure.

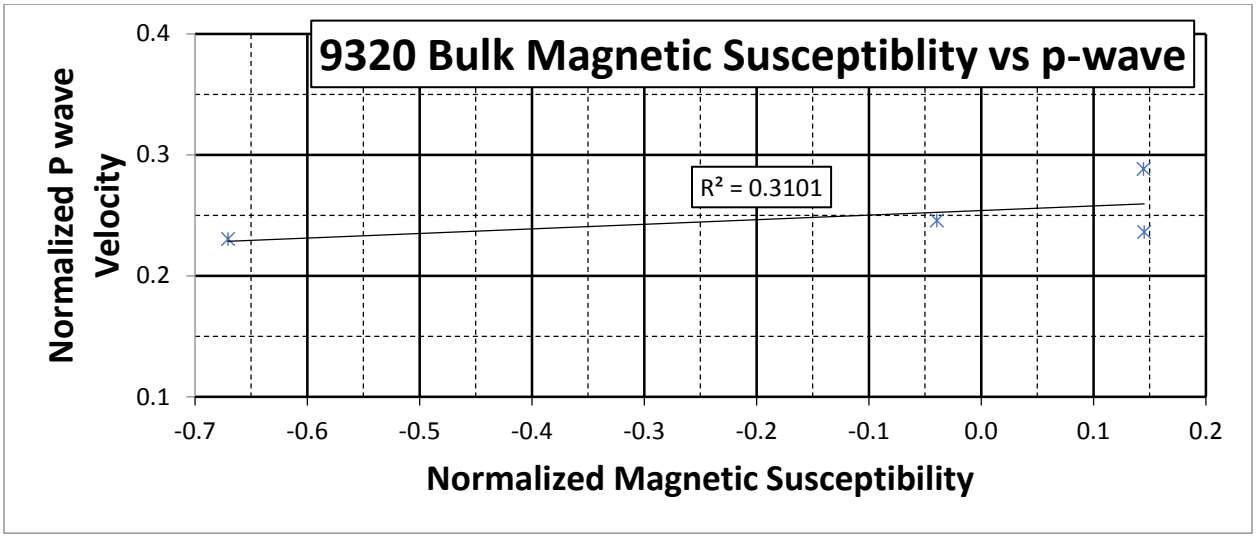

Figure 37: Normalized bulk magnetic susceptibility vs normalized p-wave velocity for the 9320 sample set. The bulk susceptibility for each sample was measured as well as the uniaxial p-wave velocity for each core plug. These values were normalized to allow for an easier comparison between sample sets. These measurements were performed at atmospheric pressure.

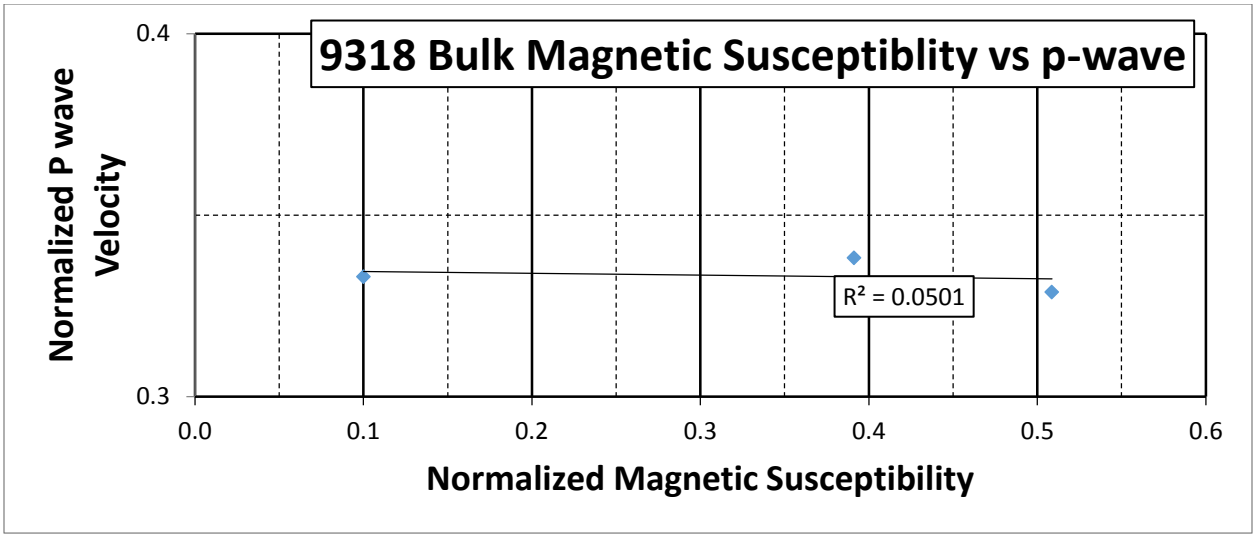

Figure 38: Normalized bulk magnetic susceptibility vs normalized p-wave velocity for the 9318 sample set. The bulk susceptibility for each sample was measured as well as the uniaxial p-wave velocity for each core plug. These values were normalized to allow for an easier comparison between sample sets. These measurements were performed at atmospheric pressure.

When comparing the above p-wave trends we can see that there is a correlation between the bulk magnetic susceptibility and the observed p-wave velocities for each sample set. However the strength of this correlation is highly variable

Sample sets 93-18 and Vol B both appear to not show a correlation between mass magnetic susceptibility and p wave velocities. Whereas other sample sets do show a more robust relationship between the magnetic susceptibility with Vol I giving the strongest correlation between the two parameters. This could be linked to the mineralogy of the samples because both N6 and Vol I have Hornblende as a large percentage of their composition which is has a high acoustic anisotropy. This correlation does not translate between sample sets. This method is best applied towards individual related sample sets. This trend could be improved by measuring the p-wave velocities at a high confining pressure to improve the coupling between sample and endcap.

4.5.4 Comparisons of Three Dimensional Magnetic Anisotropy (AMS, AIRM, and GRM) and Two Dimensional Acoustic Anisotropy (S-Wave)

There are also several interesting comparisons of 3D anisotropy which can be made in this section. The AMS, AIRM, GRM and acoustic anisotropies were compared to fully characterize a core plug's rock fabric. These comparisons were done on a per plug basis.

The Vol B Z plug is noted to have a visual fabric within the rock sample itself. This fabric appears to be a foliation within the XY plane of the core plug **Figure 39**. This fabric is evidenced by the light and dark mineral banding observed within the plug.

Figure 39: Vol B Z core plug with visible foliation of light and dark layers within the XY plane of the plug. This core plug was cut along the Z textural direction. This is perpendicular to the foliation with the local y axis marked as the solid line on the sample.

Table 9: AMS and AIRM ellipsoids for the Vol B Z sample. The AMS axis and AIRM axes intensities have been normalized relative to the other samples measured in this study.

Vol B Z

	Principle Axis	Normalized Magnitude	Declination (degrees)	Inclination (degrees)
AMS	Max	0.3833	34.6	6
	Int	0.3585	305.4	-7.5
	Min	0.2581	86.4	-80.3
AIRM	Max	0.4094	51.4	13
	Int	0.3352	321.8	-1.5
	Min	0.2554	58.1	-77

In comparison to the visual fabric, both the AMS and AIRM results are very consistent with a foliation in the XY plane dominated by MD grains. The MD component is due to the fact that the inclinations of the maximum, minimum, and intermediate principle axes of both the AMS and AIRM ellipsoids being aligned with their counterparts (**Table 9**). The foliation within the XY plane is shown by the low inclination values of the maximum and intermediate values of each ellipsoid.

This sample was the only one tested in this thesis with an observable GRM. Due to the high sensitivity of this method, it is important to measure and account for any remaining magnetization after tumble demagnetization. A GRM was imparted on the sample by placing it in an alternating magnetic field of 40 mT. The resulting remanence in the plane perpendicular to the applied AF was measured then measured. The sample was then demagnetized,

measured and the AF was reapplied after rotating the sample by 15° in the XY plane. The procedure was repeated at 15° intervals in that plane and then likewise in the YZ and ZX planes.

Only one sample, Vol B Z, displayed any significant GRM response shown in **Figure 40**. The other sample sets were tested and did not show any gyroremanence. This was most likely due to a lack of SSD grains within the other samples, which primarily contained MD grains as their major ferrimagnetic component.

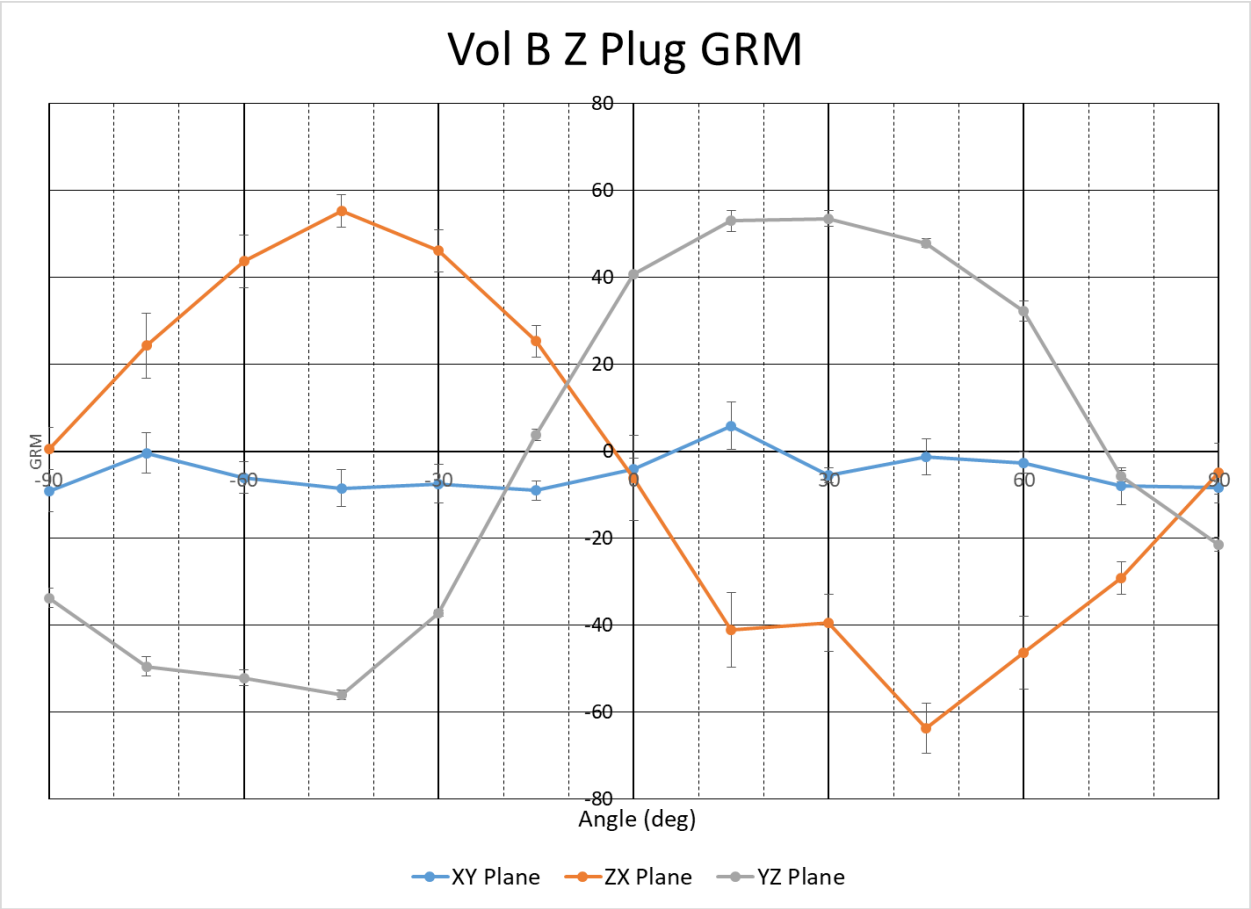

Figure 40: Gyroremanent magnetization displayed by the Vol B Z sample. The blue curve represents the Z component of GRM measured when the AF is applied at various orientations within the XY plane. Similarly the orange curve represents the Y component of GRM measured for an AF applied within the ZX plane and the grey curve is the measured X component resulting from an AF applied within the YZ plane. There is an observable anisotropy of SSD grains within both the ZX and YZ planes. The XY plane does not show any indication of anisotropy. Error bars are resulting from the standard deviation observed with each measurement.

The anisotropy which results in the GRM shown in **Figure 40** is interpreted as a foliation within the XY plane since:

X ≈ Y since there is virtually no GRM measured in the Z axis when the AF is applied in the XY plane.

Y > Z since there is a large positive GRM measured in the X axis when the AF is applied at positive orientations in the YZ plane.

X > Z since there is a large positive GRM in the Y axis when the AF is applied at negative orientations within the ZX plane.

These results are in agreement with the earlier magnetic fabric that was described by the AMS and AIRM for the Vol B Z core plug as well as the visible fabric within the sample. One thing that is important to note however is that there are multiple ferrimagnetic grain sizes present in this sample. These multiple grain sizes are evidenced by the observed GRM signal, which requires SSD particles, and that the AMS and AIRM axes were found to be roughly parallel to each other, which is the result of MD grains within the sample.

For elastic anisotropy this sample was determined to be quasi isotropic by Cholach et al. (2005) due to the elastic parameters $C_{11} \approx C_{22} \approx C_{33}$ (

) determined through the use of high confining pressure p-wave measurements. However, s-wave anisotropy measurements at atmospheric pressures do not support an isotropic material as there is an observable s-wave velocity anisotropy measured within this sample shown by **Figure 41**. This s-wave anisotropy is in alignment with the observed AMS declination values where the maximum declination is at 34° compared to the maximum velocity observed at the 0°/180° polarization. The minimum velocity polarization of 90°/270° is in alignment with the declination of the minimum AMS axis of 86.4° and is 88.1 m/s slower.

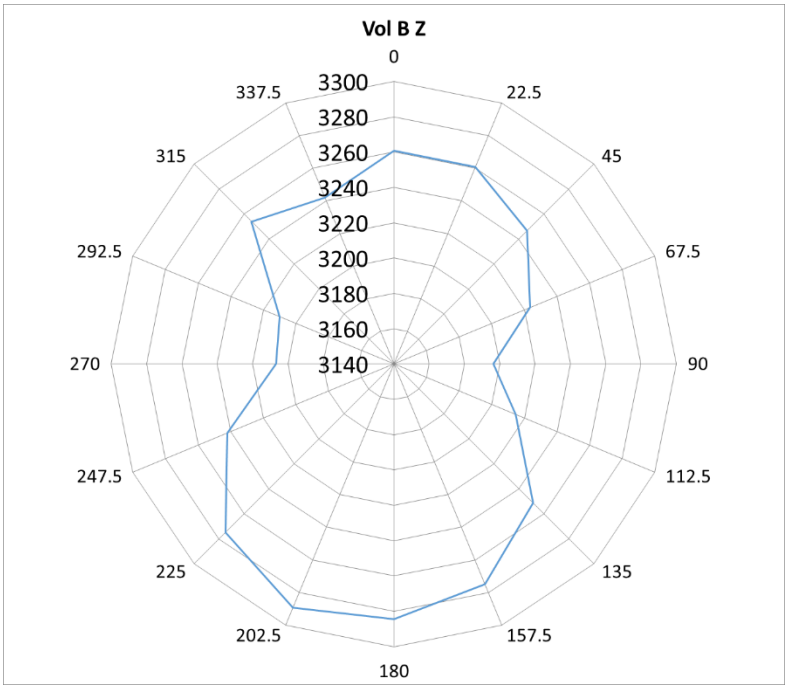

Figure 41: S-wave velocity anisotropy (m/s) within the Vol B Z plug. Maximum s-wave velocity observed within the 0 degree plane and the minimum velocity polarization is at 90 degrees. 0

degree axis is aligned along the core plug x axis and the direction of wave propagation is along the z axis of the plug.

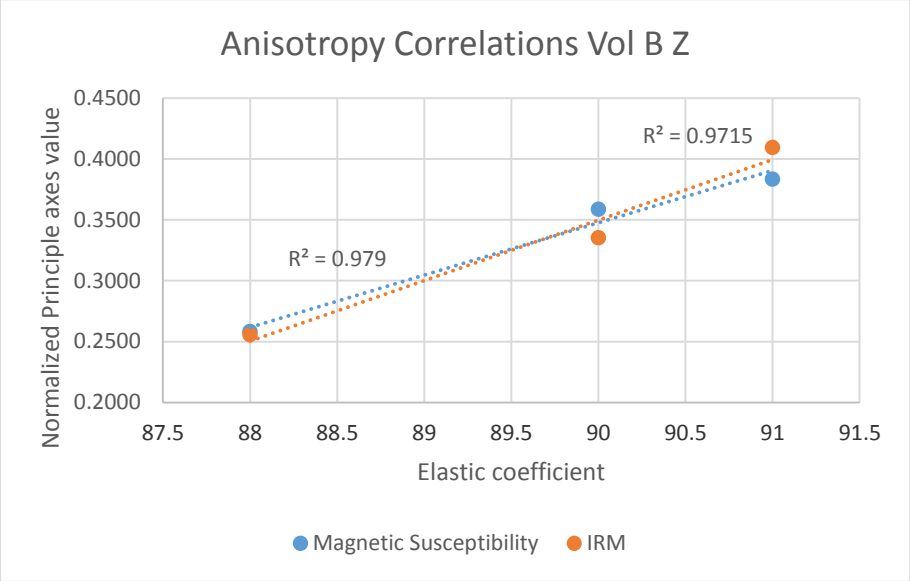

Figure 42: Comparison of normalized AMS (Blue) and AIRM (Orange) principle axes magnitudes determined in this thesis and elastic coefficients C_{11}, C_{22}, and C_{33} related to measured X, Y, and Z p-wave velocities determined by Cholach et al. (2005) for Vol B Z.

There is a strong observable correlation found between the normalized AIRM as well as normalized AMS principle axes values and the respective elastic coefficients. In this sample the maximum, intermediate and minimum axes of both ellipsoids show a strong correlation to the elastic coefficients determined from plug p wave measurements. This is most likely due to the alignment of the ferrimagnetic grains along the same orientation as the larger rock fabric or LPO of the paramagnetic and diamagnetic mineral components.

The N6 X1 core plug shown in **Figure 43** does not display a visible fabric. However, there is a strong magnetic fabric present within this sample. **Table 10** shows that the intensity of the AMS and AIRM ellipsoids are very high, in fact, these values are the highest intensity of all the samples studied in this thesis which indicates a significant ferrimagnetic component in this sample. The maximum and intermediate principle axes for each ellipsoid show relatively similar values for intensity while the minimum axis is significantly lower in intensity. This oblate geometry indicates a foliation within the sample parallel to the z axis of the core plug and the y axis. This indicates that as measured the core plug is taken along the X textural axis with the x direction on the core plug oriented along the Z textural direction and the y plug axis contains the Y textural direction. The high intensity of AMS and AIRM combined with the lack of any GRM response indicates that this sample primarily contains MD ferrimagnetic domain grains that are oriented within the XY plane.

Figure 43: N6 X1 core plug however there is no easily visible fabric within this sample. The lighter streaks are not related to any textural change but rather the drill bit and core plug cutting. This sample was cut along the X textural direction

Table 10: AMS and AIRM ellipsoids for the N6 X1 sample.

	N6 X1			
	Principle Axis	**Normalized Magnitude**	**Declination (degrees)**	**Inclination (degrees)**
AMS	Max	0.3608	101	76.3
	Int	0.3421	269.8	13.4
	Min	0.2971	0.4	2.6
AIRM	Max	0.4111	95.7	35.3
	Int	0.3539	272.3	54.7
	Min	0.2351	4.5	1.6

For elastic anisotropy this sample was determined to be transversely isotropic by Cholach et al. (2005) due to the elastic parameters $C_{11} \approx C_{22} \neq C_{33}$ (**Table 5**) determined through the use of high confining pressure p-wave measurements. Additionally to this it was found that there is an observable s-wave velocity anisotropy within this sample shown by **Figure 44**. This s-wave anisotropy is in alignment with the observed AMS declination values where the maximum declination is at 101° however it has an inclination of 76.3° which primarily has the maximum axis along the z axis of the plug. This should result in there being no major control from the maximum AMS axis of this plug on the observed s-wave anisotropy within this plug however the intermediate axis is in the plane perpendicular to the plug axis and therefore this azimuth will be a better measure for the observed anisotropy. The intermediate axis of the AMS and AIRM ellipsoids has a declination of 269.8° and 272.3° respectively and can be compared to the maximum velocity observed at the 90°/270° polarization. The minimum velocity polarization of

$0^{o}/180^{o}$ is in alignment with the declination of the minimum AMS axis of 0.4^{o} and the AIRM minimum of 4.5^{o} is 725.7 m/s slower.

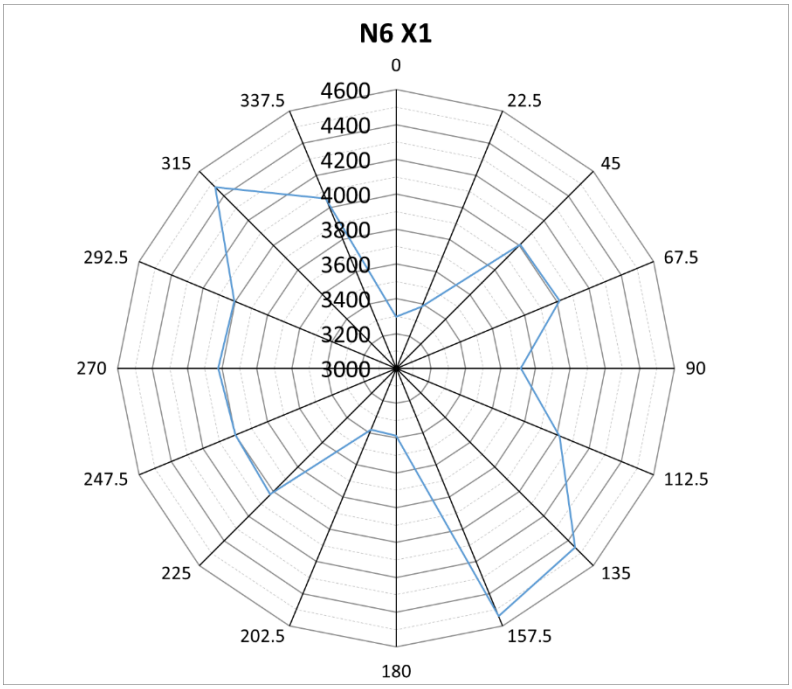

Figure 44: the N6 X1 core plug was the shortest plug measured in this thesis which caused some difficulties with picking a consistent first break arrival due to the noise from the pulse transmitter. However, despite this noise, the fast and slow s-wave polarizations still agree with the magnetic fabric described by the AMS and AIRM.

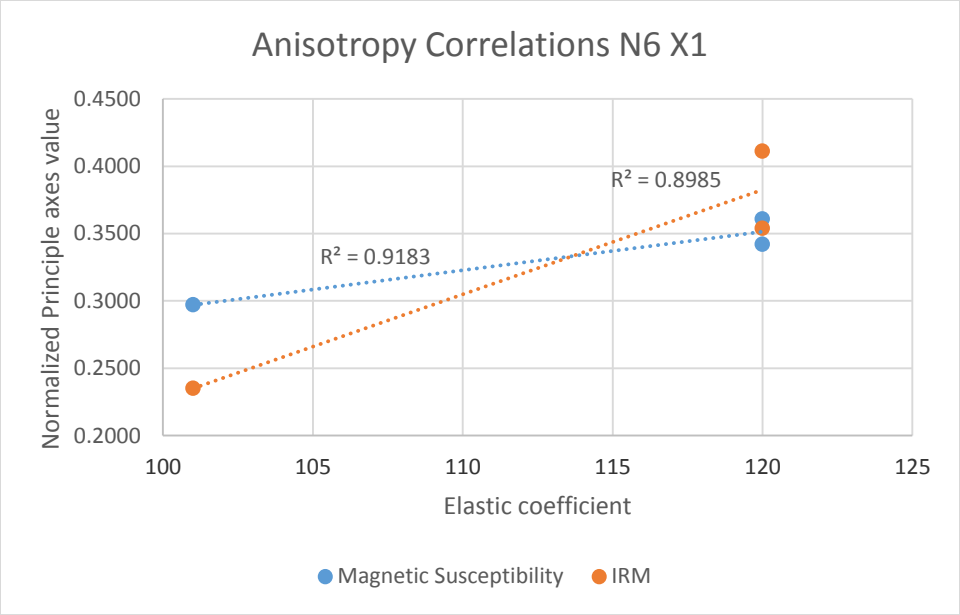

Figure 45: Comparison of normalized AMS (Blue) and AIRM (Orange) principle axes magnitudes measured in this thesis and elastic coefficients C_{11}, C_{22}, and C_{33} related to measured X, Y, and Z p-wave velocities determined by Cholach et al. (2005) for N6 X1.

There is a strong observable correlation found between the normalized AIRM as well as normalized AMS principle axes values and the respective elastic coefficients observed for the N6 sample set (**Figure *45***). In this sample the maximum, intermediate and minimum axes of both ellipsoids show a correlation to the elastic coefficients determined from core plug p wave measurements by Cholach et al. (2005). This is most likely due to the alignment of the ferrimagnetic grains along the same orientation as the larger rock fabric or LPO of the paramagnetic and diamagnetic mineral components. However the R^2 value is lower in this case due to the sample displaying a transversely isotropic elastic symmetry where $C_{11} \approx C_{22} \neq C_{33}$.

The visible fabric for the Vol I Z core plug shown below in **Figure 46** is defined by one textural element. This is the large quartz vein running down the axis of the plug. The magnetic fabric was observed to be a paramagnetic foliation within the XY textural plane (**Table 11**). This is shown by a weakly positive AMS parallel to the quartz vein. There was no observable AIRM response measured for this sample.

Figure 46: Vol I Z core plug, there is no visible fabric within the sample aside from the one quartz vein running parallel to the z axis of the core plug and aligned with the x axis of the core plug. This sample was cut along the Y textural direction.

Table 11: AMS and AIRM ellipsoids for the Vol I Z sample.

	Vol I Z			
	Principle Axis	**Normalized Magnitude**	**Declination (degrees)**	**Inclination (degrees)**
AMS	Max	0.3529	12.6	56.8
	Int	0.3435	181.8	32.7
	Min	0.3036	275	4.9
AIRM	Max	0.7500	315	54.7
	Int	0.2000	135	35.3
	Min	0.0500	225	0

There was a very low value of s-wave anisotropy s-wave anisotropy with a measured difference between the fast and slow polarizations of 17m/s. The fast polarization was found to be at 90^{o} /270^{o} while the slow polarization was observed within the 0^{o}/180^{o} In this case the minimum AMS axis was aligned with the fast polarization direction at 275^{o} and the maximum and intermediate axes aligned with the observed slow direction. The low difference in s-wave velocities makes the relationship between s-wave anisotropy and magnetic parameters difficult to characterize. However there is a strong correlation between the normalized AMS principle axes and the elastic coefficients related to the previously measured p-wave anisotropy seen in **Figure 48**.

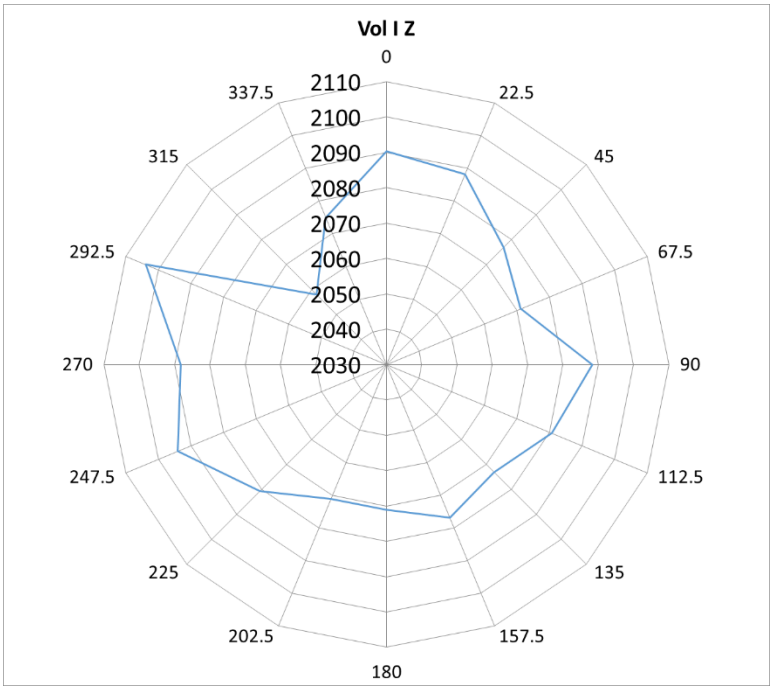

Figure 47: S-wave velocity (m/s) anisotropy measured along the Vol I Z core plug within the ZX textural plane.

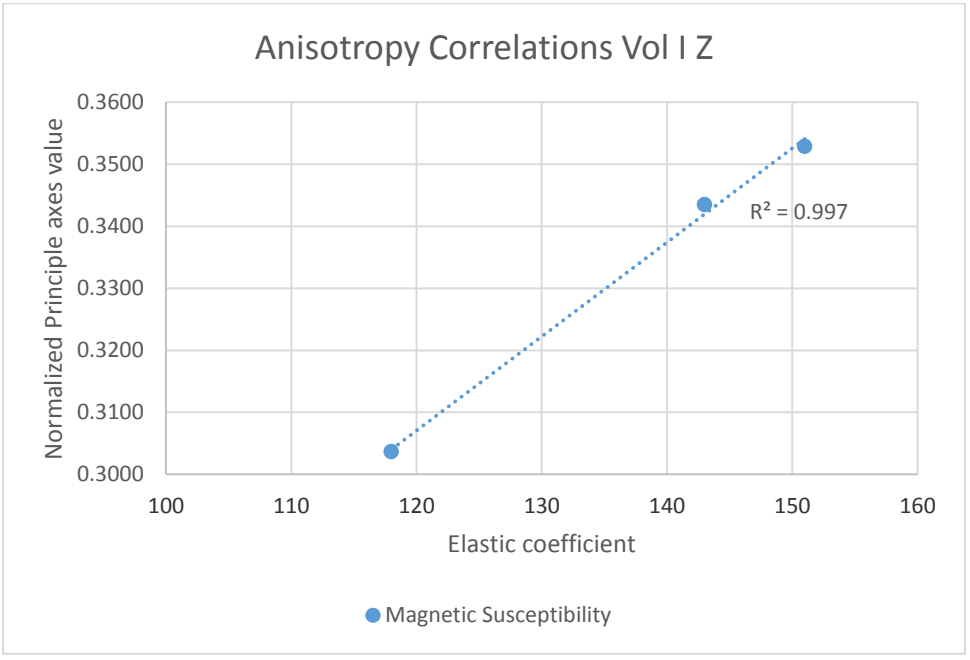

Figure 48: Comparison of normalized AMS principle axes magnitudes from this thesis and elastic coefficients C_{11}, C_{22}, and C_{33} related to measured X, Y, and Z p-wave velocities determined by Cholach et al. (2005) for Vol I Z. There was no significan AIRM observed in this sample.

The 93 20 Z2 plug shows a visual fabric within the rock sample. This fabric appears to be a foliation within the ZX plane of the core plug seen as light banding in **Figure 49**.

Figure 49: Core plug photo of 93-20 Z2. A fabric is clearly observed on this sample. The lighter veins running though the bulk of the sample material are along the z axis of the plug and oriented to be along the x axis of the plug. This core plug was cut in the textural Y direction.

In addition to the visual fabric, the AMS is also consistent with a foliation in the XY plane dominated by diamagnetic grains (**Table 12**). The foliation within this plane is shown by the declination values of the maximum and intermediate values of the ellipsoid.

Table 12: AMS and AIRM ellipsoids for the 93-20 Z2 sample.

		93-20 Z2		
	Principle Axis	**Normalized Magnitude**	**Declination (degrees)**	**Inclination (degrees)**
AMS	Max	-0.2566	153.9	78.2
	Int	-0.3291	162.8	-11.6
	Min	-0.4143	252.4	1.8
AIRM	Max	0.6250	243.4	90
	Int	0.3125	225	0
	Min	0.0625	315	0

From **Figure 50** we can see evidence of s-wave anisotropy with a clear distinction between the fast and slow polarization orientations. The fast s-wave polarization is along the 22.5^{o}/202.5^{o} trend and the slow polarization is along the 112.5^{o} /292.5^{o} trend. These are roughly parallel to the declinations of the maximum/intermediate and minimum AMS principle axes of 153.9^{o} /16.2.8^{o} and 252.4^{o} respectively which indicates that the LPO observed by the s-wave

anisotropy is also responsible for the magnetic fabric observed. There is also an observable correlation between the AMS principle axes magnitudes and the value of elastic coefficients found for this sample set. This sample has the lowest correlation between the values which could be the result of a lower signal to noise ratio as a result of the weak response associated with diamagnetic materials or perhaps this sample set was not properly aligned with the main p-wave anisotropic axes when it was initially cut.

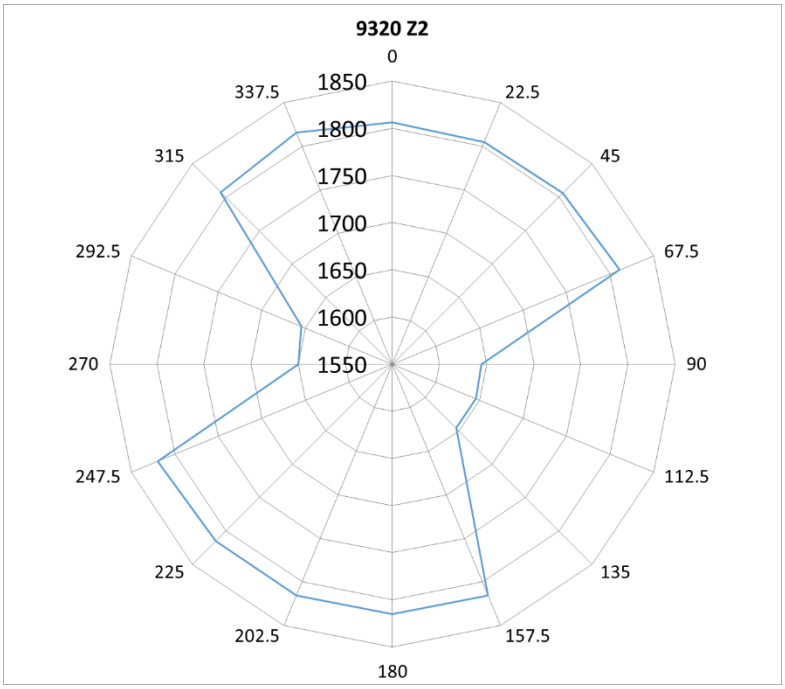

Figure 50: S-wave velocity (m/s) anisotropy observed within the 93 20 Z2 core plug. This details s-wave anisotropy within the ZX plane as this sample was cut along the Y textural axis.

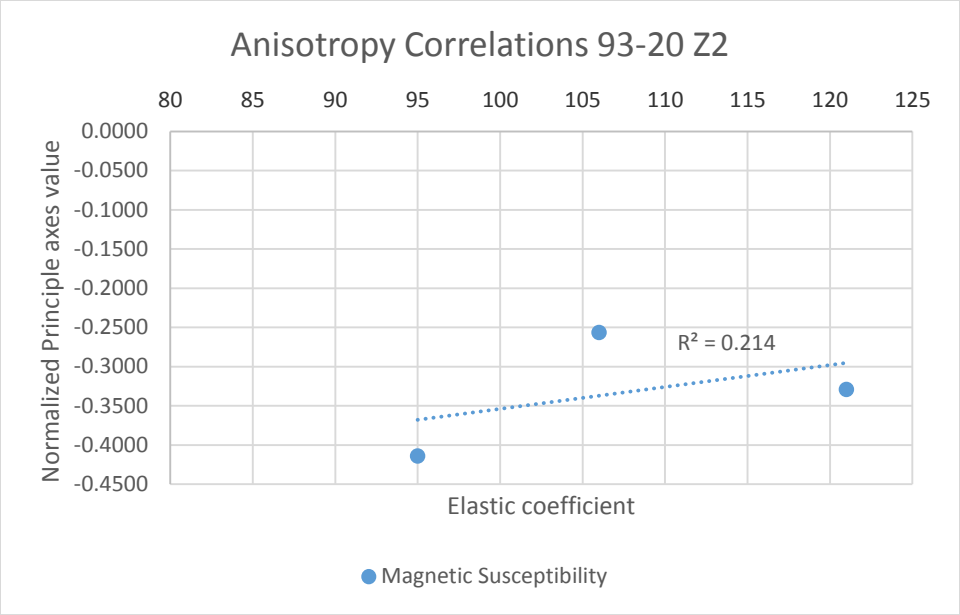

Figure 51: Comparison of normalized AMS principle axes magnitudes from this thesis and elastic coefficients C_{11}, C_{22}, and C_{33} related to measured X, Y, and Z p-wave velocities determined by Cholach et al. (2005) for 93-20 Z2. There was no significant AIRM observed in this sample.

4.6 Conclusions

From the comparison of the different magnetic measurements we were able to determine the relative control for the magnetic fabric observed. In this sample set diamagnetic, paramagnetic, and ferrimagnetic responses were measured. A magnetic fabric was associated to each core plug sample studied in **section 4.5.4**. All of the samples studied displayed varying degrees of oblate magnetic fabrics or magnetic foliations. This magnetic fabric would be at a similar orientation to the visible texture within the sample when one was visible. Additionally, the magnetic fabric due to any ferrimagnetic grains present within each sample was determined.

- **Vol B Z** was shown to be ferrimagnetic. This sample contains a SSD component in addition to the primary MD fabric that was observed. The MD fabric is evidenced by an alignment between the principle axes of both the AMS and AIRM ellipsoids. A contribution from SSD grains was clearly demonstrated through the presence of a gyroremanent magnetization. All of the magnetic measurements AMS, AIRM, and GRM demonstrated a foliation within the XY plane.
- **N6 X1** displayed a MD magnetic fabric where the high magnetic susceptibility values as well as AIRM response indicate a strong ferrimagnetic component however there was no GRM observed within this sample which eliminates the possibility of SSD grains. The AMS and AIRM principle axes were found to be aligned as a foliation within the sample.
- **Vol I Z** was shown to be paramagnetic. There was no observable AIRM measured within this sample which suggested that there was no significant volume of ferrimagnetic

material present. This was also supported by a low positive value of AMS and bulk magnetic susceptibility. The AMS signal within this sample is consistent with a foliation.

- **93-20 Z2** was found to be diamagnetic. There was no observable AIRM measured within the sample suggesting that there was no ferrimagnetic material present. Additionally the AMS and bulk magnetic susceptibility values were all determined to be negative indicating a primarily diamagnetic mineral content, the AMS was determined to be a weak foliation in the XY plane.

The previous acoustic measurements made by Cholach et al. (2005) as well as the supplementary s-wave measurements presented in **Chapter 3** were then compared to the magnetic fabric results. This comparison highlighted several correlations between the two methods.

1) A strong relationship between the magnetic anisotropy (AMS and AIRM) and elastic coefficients was found. It was shown that there is a correlation between the magnitude of elastic coefficients measured previously and the magnitudes of the AMS and AIRM ellipsoid principle axes. Most samples that were compared displayed a very high correlation between these two values.
2) It was also shown that there exists an alignment between shear wave anisotropy and the AMS fabric as well as AIRM and GRM when present. This was evident by the polarization of s-wave slow and fast anisotropic polarizations within each sample aligning parallel to the maximum and minimum AMS principle axes declinations. In cases where one of the principle axes was parallel to the z axis of the plug it was found that the *s-wave* polarizations aligned with the remaining two axes contained within the plane perpendicular to the core plug cylindrical axis.

This suggests that it is possible to use the AMS ellipsoid as a tool to predict the orientations and relative strengths of the 3 compressional principle axis directions for orthorhombic and transversely isotropic materials. The lowest correlation was found for the 93-20 Z2 sample which was diamagnetic in nature. The weak susceptibility of diamagnetic materials and low signal to noise ratio gives an explanation as to why this relationship is less robust for this sample. Other discrepancies could be due to the fact that the core plugs were cut with orientations determined by observable textural elements and these directions may not lie along the true principle axes for each sample.

Care must be taken to understand any ferrimagnetic components within a sample as even a small amount of ferrimagnetic material is able to dominate the magnetic fabric measured within a rock sample. It is particularly important to determine if a ferrimagnetic component contains MD or SSD grains as these will give orthogonal AMS fabrics to each other. Additionally, acoustic measurements are more sensitive to the largest components of a sample and will be largely aligned with the paramagnetic and diamagnetic materials which make up the bulk volume of a sample and determine the LPO within a rock. It is possible however, not observed

in the samples studied in this work, that a small ferrimagnetic component will overwhelm the paramagnetic and diamagnetic minerals and obscure any connection to this LPO.

The primary limitation for this study was the limited number of samples available for measurement. In order to further expand on this work it is suggested that more samples be included into developing this relationship between the AMS fabric and the shear wave anisotropy. It is also suggested that a more in depth study of the elastic coefficients for other samples be completed as the values used in this work relied on assumptions that the core plug was cut along an acoustic principle axis. Comparison of these magnetic results against the off diagonal elastic coefficients would also be necessary to fully characterise this relationship.

CHAPTER 5: CONCLUSIONS & FUTURE WORK

5.1 Conclusions

This thesis studied the potential use of magnetic nanoparticles as reservoir contrast agents. Mn-Zn ferrite nanoparticles were investigated due to their high magnetic susceptibility. This magnetic susceptibility was found to be higher than the nanoparticle magnetite previously investigated by Morrow et al. (2015). The higher magnetic susceptibility of these Mn-Zn ferrite nanoparticles makes them the better choice for contrast agents in applications for hydraulic fracturing to either measure the propant distribution or monitor fracture fluids. To test their viability, a variety of Mn-Zn ferrites were studied with varying Mn:Zn ratios for their applicability as reservoir contrast agents with several key observations found:

1) The ferrite nanoparticles with a higher Mn:Zn ratio were found to have a higher Curie temperature. This is expected due to the fact that the Curie point of Zn is lower than that of Mn.
2) Magnetic susceptibility as well as saturation magnetization are independent of the Mn:Zn ratio when observed at a low temperature of 25^{o}C.
3) The particles with a higher Mn:Zn ratio had a lower decrease in magnetic susceptibility and saturation magnetization when observed at reservoir temperature conditions of 125^{o}C.

These observations appear to be related to the Curie temperature of these ferrite nanoparticles. Therefore it was found that the ferrite nanoparticles with a higher Mn:Zn ratio are more useful as magnetic contrast agents at downhole reservoir temperatures.

When compared to nanoscale magnetite these Mn-Zn ferrite nanoparticles are 6.5x more effective as contrast agents under reservoir conditions. That said, the proper application of these nanoparticles to characterize a reservoir and measure the effectiveness of a frac job still requires a large mass of Mn-Zn ferrite nanoparticles which is still not an economic solution. Therefore it would be useful to further test different nanoparticle options for more magnetically susceptible contrast agents in order to reduce the cost of this characterization technique.

This thesis also investigated the relationship between magnetic and acoustic anisotropy within several metamorphic rock samples. Three dimensional AMS and AMR measurements have been used to confirm magnetic fabric present within several rock samples originating from the Flin Flon belt of the Trans Hudson Orogen. The compressional elsastic anisotropy within these samples was previously determined by Cholach et al. (2005). This work was expanded on in this thesis by measuring the s-wave anisotropy within each sample and comparing it to the previously measured p-wave anisotropy as well as the magnetic fabric found in each. For the samples studied both AMS and AMR methods used agree with the observed visible rock fabric

and provide comparable magnetic fabric results to the acoustic anisotropy methods. These results are:

1) The sample sets studied in detail indicate a magnetic foliation through the use of AMS and AIRM. One sample displayed a GRM foliation within the XY plane that was consistent with the AMS and AIRM results as well as the observable rock fabric.
2) Additionally there was a correlation found between the magnitudes of the principle axes for the AMS and AIRM ellipsoids and the elastic coefficients previously determined by Cholach et al. (2005).
3) The declination of the maximum and minimum principle axes of the AMS ellipsoid on the core plugs aligned with the azimuth of the fast and slow s-wave polarization directions that were observed for each core plug respectively. This also agreed with the orientations of the AIRM principle axes and GRM fabric when present.
4) The use of one dimensional bulk magnetic susceptibility measurements also demonstrated a correlation with p-wave velocity measurements in the same rock plug samples. This relationship appears to be related to the lattice preferred orientation of the minerals within the sample and the strongest correlations were observed with the samples containing hornblende.

The relationships are unique to the individual sample sets and most likely tied to the minerology of each sample. Nevertheless, the correlations found between the magnetic anisotropy techniques utilized in this thesis and the acoustic anisotropy measurements suggest that magnetic anisotropy could be used to rapidly predict the orientation and relative magnitudes of the principle acoustic anisotropy axes. This would allow us to further optimize the directions of observation for core plug acoustic measurements as these measurements are complex and time consuming when compared to magnetic anisotropy methods.

5.2 Improvements and future work

There are several improvements that can be made for the Mn-Zn nanoferrite results. These recommendations can also apply to testing various other nanoparticle types in the future.

1) Conduct the high temperature measurements in either a vacuum or inert gas. This will remove the potential for oxidation of the samples.
2) Utilize various other dispersant media in testing besides calcium fluoride. Typical sand and ceramic propant samples should be used as dispersants during Curie point measurements as well as calcium fluoride.
3) Test additional nanoparticle compositions as magnetic contrast agents for ones with higher magnetic susceptibility values.

There were several limitations within the anisotropic study which could also be improved on in the future. To further improve on these results:

1) Increase the sample size tested for both their acoustic and magnetic anisotropies.

2) Conduct a detailed study of texture of each major mineral within the sample. Additional care must be taken to quantify the percent volume, size, and shape of any ferrimagnetic minerals.
3) Orient the three orthogonal core plug directions for acoustic measurements with the magnetic fabric of a sample.
4) Measure the p and s-wave anisotropy in more directions than three orthogonal axes based on symmetry. Ideally this will be done to fully characterize the 21 elastic coefficients possible for a material. Comparing the magnetic results with the full elastic coefficient tensor would help fully understand the relationship between these methods.

REFERENCES

Ali, A., and D. K. Potter, 2012, Temperature dependence of the magnetic properties of reservoir rocks and minerals and implications for in situ borehole predictions of petrophysical parameters: Geophysics, v. 77, no. 3, p. WA211, doi:10.1190/geo2011-0282.1.

Arbaret, L., P. Launeau, H. Diot, and S. Sizaret, 2013, Magnetic and shape fabrics of magnetite in simple shear flows: Journal of Volcanology and Geothermal Research, v. 249, p. 25–38, doi:10.1016/j.jvolgeores.2012.09.003.

Arulmurugan, R., B. Jeyadevan, G. Vaidyanathan, and S. Sendhilnathan, 2005, Effect of zinc substitution on Co-Zn and Mn-Zn ferrite nanoparticles prepared by co-precipitation: Journal of Magnetism and Magnetic Materials, v. 288.

Auld, B. A., 1974, Acoustic Fields and Waves in Solids: Two Volumes: Physics Today, v. 27, no. 10, p. 63–64, doi:10.1063/1.3128926.

Backus, G. E., 1962, Long-wave elastic anisotropy produced by horizontal layering: Journal of Geophysical Research, v. 67, no. 11, p. 4427, doi:10.1029/JZ067i011p04427.

Barron, R. A., M. J. Tour, A. A. Busnaina, J. Y. Jung, S. Somu, Y. Kanj, D. Potter, R. Daniel, and J. Ullo, 2010, Big Things in Small Packages: Oilfield Review, v. 22, no. 3, p. 38–49.

Bean, C. P., and I. S. Jacobs, 1956, Magnetic Granulometry and Super-Paramagnetism: Journal of Applied Physics, v. 27, p. 1448.

Birch, F., 1960, The Velocity of Compressional Waves in Rocks to 10 Kilobars, Part I: Journal of Geophysical Research, v. 65, p. 1083–1102.

Birch, F., 1961, The Velocity of Compressional Waves in Rocks to 10 Kilobars, Part II: Journal of Geophysical Research, v. 66, no. 7, p. 2199–2224.

Borradaile, G. J., and M. Jackson, 2010, Structural geology, petrofabrics and magnetic fabrics (AMS, AARM, AIRM): Journal of Structural Geology, v. 32, no. 10, p. 1519–1551, doi:10.1016/j.jsg.2009.09.006.

Byerlee, J., and M. Johnston, 1976, A Magnetic Method for Determining the geometry of hydraulic fractures: Pure Applied Geophysics, v. 114, p. 425–433.

Cholach, P. Y., 2005, The Elasticity of Intrinsically Anisotropic Rocks: University of Alberta.

Cholach, P. Y., J. B. Molyneux, and D. R. Schmitt, 2005, Flin Flon Belt seismic anisotropy: elastic symmetry, heterogeneity, and shear-wave splitting: Canadian Journal of Earth Sciences, v. 42, no. 4, p. 533–554, doi:10.1139/e04-094.

Cocuzza, M., C. Pirri, and V. Rocca, 2012, Current and Future Nanotech applications in the oil industry: American Journal of Applied Science, v. 9, p. 784–793.

Collinson, D. W., 1965, Depositional remanent magnetization in sediments: Journal of Geophysical Research, v. 70, no. 18, p. 4663, doi:10.1029/JZ070i018p04663.

Crampin, S., 1985, Evaluation of anisotropy by shear-wave splitting: Geophysics, v. 50, no. 1, p. 142–152.

Crampin, S., and S. Peacock, 2005, A review of shear-wave splitting in the compliant crack-critical anisotropic Earth: Wave Motion, v. 41, no. 1, p. 59–77, doi:10.1016/j.wavemoti.2004.05.006.

Daley, P. F., and F. Hron, 1977, Reflection and transmission coefficients for transversely isotropic media: Bulletin of the Seismological Society of America, v. 67, no. 3, p. 661–675.

Dammel, J., J. Bielicki, and M. Pollak, 2011, A Tale of Two Technologies: Hydraulic Fracturing and Geologic Carbon Sequestration.: Environmental Science and Technology, v. 45, p. 5075–5076.

Dewhurst, D. N., and A. F. Siggins, 2006, Impact of fabric, microcracks and stress field on shale anisotropy: Geophysical Journal International, v. 165, no. 1, p. 135–148, doi:10.1111/j.1365-246X.2006.02834.x.

Dubey, A. K., 2014, Understanding an Orogenic Belt Structural Evolution of the Himalaya: Anisotropy of Magnetic Susceptibility: Switzerland, Springer International Publishing, doi:10.1007/978-3-319-05588-6.

Dunlop, D. J., and O. Ozdemir, 1997, Rock Magnetism: Fundamentals and Frontiers: Cambridge University Press.

Ferré, E. C., A. Gébelin, J. L. Till, C. Sassier, and K. C. Burmeister, 2014, Deformation and magnetic fabrics in ductile shear zones: A review: Tectonophysics, v. 629, p. 179–188, doi:10.1016/j.tecto.2014.04.008.

Frenkel, J., and J. Dorfman, 1930, Spontaneous and Induced Magnetisation in Ferromagnetic Bodies.: Nature, v. 126, no. 3173, p. 274–275, doi:10.1038/126274a0.

Gangi, A. F., and R. L. Carlson, 1996, An asperity-deformation model for effective pressure: Tectonophysics, v. 256, no. 1–4, p. 241–251, doi:10.1016/0040-1951(95)00167-0.

Griffiths, D. J., 1999, Magnetic Fields in Matter, *in* Introduction to Electrodynamics: Upper Saddle River, NJ, Prentice Hall, p. 255–278.

Han, Z., 2005, Correlations between seismic and magnetic susceptibility andisotropy in serpentinized peridotite: University of Alberta.

He, T., 2006, P and S Wave Velocity Measurement and Pressure Sensitivity Analysis of AVA Response: University of Alberta.

Helbig, K., 1994, Foundations of Anisotropy for Exploration Seismics: Elsevier Science Serials, 486 p.

Hemsing, D. B., 2007, Laboratory Determination of Seismic Anisotropy in Sedimentary Rock from the Western Canadian Sedimentary Basin: University of Alberta.

Hornby, B. E., L. M. Schwartz, and J. A. Hudson, 1994, Anisotropic effective-medium modeling of

the elastic properties of shales: Geophysics, v. 59, no. 10, doi:10.1190/1.1443546.

Housen, B. A., and B. A. van der Pluijm, 1991, Slaty cleavage development and magnetic anisotropy fabrics: Journal of Geophysical Research, v. 96, no. B6, p. 9937, doi:10.1029/91JB00605.

Hrouda, F., 1982, Magnetic anisotropy of rocks and its application in geology and geophysics: Geophysical Surveys, v. 5, p. 37–82, doi:10.1007/BF01450244.

Hrouda, F., and J. Ježek, 1999, Theoretical models for the relationship between magnetic anisotropy and strain: Effect of triaxial magnetic grains: Tectonophysics, v. 301, no. 3–4, p. 183–190, doi:10.1016/S0040-1951(98)00267-4.

Hudson, J. A., and J. P. Harrison, 2000, Engineering Rock Mechanics: An Introduction to the Principles: London, U. K., Imperial College of Science, Technology and Medicine.

Ising, E., 1942, On the Magnetic Properties of Varved Clay: Arkiv Astron, v. 29A, p. 1–37.

Johnston, D. H., 1987, Physical-Properties of Shale At Temperature and Pressure: Geophysics, v. 52, no. 10, p. 1391–1401.

Johnston, J. E., and N. I. Christensen, 1995, Seismic anisotropy of shales: International Journal of Rock Mechanics and Mining Sciences and Geomechanics Abstracts, v. 33, p. 72A–72A(1), doi:10.1029/95JB00031.

Jones, L. E. A., and H. F. Wang, 1981, Ultrasonic velocities in Cretaceous shales from the Williston basin: p. 288, doi:10.1190/1.1441199.

Kebaili, A., and D. R. Schmitt, 1997, Ultrasonic anisotropic phase velocity determination with the Radon transformation: The Journal of the Acoustical Society of America, v. 101, no. 6, p. 3278, doi:10.1121/1.418344.

Kittel, C., 1949, Physical Theory of Ferromagnetic Domains: Physical Review, v. 21, no. 4, p. 541–583, doi:10.1103/PhysRev.79.745.2.

Landau, L., and E. Lifshits, 1935, On the Theory of the Dispersion of Magnetic Permeability in Ferromagnetic Bodies: Phys. Zeitsch. der Sow., v. 169, no. 14, p. 14–22, doi:10.1109/TMAG.2004.836740.

Lima, E., A. L. Brandl, A. D. Arelaro, and G. F. Goya, 2006, Spin disorder and magnetic anisotropy in Fe3 O4 nanoparticles: Journal of Applied Physics, v. 99, no. 8, p. 083908, doi:10.1063/1.2191471.

Lowrie, W., 2007, Fundamentals of Geophysics: Cambridge University Press.

Lucas, S. B., A. Green, Z. Hajnal, D. White, J. Lewry, K. Ashton, W. Weber, and R. Clowes, 1994, Three dimensional collisional structure of the Trans-Hudson Orogen, Canada: Tectonophysics, v. 232, p. 143–160.

Lucas, S. B., R. A. Stern, E. C. Syme, B. A. Reilly, and D. J. Thomas, 1996, Intraoceanic tectonics and the development of continental crust: Geological Survey of America Bulletin, v. 108,

no. 5, p. 602–629.

Maguire-Boyle, S., D. Garner, and J. Heimann, 2014, Automated method for determining the flow of surface functionalized nanoparticles through a hydraulically fractured mineral formation using plasmonic silver nanoparticles: Environmental Science: Processes & Impacts, v. 16, p. 220–231.

Martinez, J. M., 2014, Elastic Properties of Sedimentary Rocks: University of Alberta, 1-210 p.

Martínez, J. M., and D. R. Schmitt, 2016, A comparative study of the anisotropic dynamic and static elastic moduli of unconventional reservoir shales : Implication for Geomechanical investigations: Geophysics, v. 81, p. 245–261.

Mattei, M., L. Sagnotti, C. Faccenna, and R. Funiciello, 1997, Magnetic fabric of weakly deformed clay-rich sediments in the Italian peninsula: Relationship with compressional and extensional tectonics: Tectonophysics, v. 271, no. 1–2, p. 107–122, doi:10.1016/S0040-1951(96)00244-2.

McDaniel, R., S. McCarthy, and M. Smith, 2012, No Title, 8129318: US Patent.

Meissner, F. F., 1984, Petroleum Geology of the Bakken Formation Williston Basin, North Dakota and Montana: v. 28, p. 159–179.

Miller, D., R. Plumb, and G. Boitnott, 2013, Compressive strength and elastic properties of a transversely isotropic calcareous mudstone: Geophysical Prospecting, v. 61, no. 2, p. 315–328, doi:10.1111/1365-2478.12031.

Morrow, L., 2015, Metal Ferrite Nanoparticles as Tracers in Hydraulically Fractured Wells: Rice University.

Morrow, L. et al., 2018, Temperature dependence on the mass susceptibility and mass magnetization of superparamagnetic Mn – Zn – ferrite nanoparticles as contrast agents for magnetic imaging of oil and gas reservoirs: Experimental Nanoscience, v. 13, no. 1, p. 107–118, doi:10.1080/17458080.2018.1426894.

Morrow, L., D. K. Potter, and A. R. Barron, 2014, Detection of magnetic nanoparticles against proppant and shale reservoir rocks: Journal of Experimental Nanoscience, no. November, p. 1–14, doi:10.1080/17458080.2014.951412.

Musgrave, M. J. P., 1970, Deviation of ray from wave normal for elastic waves in principal planes of crystal symmetry: Journal of the Mechanics and Physics of Solids, v. 18, no. 3, p. 207–211, doi:10.1016/0022-5096(70)90024-4.

Néel, L., 1947, *MAGNETISME - LE CHAMP COERCITIF DUNE POUDRE FERROMAGNETIQUE CUBIQUE A GRAINS ANISOTROPES: COMPTES RENDUS HEBDOMADAIRES DES SEANCES DE L ACADEMIE DES SCIENCES, v. 224, no. 22, p. 1550–1551.

Néel, L., 1955, Some theoretical aspects of Rock-Magnetism: Advances in Physics, v. 4, no. 14, p. 191–243, doi:10.1080/00018735500101204.

Néel, L., 1949, Théorie du traînage magnétique des ferromagnétiques en grains fins avec applications aux terres cuites: Ann. Géophys, v. 5, p. 99–136.

Nguyen, P., and D. Fulton, 2006, Electroconductive proppant compositions and related methods., 7073581: US Patent.

Nicot, J., and B. Scanlon, 2012, Water Use for Shale-Gas Production in Texas, U.S..: Environmental Science and Technology, v. 46, p. 3580–3586.

Nye, J. F., 1957, Physical Properties of Crystals: London, Oxford University Press.

OPEC, 2014, OPEC. 2014 World Oil Outlook: Vienna.

Orbaek, A., L. Morrow, S. J. Maguire-Boyle, and A. R. Barron, 2015, Reagent Control over the Composition of mixed metal oxide nanoparticles: Journal of Experimental Nanoscience, v. 10, no. 5, p. 324–349.

Owens, W. H., and D. Bamford, 1976, Magnetic, seismic, and other anisotropic properties of rock fabrics: Philosophical Transactions of the Royal Society of London.

Potter, D. K., 2004, A comparison of anisotropy of magnetic remanence methods -- a user's guide for application to palaeomagnetism and magnetic fabric studies: Geological Society, London, Special Publications, v. 238, no. 1, p. 21–35, doi:10.1144/GSL.SP.2004.238.01.03.

Potter, D. K., and A. Stephenson, 1988, Single-domain particles in rocks and magnetic fabric analysis: Geophysical Research Letters, v. 15, no. 10, p. 1097, doi:10.1029/GL015i010p01097.

Rath, C., S. Anand, R. P. Das, K. K. Sahu, S. D. Kulkarni, S. K. Date, and N. C. Mishra, 2002, Dependence on cation distribution of particle size, lattice parameter, and magnetic properties in nanosize Mn-Zn ferrite: Journal of Applied Physics, v. 91, p. 2211–2215.

Robion, P., C. David, J. Dautriat, J.-C. Colombier, L. Zinsmeister, and P.-Y. Collin, 2014, Pore fabric geometry inferred from magnetic and acoustic anisotropies in rocks with various mineralogy, permeability and porosity: Tectonophysics, v. 629, p. 109–122, doi:10.1016/j.tecto.2014.03.029.

Roca, A., S. Veintemillas-Verdaguer, and M. Port, 2009, Effect of nanoparticle and aggregate size on the relaxometric properties of mr contrast agents based on high quality magnetite nanoparticles.: Journal of Physical Chemistry B, v. 113, p. 7033–7039.

Rochette, P., M. Jackson, and C. Aubourg, 1992, Rock magnetism and the interpretation of anisotropy of magnetic susceptibility: Reviews of Geophysics, v. 30, no. 3, p. 209, doi:10.1029/92RG00733.

Sahimi, M., 2012, Flow and Transport in Porous Media and Fractured Rock: From Classical Methods to Modern Approaches: Weinheim Germany, Wiley.

Sayers, C. M., 2005, Seismic anisotropy of shales: Geophysical Prospecting, v. 53, no. 5, p. 667–676, doi:10.1111/j.1365-2478.2005.00495.x.

Sayers, C. M., 1994, The elastic anisotrophy of shales: Journal of Geophysical Research: Solid Earth (1978--2012), v. 99, no. B1, p. 767–774, doi:10.1029/93JB02579.

Sondergeld, C. H., and C. S. Rai, 1992, Laboratory observations of shear-wave propagation in anisotropic media: The Leading Edge, v. 11, no. 2, p. 38–43.

Spaldin, N. A., 2010, Magnetic Materials: Fundamentals and Applications: Cambridge University Press, 1-290 p.

Stephenson, a., 1993, Three-axis static alternating field demagnetization of rocks and the identification of natural remanent magnetization, gyroremanent magnetization, and anisotropy: Journal of Geophysical Research, v. 98, no. B1, p. 373, doi:10.1029/92JB01849.

Stephenson, A., S. Sadikun, and D. K. Potter, 1986, A theoretical and experimental comparison of the anisotropies of magnetic-susceptibility and remanence in rocks and minerals: Geophysical J. Royal Astronomical Soc., v. 84, no. 1, p. 185–200.

Stephenson, A., S. Sadikun, and D. K. Potter, 1986, A theoretical and experimental comparison of the anisotropies of magnetic susceptibility and remanence in rocks and minerals: Geophysical Journal International, v. 84, no. 1, p. 185–200, doi:10.1111/j.1365-246X.1986.tb04351.x.

Sun, C., J. Lee, and M. Zhang, 2008, Magnetic nanoparticles in MR imaging and drug delivery.: Ad Drug Delivery Review, v. 60, p. 1252–1265.

Tarling, D. H., and F. Hrouda, 1993, The Magnetic Anisotropy of Rocks: London, Chapman & Hall.

Thomsen, L., 1986, Weak elastic anisotropy: Geophysics, v. 51, no. 10, p. 1954, doi:10.1190/1.1442051.

Vernik, L., and X. Liu, 1997, Velocity anisotropy in shales: A petrophysical study: Geophysics, v. 62, no. 2, p. 521, doi:10.1190/1.1444162.

Vernik, L., and A. Nur, 1992, Ultrasonic velocity and anisotropy of hydrocarbon source rocks: Geophysics, v. 57, no. 5, p. 727–735.

Vinnik, L. P., B. Romanowicz, and V. Romanowicz, 1989, Azimuthal anisotropy in the earth from observations of KSK at GEOSCOPE and NARS broadband stations: Bulletin of the Seismological Society of America, v. 191, no. 2, p. 1542–1558.

Wang, Z. Z., H. Wang, and M. E. Cates, 2001, Effective elastic properties of solid clays: Geophysics, v. 66, no. 2, p. 428.